

Study the Cyclic Plasticity Behavior of 508 LAS under Constant, Variable and Grid-Load-Following Loading Cycles for Fatigue Evaluation of PWR Components

Interim Report on Experimental and Mechanistic Modeling Results

Nuclear Engineering Division

About Argonne National Laboratory

Argonne is a U.S. Department of Energy laboratory managed by UChicago Argonne, LLC under contract DE-AC02-06CH11357. The Laboratory's main facility is outside Chicago, at 9700 South Cass Avenue, Argonne, Illinois 60439. For information about Argonne and its pioneering science and technology programs, see www.anl.gov.

DOCUMENT AVAILABILITY

Online Access: U.S. Department of Energy (DOE) reports produced after 1991 and a growing number of pre-1991 documents are available free via DOE's SciTech Connect (<http://www.osti.gov/scitech/>)

Reports not in digital format may be purchased by the public from the National Technical Information Service (NTIS):

U.S. Department of Commerce
National Technical Information Service
5301 Shawnee Rd
Alexandria, VA 22312
www.ntis.gov
Phone: (800) 553-NTIS (6847) or (703) 605-6000
Fax: (703) 605-6900
Email: orders@ntis.gov

Reports not in digital format are available to DOE and DOE contractors from the Office of Scientific and Technical Information (OSTI):

U.S. Department of Energy
Office of Scientific and Technical Information
P.O. Box 62
Oak Ridge, TN 37831-0062
www.osti.gov
Phone: (865) 576-8401
Fax: (865) 576-5728
Email: reports@osti.gov

Disclaimer

This report was prepared as an account of work sponsored by an agency of the United States Government. Neither the United States Government nor any agency thereof, nor UChicago Argonne, LLC, nor any of their employees or officers, makes any warranty, express or implied, or assumes any legal liability or responsibility for the accuracy, completeness, or usefulness of any information, apparatus, product, or process disclosed, or represents that its use would not infringe privately owned rights. Reference herein to any specific commercial product, process, or service by trade name, trademark, manufacturer, or otherwise, does not necessarily constitute or imply its endorsement, recommendation, or favoring by the United States Government or any agency thereof. The views and opinions of document authors expressed herein do not necessarily state or reflect those of the United States Government or any agency thereof, Argonne National Laboratory, or UChicago Argonne, LLC.

Study the Cyclic Plasticity Behavior of 508 LAS under Constant, Variable and Grid-Load-Following Loading Cycles for Fatigue Evaluation of PWR Components

Interim Report on Experimental and Mechanistic Modeling Results

Subhasish Mohanty, Bipul Barua, William Soppet, Saurin Majumdar, and Ken Natesan

Nuclear Engineering Division, Argonne National Laboratory

September 2016

This page intentionally left blank

ABSTRACT

This report provides an update of an earlier assessment of environmentally assisted fatigue for components in light water reactors. This report is a deliverable in September 2016 under the work package for environmentally assisted fatigue under DOE's Light Water Reactor Sustainability program. In an April 2016 report, we presented a detailed thermal-mechanical stress analysis model for simulating the stress-strain state of a reactor pressure vessel and its nozzles under grid-load-following conditions. In this report, we provide stress-controlled fatigue test data for 508 LAS base metal alloy under different loading amplitudes (constant, variable, and random grid-load-following) and environmental conditions (in air or pressurized water reactor coolant water at 300°C). Also presented is a cyclic plasticity-based analytical model that can simultaneously capture the amplitude and time dependency of the component behavior under fatigue loading. Results related to both amplitude-dependent and amplitude-independent parameters are presented. The validation results for the analytical/mechanistic model are discussed. This report provides guidance for estimating time-dependent, amplitude-independent parameters related to material behavior under different service conditions. The developed mechanistic models and the reported material parameters can be used to conduct more accurate fatigue and ratcheting evaluation of reactor components.

This page intentionally left blank

TABLE OF CONTENTS

Study the Cyclic Plasticity Behavior of 508 LAS under Constant, Variable and Grid-Load-Following Loading Cycles for Fatigue Evaluation of PWR Components	i
ABSTRACT	i
Table of Contents	iii
List of Figures	v
List of TABLES	ix
Abbreviations	x
Acknowledgments	xi
1 Introduction	1
2 Theoretical Background: Cyclic Plasticity Models	3
2.1 Time/Cycle-Dependent Constitutive Relations for Incremental Cyclic Plasticity	3
2.2 Estimation of Time-Dependent-Amplitude-Independent Parameters	5
2.2.1 Method 1: Parameter estimation using block equivalent monotonic stress-strain curves	5
2.2.2 Method 2: Parameter estimation using all stress-strain data within a block	7
3 Experimental Results from Fatigue Tests	9
3.1 Constant-Amplitude Fatigue Test	10
3.2 Comparison between Stress-and Stroke-Controlled Fatigue Tests.....	12
3.3 Variable-Amplitude Fatigue Tests.....	14
3.4 Grid-Load-Following Random Amplitude Fatigue Tests.....	22
4 Results from Material Parameter Estimation	30
4.1 Cycle-by-Cycle Parameters Estimated from Constant-Amplitude Fatigue Tests.....	30
4.2 Parameters Estimated from Variable-Amplitude Fatigue Tests	33
4.2.1 Cycle-by-Cycle Parameters Estimated from Variable-Amplitude Fatigue Tests	34
4.2.2 Block-by-Block Parameters Estimated from Variable-Amplitude Fatigue Tests Using Method 1	36
4.2.3 Block-by-Block Parameters Estimated from Variable-Amplitude Fatigue Tests Using Method 2	40
5 Results from Analytical Modeling	43
5.1 Constant-Amplitude Fatigue Tests	43
5.2 Variable-Amplitude Fatigue Tests.....	45
5.2.1 Results Using Time-Independent and Time-Dependent (Cycle-by-cycle) Parameters	45

5.2.2 Results Using Time-Dependent-Amplitude-Independent (Block-by-Block) Parameters	47
6 Summary and Future Study	52
7 References	54

LIST OF FIGURES

Figure 2.1 Block loading showing first three blocks for variable-amplitude fatigue test.....	6
Figure 2. 2 Schematic of average equivalent stress-strain monotonic curve estimated from hysteresis curves in a block.....	6
Figure 3. 1 Engineering stress-strain curve estimated from ET-T08 tensile test (air, 300 °C) data of 508 LAS base metal.	11
Figure 3. 2 Time history of applied stress for ET-F28 fatigue test.....	11
Figure 3. 3 Time history of observed strain for ET-F28 fatigue test.	12
Figure 3. 4 Fatigue life of 508 LAS base alloy under two test modes (air and 300°C).....	13
Figure 3. 5 Maximum/minimum stress for 508 LAS base alloy during two fatigue test modes (air and 300°C).	13
Figure 3. 6 Maximum/minimum strain for 508 LAS base alloy during two fatigue test modes (air and 300°C).....	14
Figure 3. 7 Variable-amplitude block loading during ET-F31 fatigue test.....	15
Figure 3. 8 Time history of measured stroke for ET-F31 fatigue test.	15
Figure 3. 9 Time history of measured strain for ET-F31 fatigue test.	16
Figure 3. 10 Example comparison of strain predicted from stroke (using stroke-strain mapping relation) with strain obtained from ET-F31 fatigue test. The data correspond to fatigue cycle no. 7 in block no. 1 (see Figure 3.7).....	16
Figure 3. 11 Stress-strain hysteresis plots of first block (for all 12 cycles within the block) obtained through ET-F31 fatigue test of 508 LAS base alloy under in-air and 300°C condition.	17
Figure 3. 12 Stress-strain hysteresis plots (after removing the offset due to ratcheting strain) of last block (for all 12 cycles within the block) obtained through ET-F31 fatigue test of 508 LAS base alloy under in-air and 300°C condition.	17
Figure 3. 13 Variable-amplitude block loading during EN-F32 fatigue test.	18
Figure 3. 14 Time history of measured stroke for EN-F32 fatigue test.....	19
Figure 3. 15 Time history of predicted strain (estimated from measured stroke, as shown in Figure 3.13, using stroke-strain mapping relation generated from ET-F31 in-air fatigue test) for EN-F32 PWR environment fatigue test.	19
Figure 3. 16 Stress-strain hysteresis plots of first block (with all 12 cycles within the block) obtained through variable-amplitude fatigue test (ET-F32) of 508 LAS base alloy under PWR environment and 300°C condition.	20
Figure 3. 17 Stress-strain hysteresis (after removing the offset due to ratcheting strain) plots of last block (with all 12 cycles within the block) obtained through variable-amplitude fatigue test (ET-F32) of 508 LAS base alloy under PWR environment and 300°C condition.	20

Figure 3. 18 Maximum and minimum strain for 508 LAS base metal alloy fatigue tested under stress-controlled variable-amplitude loading for in-air (ET-F31) and PWR environment (ET-F32) conditions.....	21
Figure 3. 19 Model of RPV and its hot leg (HL) and cold leg (CL) nozzles [29].....	22
Figure 3. 20 Shape, approximate size, and location of axial crack in left HL nozzle of RPV [29].....	23
Figure 3. 21 Von-Mises stress contour at a typical full power condition [29]. Arrow showing a typical nodal location, where stress states are used as fatigue test loading input for grid-load-following fatigue tests (ET-F3 and EN-F34).	23
Figure 3. 22 Von-Mises stress histories at maximum stressed node in left HL and the corresponding maximum stressed node in right HL nozzle [29].....	24
Figure 3. 23 Example screen shot of the control panel during 1st block loading of EN-F34 test.....	25
Figure 3. 24 Time history of measured stroke (frame cross-head displacement) for ET-F33 fatigue test.....	26
Figure 3. 25 Time history of measured strain for ET-F33 fatigue test.	27
Figure 3. 26 Example stroke-versus-strain mapping results for ET-F33 fatigue test.	27
Figure 3. 27 Schematic showing the cross-section of 508 LAS- 316 SS dissimilar metal weld plate. The green highlighted block shows the location of EN-F34 fatigue specimen.28	
Figure 3. 28 Time history of measured stroke (frame cross-head displacement) for EN-F34 fatigue test.....	28
Figure 3. 29 Time history of estimated strain for EN-F34 fatigue test.....	29
Figure 3. 30 Hysteresis (strain-versus-stress) curves for first 64 blocks of EN-F34 fatigue test.....	29
Figure 4.1 Equivalent monotonic stress-strain curves estimated from upward/downward cycle (for first 50 cycles) stress-strain curves data for ET-F28 fatigue test. Also given are the tensile test data (in-air, 300°C condition) and the 0.05% offset yield line.....	31
Figure 4.2 Cycle-by-cycle elastic modulus estimated from constant-amplitude fatigue tests. Corresponding parameter estimated from tensile test is also shown.	31
Figure 4.3 Cycle-by-cycle elastic limit stress estimated from constant-amplitude fatigue tests. Corresponding parameter estimated from tensile test is also shown.	32
Figure 4.4 Cycle-by-cycle nonlinear kinematic hardening parameter C1 estimated from constant-amplitude fatigue tests. Corresponding parameter estimated from tensile test is also shown.	32
Figure 4.5 Cycle-by-cycle nonlinear kinematic hardening parameter γ_1 estimated from constant-amplitude fatigue tests. Corresponding parameter estimated from tensile test is also shown.	33
Figure 4.6 Cycle-by-cycle elastic modulus estimated from variable-amplitude fatigue tests. .	34

Figure 4.7 Cycle-by-cycle elastic limit stress estimated from variable-amplitude fatigue tests.	35
Figure 4.8 Cycle-by-cycle nonlinear kinematic hardening parameter C1 estimated from variable-amplitude fatigue tests.	35
Figure 4.9 Cycle-by-cycle nonlinear kinematic hardening parameter γ_1 estimated from variable-amplitude fatigue tests.	36
Figure 4.10 Block average equivalent monotonic strain-stress graphs (estimated from ET-F31 test data) for 508 LAS base metal alloy fatigue tested in air at 300°C.....	37
Figure 4.11 Block average equivalent monotonic strain-stress graphs (estimated from EN-F32 test data) for 508 LAS base metal alloy fatigue tested in PWR environment at 300°C.	37
Figure 4.12 Block-by-block elastic modulus estimated (using method 1) from variable-amplitude fatigue tests.	38
Figure 4.13 Block-by-block elastic limit stress estimated (using method 1) from variable-amplitude fatigue tests.	38
Figure 4.14 Block-by-block nonlinear kinematic hardening parameter C1 estimated (using method 1) from variable-amplitude fatigue tests.	39
Figure 4.15 Block-by-block nonlinear kinematic hardening parameter γ_1 estimated (using method 1) from variable-amplitude fatigue tests.	39
Figure 4.16 Example comparison of experimental true back stress (as a function of true plastic strain) with that predicted by using average hardening parameters (method 2) pertaining to that block.	40
Figure 4.17 Block-by-block elastic modulus estimated (using method 2) from variable-amplitude fatigue tests.	41
Figure 4.18 Block-by-block elastic limit stress estimated (using method 2) from variable-amplitude fatigue tests.	41
Figure 4.19 Block-by-block nonlinear kinematic hardening parameter C1 estimated (using method 2) from variable-amplitude fatigue tests.	42
Figure 4.20 Block-by-block nonlinear kinematic hardening parameter γ_1 estimated (using method 2) from variable-amplitude fatigue tests.	42
Figure 5.1 Predicted (using time-independent parameters estimated from tensile test ET-T08) versus experimental hysteresis curves for first 20 cycles of ET-F28 test.	44
Figure 5.2 Predicted (using time-independent parameters estimated from ET-F28 fatigue test data at half-life) versus experimental hysteresis curves for first 20 cycles of ET-F28 test.....	44
Figure 5.3 Predicted (using time-dependent, cycle-by-cycle parameters estimated from ET-F28) versus experimental hysteresis curves for first 20 cycles of ET-F28 test.	45
Figure 5.4 Predicted (using time-independent parameters from ET-T08) versus experimental hysteresis curves for first block (with 12 variable-amplitude cycles) of ET-F31 test.	46

Figure 5.5 Predicted (using time-independent parameters from half-life fatigue data of ET-F28) versus experimental hysteresis curves for first block (with 12 variable-amplitude cycles) of ET-F31 test.	46
Figure 5.6 Predicted (using cycle-by-cycle, amplitude-dependent parameters estimated from first block data of ET-F31 fatigue test) versus experimental hysteresis curves for first block (with 12 variable-amplitude cycles) of ET-F31 test.	47
Figure 5.7 Predicted (using method 1 block-by-block parameters estimated from ET-F31 data) versus experimental hysteresis curves for 12 variable-amplitude fatigue cycles within the 1 st block of ET-F31 test.	48
Figure 5.8 Predicted (using method 2 block-by-block parameters estimated from ET-F31 data) versus experimental hysteresis curves for 12 variable-amplitude fatigue cycles within the 1 st block of ET-F31 test.	49
Figure 5.9 Predicted (using method 1 block-by-block parameters estimated from ET-F31 data) versus experimental hysteresis curves for 12 variable-amplitude fatigue cycles within the 20 th block of ET-F31 test.	49
Figure 5.10 Predicted (using method 2 block-by-block parameters estimated from ET-F31 data) versus experimental hysteresis curves for 12 variable-amplitude fatigue cycles within the 20 th block of ET-F31 test.	50
Figure 5.11 Predicted (using method 2 block-by-block parameters estimated from EN-F32 data) versus experimental hysteresis curves for 12 variable-amplitude fatigue cycles within the 1 st block of ET-F32 test.	50
Figure 5.12 Predicted (using method 2 block-by-block parameters estimated from EN-F32 data) versus experimental hysteresis curves for 12 variable-amplitude fatigue cycles within the 20 th block of ET-F32 test.	51

LIST OF TABLES

Table 3. 1 Test conditions for 508 LAS base metal tensile and fatigue tests. 10

ABBREVIATIONS

ANL	Argonne National Laboratory
ASME	American Society of Mechanical Engineers
DO	Dissolved Oxygen
FE	Finite Element
FEA	Finite Element Analysis
HAZ	Heat Affected Zone
LAS	Low Alloy Steel
LWR	Light Water Reactor
LWRS	Light Water Reactor Sustainability
PWR	Pressurized Water Reactor
RCS	Reactor Coolant System
RPV	Reactor Pressure Vessel
SS	Stainless Steel

ACKNOWLEDGMENTS

This research was supported through the U.S. Department of Energy's Light Water Reactor Sustainability program under the work package of environmental fatigue study, program manager Dr. Keith Leonard.

This page intentionally left blank

1 Introduction

The present method used for fatigue life evaluation of nuclear power plant components has large uncertainties [1]. This problem is due to the overdependence on approaches that involve empirical fatigue life estimation, such as use of test-based curves of stress/strain versus life (S~N) and Coffin-Manson type empirical relations. In addition, the uncertainty is higher for reactor components exposed to the coolant environment.

During the past ten to fifteen years, the US Nuclear Regulatory Commission (US-NRC), Argonne National Laboratory (ANL), and other regulatory and research agencies, such as the Japan Nuclear Energy Safety Organization (JNES), invested substantial effort to reduce this uncertainty in life estimation. One method of accomplishing this has been factoring out the effect of the reactor coolant on the fatigue life estimations based on S~N curves [2-4]. Recent work by various researchers [5-14] has further demonstrated the value of the experimental and S~N based approach to fatigue life estimation.

The stress-strain state of a component along with results from the S~N-based methodology is used for fatigue analysis of a reactor component. The stress-strain state can be estimated by following appropriate stress analysis methodology. In general, the relevant design codes [15, 16] used for fatigue evaluation are based on elastic stress analysis. Ideally, if stress and strain stay below the elastic limit (a prerequisite for following the elastic stress analysis methodology), no fatigue would occur in the reactor components. However, safety-critical reactor components often fail due to fatigue damage associated with the reactor loading cycles and environmental conditions. In general, fatigue damage in a reactor occurs due to the presence of stress concentration and/or plastic zones and its interaction with reactor environment. The plastic zone formation in the reactor metal can be due to local stress concentration. Hence, for better accuracy, it is essential to estimate the fatigue and ratcheting damage of reactor components based on the results of elastic-plastic stress analysis rather than pure elastic stress analysis alone. Recently, elastic-plastic analysis and fatigue life estimation based on flaw tolerance [17-22] have increasingly become an active research area by infusing more mechanics-based prediction capability into the overall fatigue evaluation methodology. Since elastic-plastic ratcheting is a phenomenon closely related to the transient plastic deformation behavior, its accurate description requires the calculation of material hardening stress-strain states as a function of fatigue cycles or time. This type of stress-strain ratcheting analysis can be done with Chaboche-type kinematic material models [23-25]. However, most of the available material models used for elastic-plastic stress analysis are based on fixed and time-independent stress-strain curves, obtained either from a tensile test data or from a specific cycle of fatigue test data. However, a model based on fixed or time-independent stress-strain curves may not accurately capture the time/cycle-dependent ratcheting behavior of reactor materials under cyclic thermal-mechanical loading.

In our recent work [26-28] we reported various material parameters such as elastic modulus, elastic/yield limit stress, and Chaboche-type hardening constants, for the time/cycle-dependent model. Although, using the reported material parameters, we were able to capture the time/cycle dependence of stress-strain curves, we found that the estimated time-dependent parameters are sensitive to fatigue test amplitude. Note that those parameters were estimated based on constant amplitude fatigue test data. To avoid the issue of amplitude dependence on material properties, in this reported work we are proposing estimation techniques involving parameters based on variable-amplitude fatigue tests. This approach is intended to capture not only the time/cycle dependency in the material parameters but also the amplitude independency in the estimated parameters. To estimate the parameters, we conducted a few block/variable-amplitude fatigue tests using 508 LAS base metal alloy, which is a widely used alloy for

making the reactor pressure vessel (RPV) and its nozzle. The tests were conducted under in-air and coolant environment condition of a pressurized water reactor (PWR). We also developed cyclic-plasticity analytical/mechanistic models to verify whether or not the estimated parameters are able to capture the elastic-plastic stress-strain state of the test specimens. Furthermore, a few fatigue tests were conducted under grid-load-following conditions. The grid-load-following amplitudes were selected based on our earlier stress analysis results for an RPV nozzle (of a PWR reactor) [29, 30]. Note that the load sequence effect associated with the real-life spectrum load [31, 32] may have a significant effect on the fatigue life of a component. Hence, it is essential to study the stress-strain state of material under prototypical loading conditions. In this report, experimental results are presented pertinent to the grid-load-following conditions.

2 Theoretical Background: Cyclic Plasticity Models

In our previous work [26-28], we proposed a time-dependent material hardening model for key reactor materials, such as 508 LAS and 316 SS base metal and 316 SS similar metal welds. In the proposed model, it was assumed that the material yield surface and the corresponding material hardening parameters evolve over time. The proposed model was employed to evaluate the corresponding time-dependent parameters such as elastic modulus, yield limit, and kinematic hardening. The parameters were estimated using fatigue test data calculated for constant amplitude loading. However, from the reported results, we found that the estimated time-dependent parameters are sensitive to test amplitude. To capture the dependency of the material model on amplitude, we conducted fatigue tests under variable amplitude loading. During a variable-amplitude fatigue test, repetitive loading blocks, with each block consisting of multiple cycles with varying amplitudes, are applied to the specimen. The details of the variable-amplitude fatigue tests and the experimental results are presented in Section 3. In this section, the theoretical background of the associated cyclic plasticity models and parameter estimation techniques is briefly discussed.

2.1 Time/Cycle-Dependent Constitutive Relations for Incremental Cyclic Plasticity

In the present work, an elastic-plastic material is considered. The strain is assumed to be small and additively decomposed into the elastic part, which obeys Hooke's law, and the plastic part, which is governed by the associated flow rule based on a Von-Mises yield surface. Further assumptions are that the elastic deformation remains isotropic, and the yield surface translates and expands. The time/cycle-dependent yield function f_i , corresponding to the time-dependent cyclic plasticity model, can be expressed as,

$$f_i(\boldsymbol{\sigma}_{i,j,k}, \boldsymbol{\alpha}_{i,j,k}) = \sigma_e(\boldsymbol{\sigma}_{i,j,k} - \boldsymbol{\alpha}_{i,j,k}) - \sigma_i^y \quad (2.1)$$

where σ_e is the Von-Mises stress, $\boldsymbol{\sigma}_{i,j,k}$ is the k^{th} instance stress vector in the j^{th} fatigue cycle of the i^{th} block, $\boldsymbol{\alpha}_{i,j,k}$ is the corresponding k^{th} instance back stress vector, and σ_i^y is the i^{th} block yield stress. The back stress vector represents an intra-cycle memory effect, i.e., kinematic hardening stress, while the inter-cycle evolution of the yield stress represents the isotropic softening/hardening. According to the normality hypothesis [33, 34], the increment in plastic strain tensor is in the direction normal to the tangent to the yield surface at the load point. Thus, the k^{th} -instance plastic increment in the j^{th} fatigue cycle of the k^{th} block can be written as,

$$d\boldsymbol{\varepsilon}_{i,j,k}^{pl} = d\lambda_{i,j,k} \frac{\partial f_i}{\partial \boldsymbol{\sigma}_{i,j,k}} \quad (2.2)$$

where $\frac{\partial f_i}{\partial \boldsymbol{\sigma}_{i,j,k}}$ defines the direction of the plastic strain increment, and $d\lambda_{i,j,k}$ determines the magnitude of the plastic strain increment. In this work, a Chaboche-type time/cycle-dependent (and amplitude-dependent/independent) kinematic hardening model is used to capture the evolution of time (and amplitude) dependency of the center of the yield surface in the form of back stress $\boldsymbol{\alpha}_{i,j,k}$. According to

these models, the incremental back stress at the k^{th} instance in the j^{th} fatigue cycle of the i^{th} block can be expressed as, for linear kinematic hardening,

$$d\alpha_{i,j,k} = \frac{2}{3}C1_i d\epsilon^{pl}_{i,j,k} \quad (2.3)$$

and for nonlinear kinematic hardening,

$$d\alpha_{i,j,k} = \frac{2}{3}C1_i d\epsilon^{pl}_{i,j,k} - \gamma1_i \alpha_{i,j,k} dP_{i,j,k} \quad (2.4)$$

where $C1_i$ and $\gamma1_i$ are cycle-dependent (and amplitude-dependent/independent) material constants. The parameter $C1_i$ is a proportional constant that gives a linear relation between the increment in the back stress $d\alpha_{i,j,k}$, and the increment in the accumulated plastic strain $d\epsilon^{pl}_{i,j,k}$, while $\gamma1_i$ describes the rate at which the back stress decreases with the increase in accumulated effective plastic strain $dP_{i,j,k}$. For incremental plasticity, the plastic strain increment $d\epsilon^{pl}_{i,j,k}$ associated with the time-dependent nonlinear kinematic hardening model [given in Eq. (2.4)] can be expressed as

$$d\epsilon^{pl}_{i,j,k} = d\lambda_{i,j,k} \frac{\partial f_i}{\partial \sigma_{i,j,k}} = \left(\frac{\frac{\partial f_i}{\partial \sigma_{i,j,k}} C_i d\epsilon_{i,j,k}}{\left(\frac{\partial f_i}{\partial \sigma_{i,j,k}} \right) C_i \left(\frac{\partial f_i}{\partial \sigma_{i,j,k}} \right) + \gamma1_i \left(\frac{\partial f_i}{\partial \alpha_{i,j,k}} \right) \alpha_{i,j,k} - \frac{2}{3} C1_i \left(\frac{\partial f_i}{\partial \alpha_{i,j,k}} \right) \left(\frac{\partial f_i}{\partial \alpha_{i,j,k}} \right)} \right) \frac{\partial f_i}{\partial \sigma_{i,j,k}} \quad (2.5)$$

Substituting $\gamma1_i = 0$ in Eq. (2.5), the above expression of incremental plastic strain can be reduced to its linear kinematic hardening form:

$$d\epsilon^{pl}_{i,j,k} = d\lambda_{i,j,k} \frac{\partial f_i}{\partial \sigma_{i,j,k}} = \left(\frac{\frac{\partial f_i}{\partial \sigma_{i,j,k}} C_i d\epsilon_{i,j,k}}{\left(\frac{\partial f_i}{\partial \sigma_{i,j,k}} \right) C_i \left(\frac{\partial f_i}{\partial \sigma_{i,j,k}} \right) - \frac{2}{3} C1_i \left(\frac{\partial f_i}{\partial \alpha_{i,j,k}} \right) \left(\frac{\partial f_i}{\partial \alpha_{i,j,k}} \right)} \right) \frac{\partial f_i}{\partial \sigma_{i,j,k}} \quad (2.6)$$

The above expressions of incremental plastic strain [Eqs. (2.5) and (2.6)] can be used for developing a cyclic-plasticity finite element or analytical model. The associated parameters include the time/cycle-dependent (and amplitude-dependent/independent) elastic modulus (E_i , used for estimating the stiffness matrix C_i), kinematic hardening parameters ($C1_i$ and $\gamma1_i$), and yield stress (σ_i^y , used for estimating the yield function f_i). Equations 2.1-2.6 constitute the 3-D form of the proposed cyclic-plasticity model. However, to model the uniaxial test data for parameter estimation (the estimation procedure discussed in Section 2.2 and the related results are discussed in Section 4), the equivalent uniaxial form has to be used. The equivalent uniaxial forms of Eqs. (2.5) and (2.6) are, respectively:

$$d\epsilon^{pl}_{i,j,k} = \left(\frac{E_i}{E_i + C1_i - \gamma1_i \alpha_i^y} \right) d\epsilon_{i,j,k} \quad (\text{nonlinear hardening model}) \quad (2.7)$$

$$d\epsilon^{pl}_{i,j,k} = \left(\frac{E_i}{E_i + C1_i} \right) d\epsilon_{i,j,k} \quad (\text{linear hardening model}) \quad (2.8)$$

Note that, in Eqs. 2.1 to 2.8, the subscripts i , j , and k respectively represent block number, cycle number in block i , and data number in cycle j . This is the convention used in this report for modeling the block (variable amplitude) loading fatigue specimens, while for constant amplitude fatigue specimen i and j are considered to be same.

2.2 Estimation of Time-Dependent-Amplitude-Independent Parameters

In our previous work [26-28], we presented a cycle-by-cycle technique to estimate time/cycle-dependent parameters. In the previously reported work, the cycle-by-cycle parameters were estimated under the assumption of constant loading amplitude for the fatigue test data. However, our earlier results [26] indicated that the cycle-by-cycle parameters are sensitive to loading amplitudes. If the parameters are sensitive to test amplitude, those parameters may not capture the stress-strain state of a reactor component under realistic random loading conditions. To alleviate this issue, we propose an approach based on variable-amplitude fatigue test data. Here we introduce two novel methods for estimating the associated time-dependent-amplitude-independent parameters from variable-amplitude fatigue test data. Both methods are discussed below.

2.2.1 Method 1: Parameter estimation using block equivalent monotonic stress-strain curves

An example of block loading during a variable amplitude fatigue test is shown in Figure 2.1. During this test, the load amplitude was varied by gradually increasing from a minimum value (selected to fall within the elastic limit) to a maximum value (equivalent of maximum 0.5% strain, similar to that selected for previously conducted constant-amplitude fatigue tests) and then gradually decreasing to the minimum again. In method 1, the average equivalent monotonic stress-strain curves were estimated by joining the peak locations (for tensile portion) and trough locations (for compressive portion) of individual cyclic stress-strain curves within a loading block. A demonstration of estimating the average equivalent monotonic stress-strain graph from the block loading (tensile portion) is shown in Figure 2.2. The stress-strain graphs estimated from all the blocks are used to estimate the corresponding average parameters. Note that in a particular block there are multiple cycles. For the example in Figures 2.1 and 2.2, there are a total of 12 cycles of the same or different amplitudes within each block. Our previous cycle-by-cycle approach would have produced 12 sets of material parameters for each loading block, but the present approach produces only one set of parameters for each block. We assume that this single set of parameters for a particular block would capture the effect of all loading amplitudes within that block. At the same time, the effect of time dependency due to hardening and softening of materials is captured through estimating the parameters of individual time-dependent loading blocks.

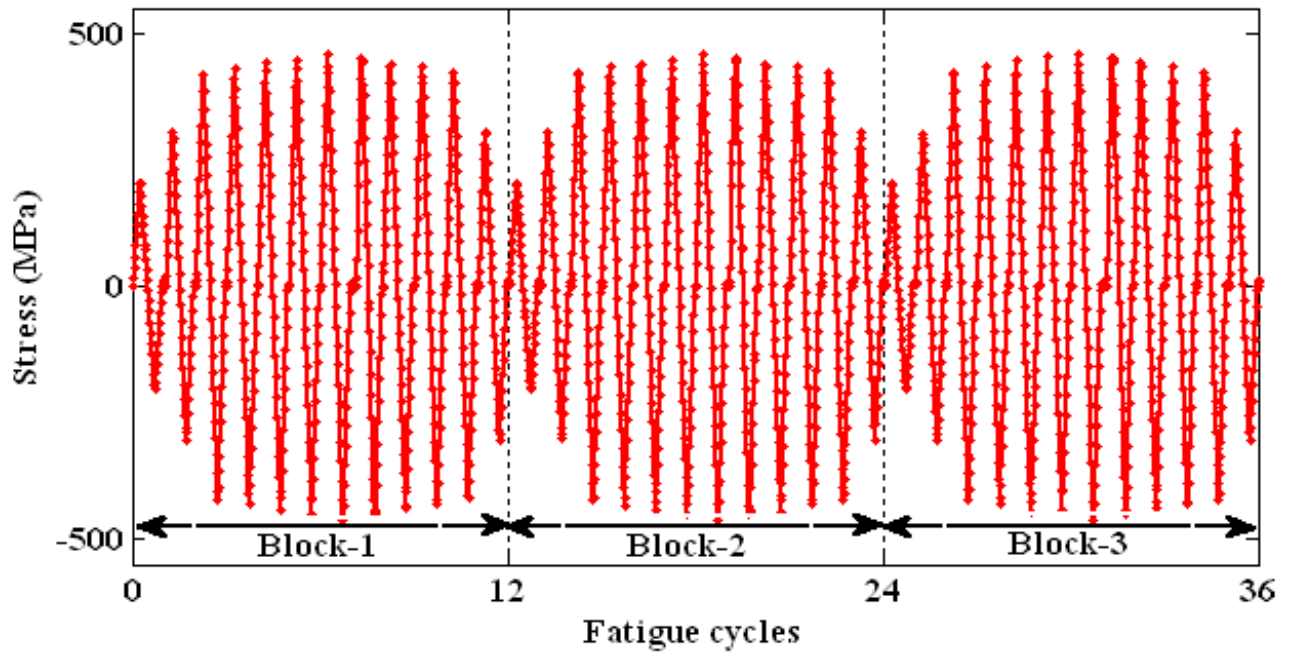


Figure 2.1 Block loading showing first three blocks for variable-amplitude fatigue test.

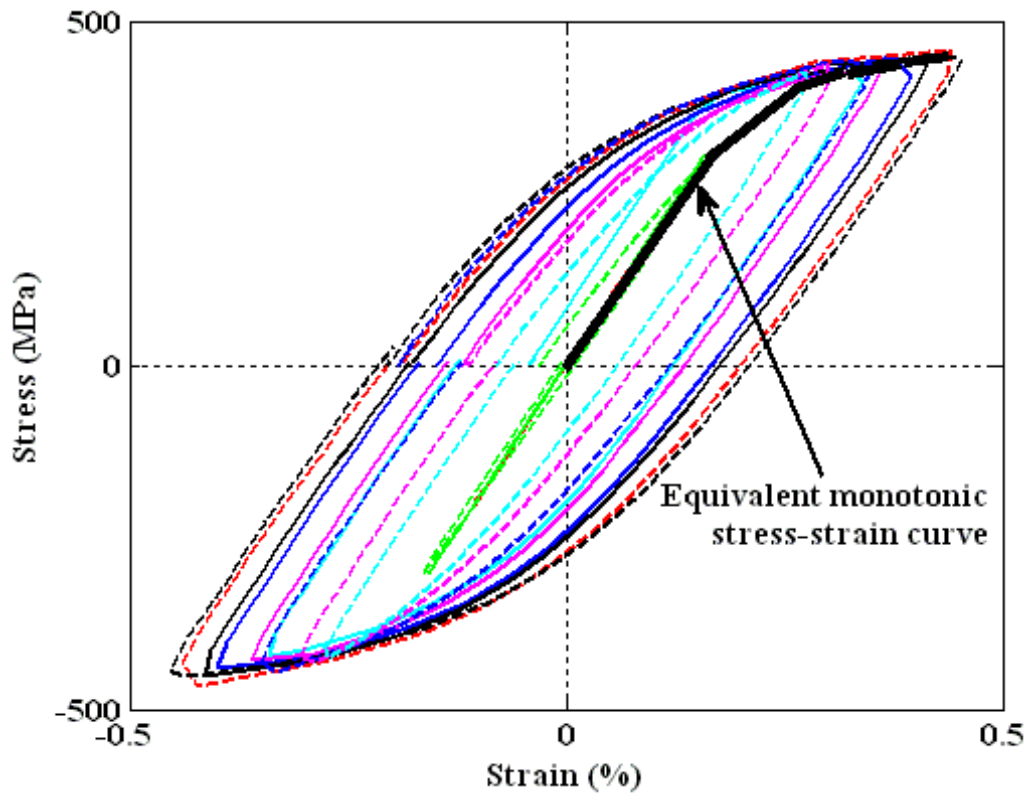


Figure 2. 2 Schematic of average equivalent stress-strain monotonic curve estimated from hysteresis curves in a block.

2.2.2 Method 2: Parameter estimation using all stress-strain data within a block

Instead of using the peak and trough locations of cyclic stress-strain curves (within a block), as in method 1, the entire stress-strain data for all the cycles in a block are used in method 2. This is done not only to capture the peak amplitude of all the stress-strain curves within a block but also the shape/path of all the stress-strain curves within that block. To that end, all the cyclic stress-strain curves in a block are first converted into equivalent monotonic stress-strain curves, as was done for individual cycles in the cycle-by-cycle parameter estimation technique [26-28]. Based on an assumed elastic limit strain, the material parameters are then determined for all the blocks by using the Gauss-Newton optimization scheme. The parameter estimation method in this case is similar to the method discussed in Refs. [26-28], except that the entire kinematic hardening stress ($\alpha_{i,j,k}$) and intra-cycle plastic strain ($\bar{p}_{i,j,k}$) within a particular block were selected for estimating a single set of parameters.

The steps for estimating the amplitude-independent average parameters for block i are as follows:

Step 1: Estimate the kinematic hardening stress or back ($\alpha_{i,j,k}$) and corresponding accumulated intra-cycle plastic strain ($\bar{p}_{i,j,k}$) for k instances ($k = 1, 2, \dots, m_j$) using the expressions:

$$\alpha_{i,j,k} = \sigma_{i,j,k} - \sigma_i^y \quad (2.9)$$

$$\bar{p}_{i,j,k} = \varepsilon_{i,j,k} - \frac{\sigma_i^y}{E_i} \quad (2.10)$$

where subscript j represents the j^{th} ($i=1, 2, \dots, 2n$) up/down cycle of the i^{th} block, superscript k represents the k^{th} data point in the shifted and scaled j^{th} ($i=1, 2, \dots, 2n$) up/down cycle of the i^{th} block, and σ_i^y and E_i are the average yield stress and average elastic modulus in the i^{th} block. Note that there are n fatigue cycles in each block, i.e., n upward cycles and n downward cycles, which make the total number of monotonic cycles in each block $2n$.

Step 3: Assume initial values for $\mathbf{L} = [C1_i \ \gamma1_i]^T$.

Step 4: Estimate the residual function vector

$$\mathbf{r} = [r_{i,j=1,k=1} \dots r_{i,j=1,k=m_1} \ r_{i,j=2,k=1} \dots r_{i,j=2,k=m_2} \dots r_{i,j=2n,k=1} \dots r_{i,j=2n,k=m_{2n}}] \quad (2.11)$$

with the k^{th} instance residual in the j^{th} cycle of the i^{th} block as

$$r_{i,j,k} = \frac{C1_i}{\gamma1_i} \left[1 - \exp\left(-\gamma1_i(p)\bar{p}_{i,j,k}\right) \right] - \alpha_{i,j,k} \quad (2.12)$$

Step 5: Estimate the Jacobian matrix J as follows:

$$J = \begin{bmatrix} \frac{\partial r_{i,j=1,k=1}}{\partial C1_i} & \frac{\partial r_{i,j=1,k=1}}{\partial \gamma1_i} \\ \vdots & \vdots \\ \frac{\partial r_{i,j=1,k=m_1}}{\partial C1_i} & \frac{\partial r_{i,j=1,k=m_1}}{\partial \gamma1_i} \\ \frac{\partial r_{i,j=2,k=1}}{\partial C1_i} & \frac{\partial r_{i,j=2,k=1}}{\partial \gamma1_i} \\ \vdots & \vdots \\ \frac{\partial r_{i,j=2,k=m_2}}{\partial C1_i} & \frac{\partial r_{i,j=2,k=m_2}}{\partial \gamma1_i} \\ \vdots & \vdots \\ \frac{\partial r_{i,j=2n,k=1}}{\partial C1_i} & \frac{\partial r_{i,j=2n,k=1}}{\partial \gamma1_i} \\ \vdots & \vdots \\ \frac{\partial r_{i,j=2n,k=m_{2n}}}{\partial C1_i} & \frac{\partial r_{i,j=2n,k=m_{2n}}}{\partial \gamma1_i} \end{bmatrix} \quad (2.13)$$

In Eq. 2.13, the k^{th} instance expression for the partial derivatives is given below:

$$\frac{\partial r_{i,j,k}}{\partial C1_i} = \frac{1}{\gamma1_i} \left[1 - \exp\left(-\gamma1_i \bar{p}_{i,j,k}\right) \right] \quad (2.14)$$

and

$$\frac{\partial r_{i,j,k}}{\partial \gamma1_i} = \frac{-C1_i}{(\gamma1_i)^2} \left[1 - \exp\left(-\gamma1_i \bar{p}_{i,j,k}\right) \right] + \frac{C1_i \bar{p}_{i,j,k}}{(\gamma1_i)} \exp\left(-\gamma1_i \bar{p}_{i,j,k}\right) \quad (2.15)$$

Step 6: Estimate the incremental change in parameters:

$$\Delta \mathbf{L} = [\Delta C1_i \ \Delta \gamma1_i]^T = -[(\mathbf{J}^T \mathbf{J})^{-1} \mathbf{J}^T] \mathbf{r} \quad (2.16)$$

Step 7: Update parameters as:

$$\mathbf{L} = [C1_i \ \gamma1_i]^T = \mathbf{L} + \Delta \mathbf{L} \quad (2.17)$$

Step 8: Repeat step 4 to step 7 unless the L_2 norm of the incremental parameters $\Delta \mathbf{L}$ is less than a tolerance value, i.e.,

$$\|\Delta \mathbf{L}\|_2 \leq t_{tol} \quad (2.18)$$

3 Experimental Results from Fatigue Tests

In our previous work [28], we conducted stroke (or crosshead displacement) controlled fatigue tests for 508 LAS base metal. The fatigue test data were used to estimate the time-dependent parameters utilizing a cyclic-plasticity model, and the results were compared with the corresponding time-independent parameters estimated from tensile test data. However, the parameters should be able to capture the evolution of the material behavior under realistic loading conditions, which may vary by loading amplitude. With this in mind, we conducted a few additional fatigue tests under stress-controlled conditions and with different amplitude conditions: constant, variable, and random grid-load-following amplitude.

The constant-amplitude stress test is used as a baseline experiment to compare the estimated parameters with those estimated from a stroke-controlled experiment. From our earlier work [26] we found that, although the constant-amplitude fatigue test can be used for estimating time-dependent material properties, the estimated material properties are sensitive to loading amplitude. To avoid the issues of amplitude dependence on material properties, we conducted a few variable-amplitude stress-controlled fatigue tests and used those data to estimate amplitude-independent parameters. Additionally, few fatigue tests were conducted under grid-load-following random loading conditions to examine the material behavior under realistic loading situation. In this section, the resulting fatigue test data are presented.

All the tests were conducted with small hourglass type specimens. Two test setups were used for fatigue tests in air and under PWR coolant water condition. The details of the test setups and environmental control can be found in a previous Argonne report [28]. For in-air fatigue tests, a precision high-temperature extensometer was used to measure the gauge-area strain. For PWR environmental tests, an extensometer couldn't be used for gauge-area strain measurement due to a water-tight autoclave in the experimental assembly. To determine the strain of the specimens during PWR environmental tests, stroke (crosshead displacement) measurements from PWR water tests were used along with the stroke-strain mapping functions generated from the in-air fatigue tests. The details of the generation of stroke-strain mapping functions from in-air test data and the prediction of strain data from stroke measurements during a PWR environment test can be found in a previous Argonne publication [35].

Multiple fatigue tests at various loading and environmental conditions were conducted. The test conditions along with Test ID are presented in Table 3.1. For the sake of comparison, the results from previous [28] strain-controlled tensile test (ET-T08) and stroke-controlled fatigue test (ET-F24) are used in this report. The test condition of the ET-T08 tensile test and ET-F24 fatigue test are also mentioned in Table 3.1.

Table 3. 1 Test conditions for 508 LAS base metal tensile and fatigue tests.

Test ID	Test Condition
ET-T08	In air, 300 °C, strain control, tensile test [28]
ET-F24	In air, 300 °C, stroke control, stroke amplitude = 0.1812 mm (equivalent to stress at 0.5% strain) fatigue test [28]
ET-F28	In air, 300 °C, stress control, constant amplitude = 447.5 MPa (equivalent to stress observed at 0.5% strain during similar condition tensile test*) fatigue test
ET-F31	In air, 300 °C, stress control, variable amplitude = 201.8 MPa to 466 MPa fatigue test
EN-F32	PWR water, 300 °C, stress control, variable amplitude = 201.8 MPa ~ 466 MPa fatigue test, Water chemistry: 1000 ppm B as H ₃ BO ₃ , 2 ppm Li ⁺ as LiOH, 20% H ₂ /bal. N ₂ cover gas, and DO < 5 ppb
ET-F33	In air, 300 °C, stress control, grid-load-following random amplitude fatigue test,
EN-F34	PWR water, 300 °C, stress control, grid-load-following random amplitude fatigue test, Water chemistry: 1000 ppm B as H ₃ BO ₃ , 2 ppm Li ⁺ as LiOH, 20% H ₂ /bal. N ₂ cover gas, and DO < 5 ppb

*See Figure 3.1.

3.1 Constant-Amplitude Fatigue Test

One stress-controlled constant-amplitude fatigue test (ET-F28) was performed on LAS 508 base metal alloy in air at 300 °C. The results from a previous [28] tensile test on LAS 508 base metal alloy in air at 300 °C were utilized to select the amplitude of the fatigue test. Figure 3.1 shows the stress-strain graph from the tensile test. The value of the stress at 0.5% strain was used as amplitude for the fatigue test ET-F28. The experimental results from the fatigue test are shown Figures 3.2 and 3.3.

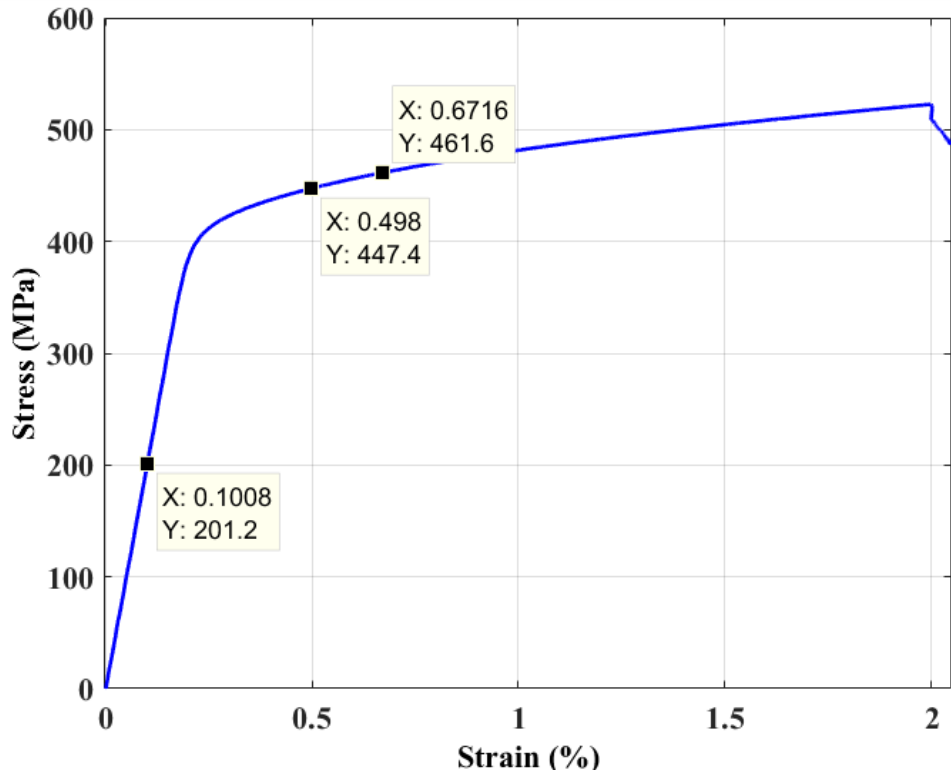


Figure 3. 1 Engineering stress-strain curve estimated from ET-T08 tensile test (air, 300 °C) data of 508 LAS base metal.

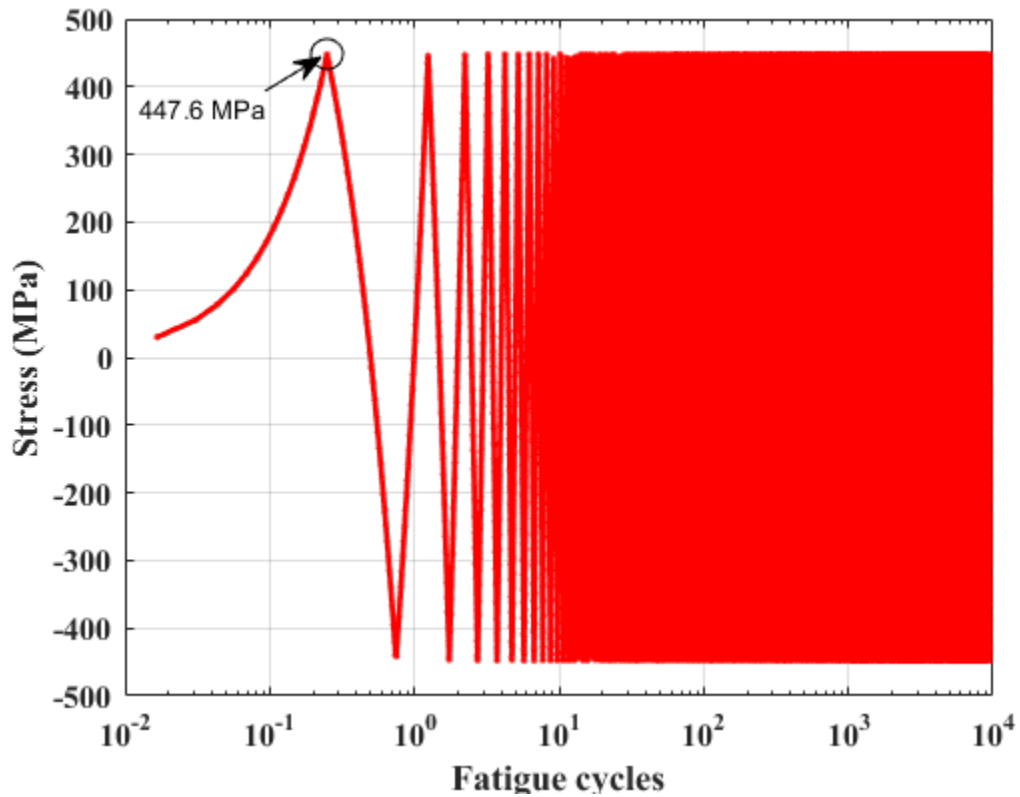


Figure 3. 2 Time history of applied stress for ET-F28 fatigue test.

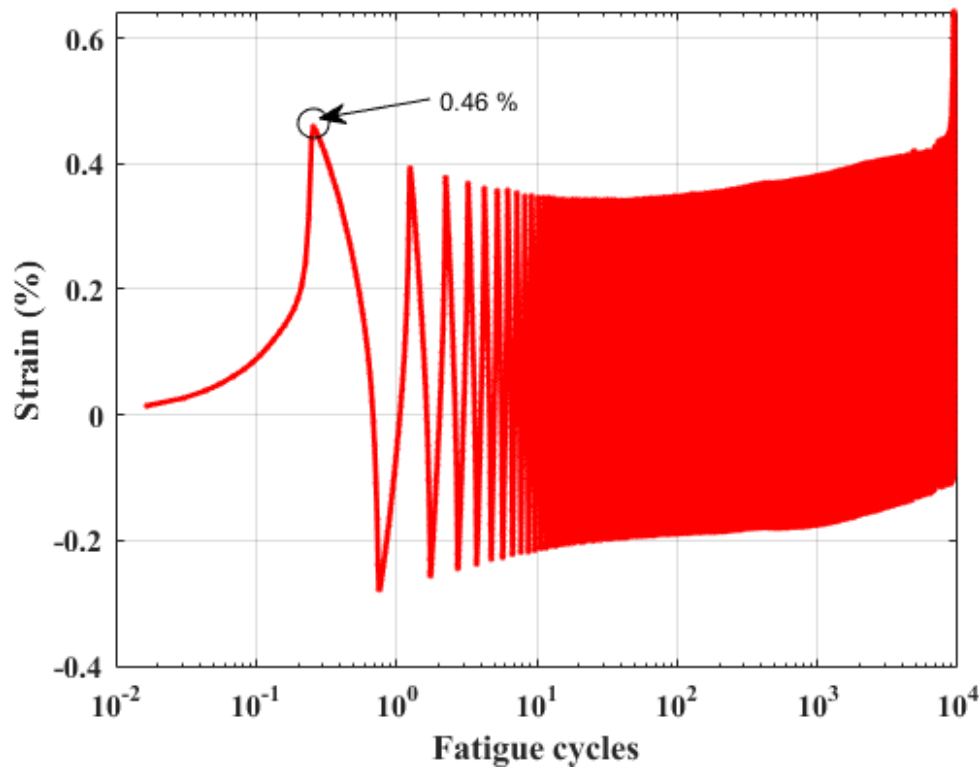


Figure 3. 3 Time history of observed strain for ET-F28 fatigue test.

3.2 Comparison between Stress-and Stroke-Controlled Fatigue Tests

Figure 3.4 shows the observed fatigue life of 508 LAS base alloy under stroke- and stress-controlled tests in air and at 300°C. The data indicate large difference in fatigue life under the two test modes. To examine the reason behind the difference, the maximum/minimum stress and strain are plotted as functions of fatigue cycles in Figures 3.5 and 3.6, respectively. As can be seen from Figure 3.5, the applied maximum and minimum stresses were constant during the stress-controlled test (ET-F28), while the stresses varied during the stroke-controlled test (ET-F24). Careful observation of the first few cycle's maximum/minimum values of stress indicated that the maximum tensile and compressive stresses during the stroke-controlled test were close to those estimated from the stress-controlled test, but the difference increased with time or fatigue cycles. During the stroke-controlled test, the maximum and minimum amounts of stroke were selected with the intention of applying similar stresses as in the stress-controlled test. However, due to the inherent nature of the stroke-controlled test and associated stress/strain hardening/softening, the stresses did not stay constant. The higher tensile and compressive stresses during the stroke-controlled test might have caused the specimen to break earlier.

Similar results can also be observed from the maximum/minimum strain vs. fatigue cycle data shown in Figure 3.6. The observed tensile and compressive strains were much higher in the case of the stroke-controlled than those observed during the stress-controlled fatigue test. Thus, quantification of the amplitude dependencies of the material model parameters is important for accurate modeling of the fatigue life of the nuclear components. However, it would require conducting many fatigue experiments to create a data base of material model parameters as a function of amplitude. Further, calculating different parameters each time the amplitude varies would require more computation time during mechanistic

modeling/simulation of the reactor components. It would be simpler and less time consuming if amplitude-independent parameters could be used during mechanistic simulation of the nuclear reactor components. To determine amplitude-independent parameters, we proposed a variable-amplitude fatigue test. The estimated parameters from variable-amplitude fatigue tests should be able to capture the amplitude dependency during modeling of the reactor components.

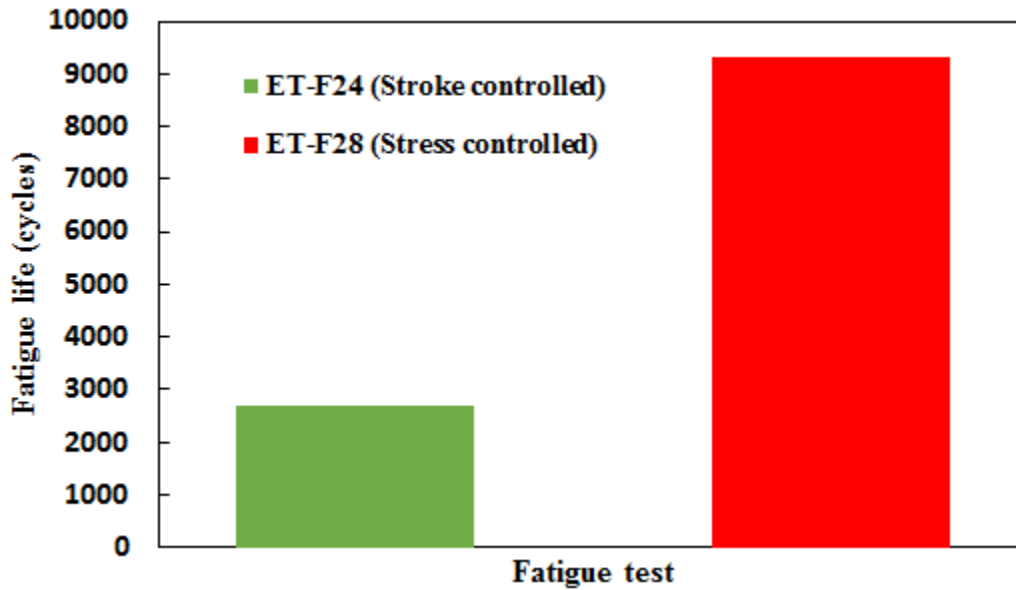


Figure 3. 4 Fatigue life of 508 LAS base alloy under two test modes (air and 300°C).

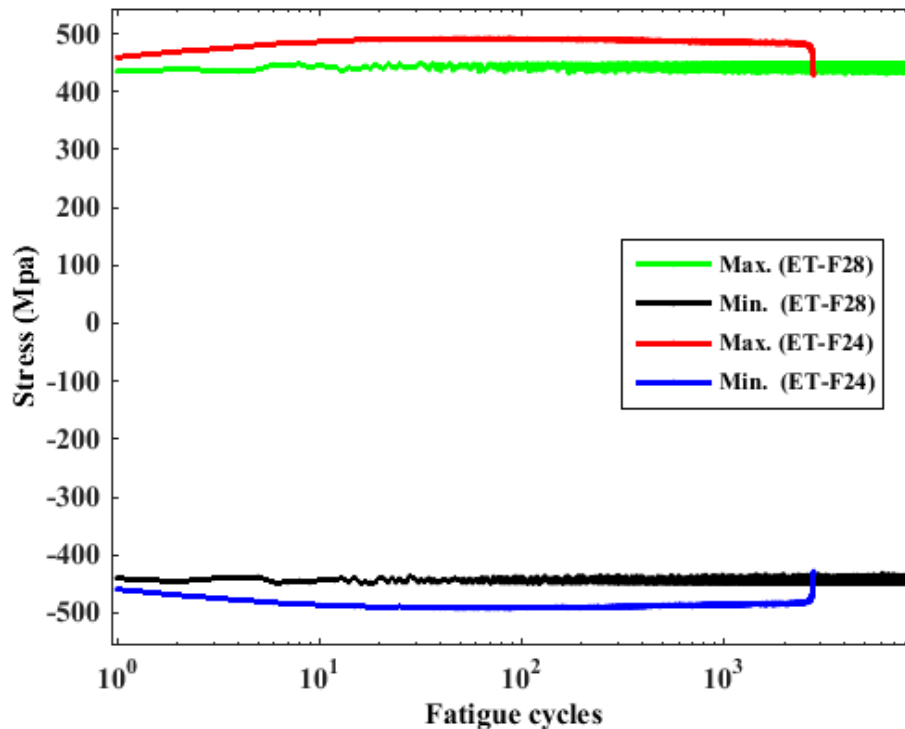


Figure 3. 5 Maximum/minimum stress for 508 LAS base alloy during two fatigue test modes (air and 300°C).

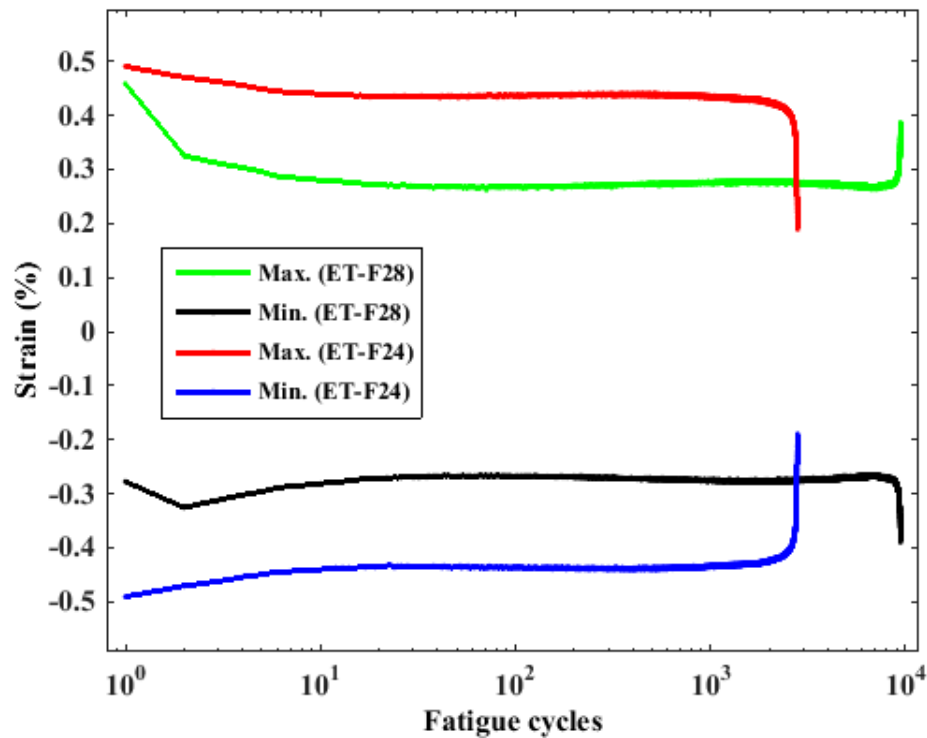


Figure 3. 6 Maximum/minimum strain for 508 LAS base alloy during two fatigue test modes (air and 300°C).

3.3 Variable-Amplitude Fatigue Tests

Stress-controlled variable-amplitude fatigue tests were conducted under the in-air and PWR coolant water conditions and at 300°C. The respective test IDs are ET-F31 and EN-F32, and the associated test conditions can be found in Table 3.1. During the variable-amplitude fatigue tests, the load amplitude was varied by gradually increasing from a minimum value (within the elastic limit, equivalent of 0.1% stress-strain curve shown in Figure 3.1) to a maximum value (equivalent of 0.67 % strain in the stress-strain curve shown in Figure 3.1), and then gradually decreasing to the minimum again. This gradual increase and decrease of load can be defined as block loading, with each block consisting of 12 fatigue cycles. A demonstration of the block loading during variable-amplitude fatigue is shown in Figure 2.1 in section 2.

Figure 3.7 depicts the applied variable-amplitude block loading during the ET-F31 test for the entire fatigue life of the specimen. The corresponding time histories of measured stroke and strain data from ET-F31 are shown in Figures 3.8 and 3.9, respectively. The stroke and strain measurement during the in-air fatigue test was used to generate the stroke-strain mapping relations. The details of the stroke-strain mapping procedures can be found from our earlier work [35]. The stroke-strain mapping relations obtained through the ET-F31 test were later used to predict strain from the measured stroke during the PWR environment test EN-F32. As mentioned earlier, an extensometer could not be used for gauge-area strain measurement during the EN-F32 test. An example comparison between measured and predicted strain (estimated from the stroke history using the generated mapping relations) for the ET-F31 in-air fatigue test is shown in Figure 3.10. Figures 3.11 and 3.12 show the stress-strain hysteresis plots of the first and last blocks obtained from ET-F31 test data, respectively.

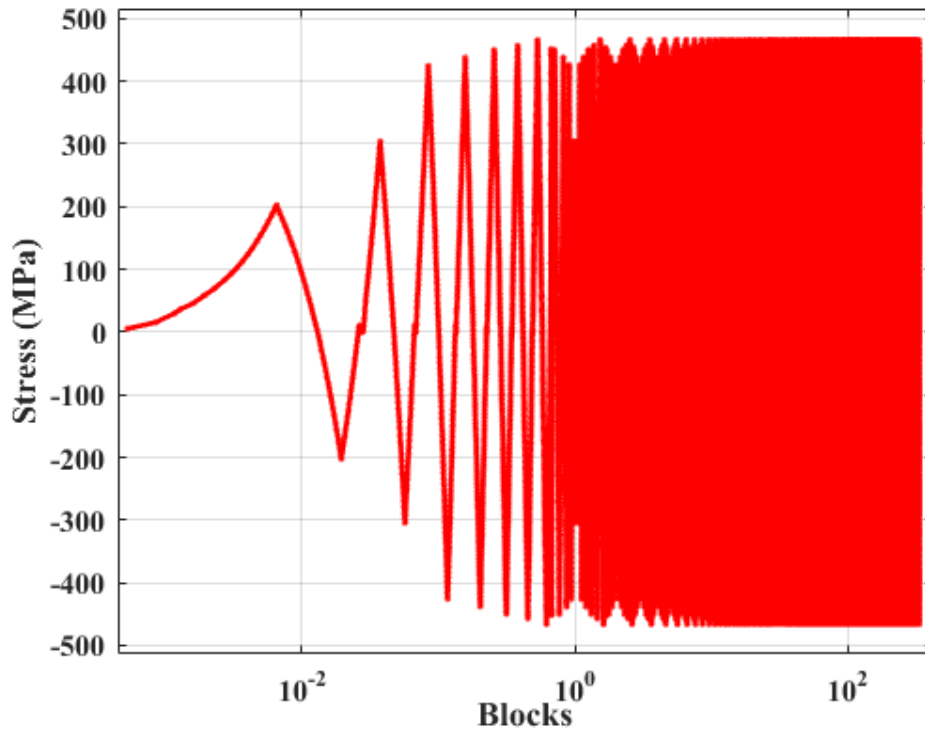


Figure 3. 7 Variable-amplitude block loading during ET-F31 fatigue test.

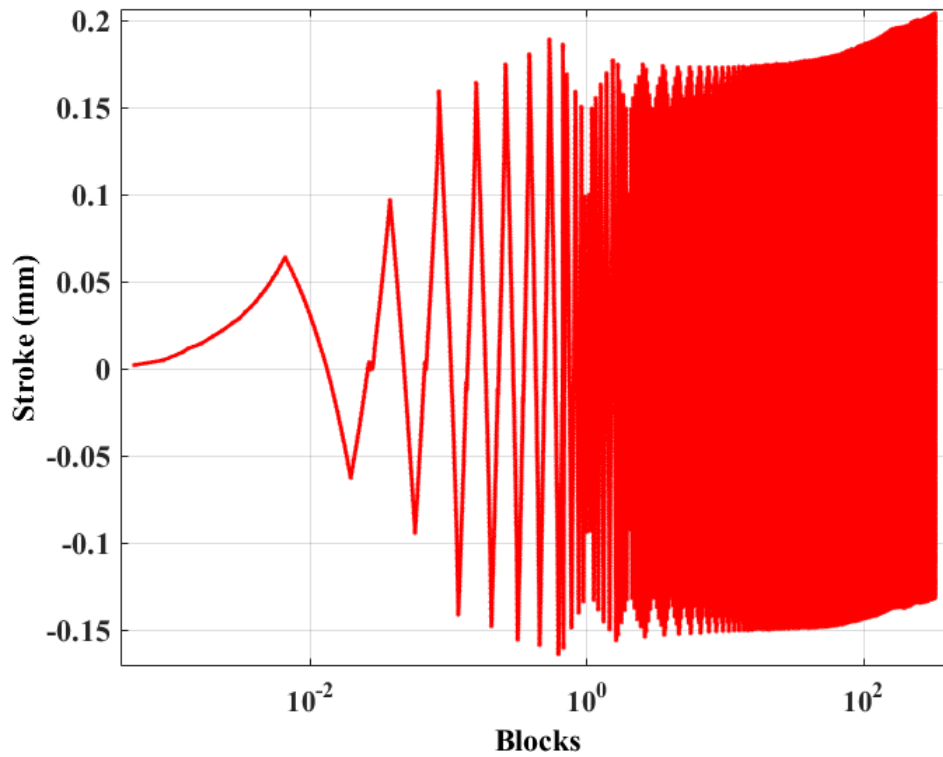


Figure 3. 8 Time history of measured stroke for ET-F31 fatigue test.

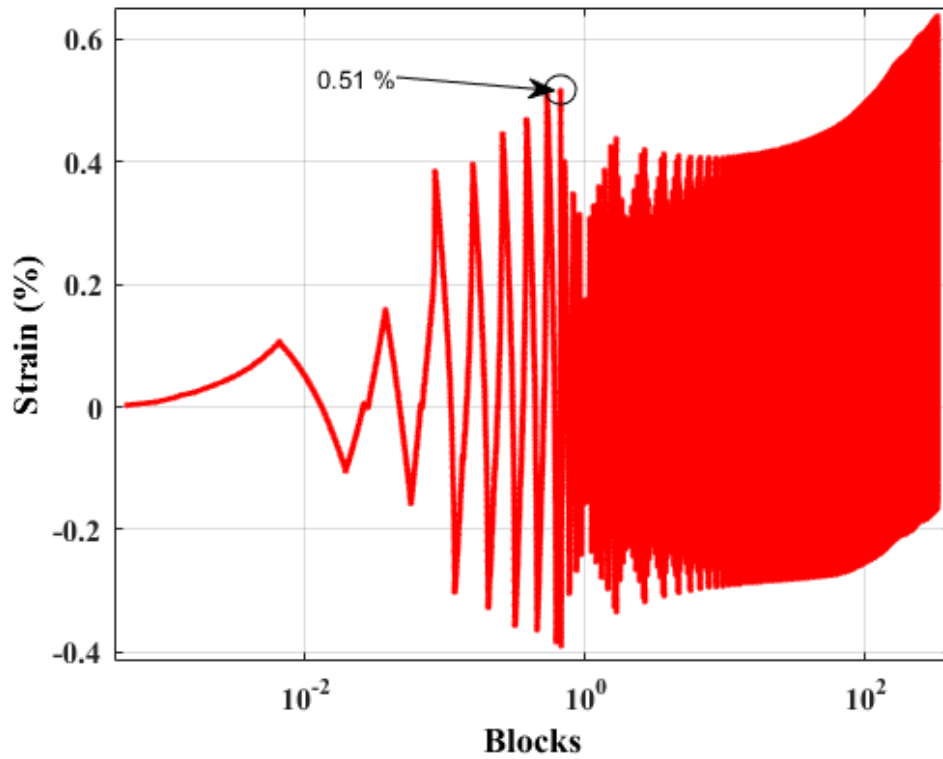


Figure 3. 9 Time history of measured strain for ET-F31 fatigue test.

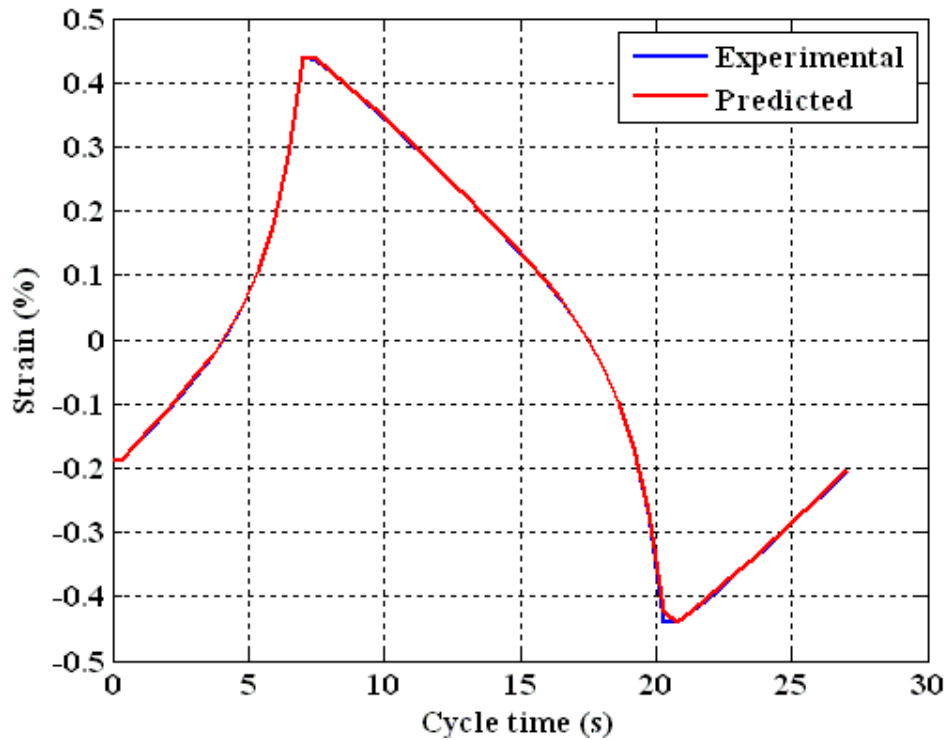


Figure 3. 10 Example comparison of strain predicted from stroke (using stroke-strain mapping relation) with strain obtained from ET-F31 fatigue test. The data correspond to fatigue cycle no. 7 in block no. 1 (see Figure 3.7).

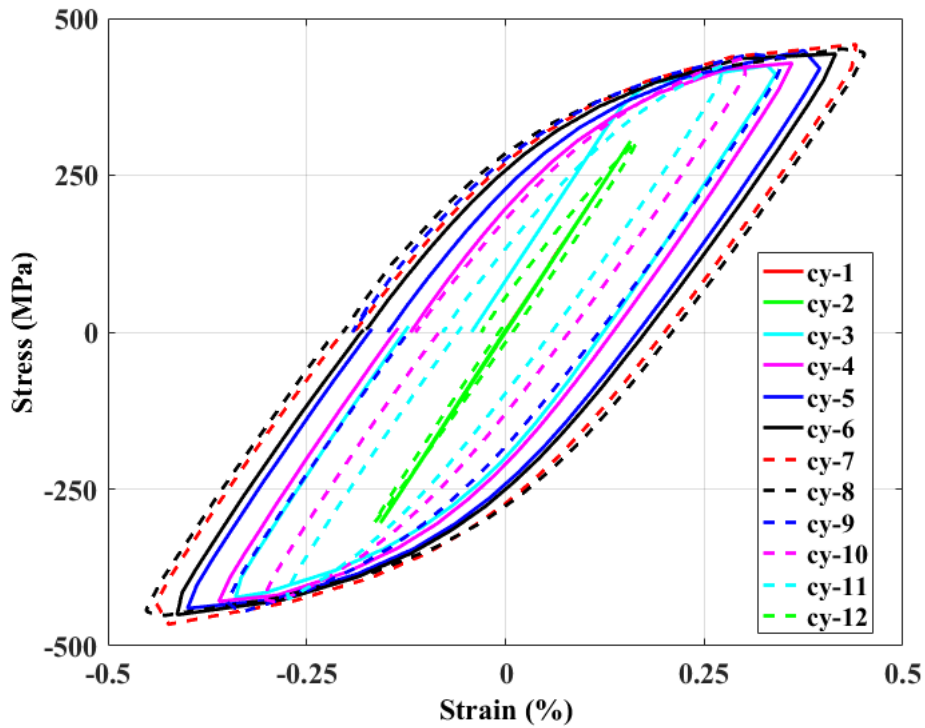


Figure 3.11 Stress-strain hysteresis plots of first block (for all 12 cycles within the block) obtained through ET-F31 fatigue test of 508 LAS base alloy under in-air and 300°C condition.

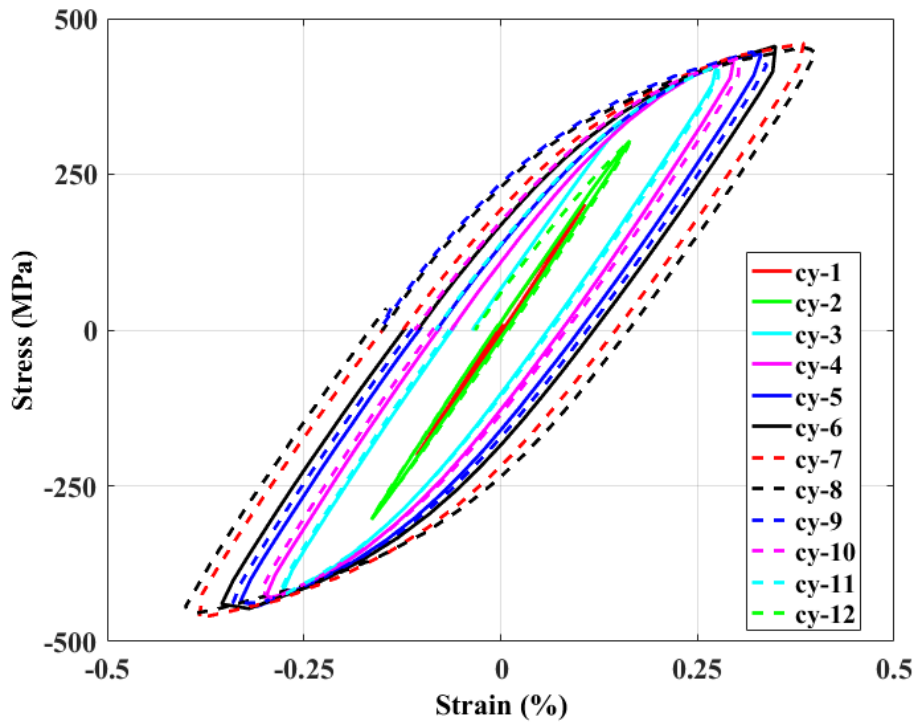


Figure 3.12 Stress-strain hysteresis plots (after removing the offset due to ratcheting strain) of last block (for all 12 cycles within the block) obtained through ET-F31 fatigue test of 508 LAS base alloy under in-air and 300°C condition.

The PWR test (EN-F32) was conducted using stress amplitudes same as in case of in-air test. The EN-F32 stress history is shown in Figure 3.13. Comparing Figure 3.13 with Figure 3.7 suggests that the loading profile for the PWR water test is not symmetric about $y=0$ axis, as in the case of the ET-F31 test. This asymmetry is due to the initial hydrostatic stress associated with the autoclave water pressure. This initial stress has been appropriately removed (as offset stress) from the EN-F32 stress history for further analysis, such as for material parameter estimation. The corresponding measured stroke history is shown in Figure 3.14. Using the stroke-strain mapping relations obtained from in-air fatigue test (ET-F31), we predicted the strain history of the PWR environment fatigue test (EN-F32). Note that the fatigue life of the specimen is different in the PWR environment than that in air. Thus, mapping of the blocks between two different test conditions was adjusted based on the fatigue life of the specimen in those test conditions. For example, for estimating the half-life cycle strain of the EN-F32 test, we used the corresponding half-life cycle stroke-strain parameters (obtained from ET-F31 test data). The predicted strain history of EN-F32 test is shown in Figure 3.15. The stress-strain hysteresis plots of the first and last blocks for the EN-F32 test are shown in Figures 3.16 and 3.17, respectively.

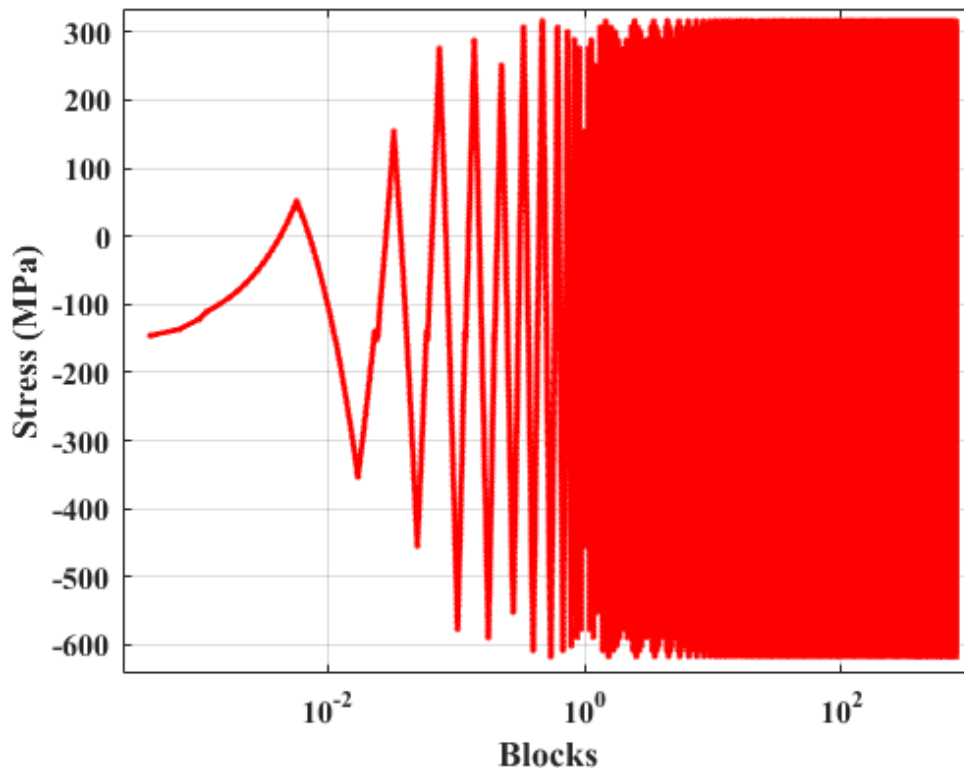


Figure 3. 13 Variable-amplitude block loading during EN-F32 fatigue test.

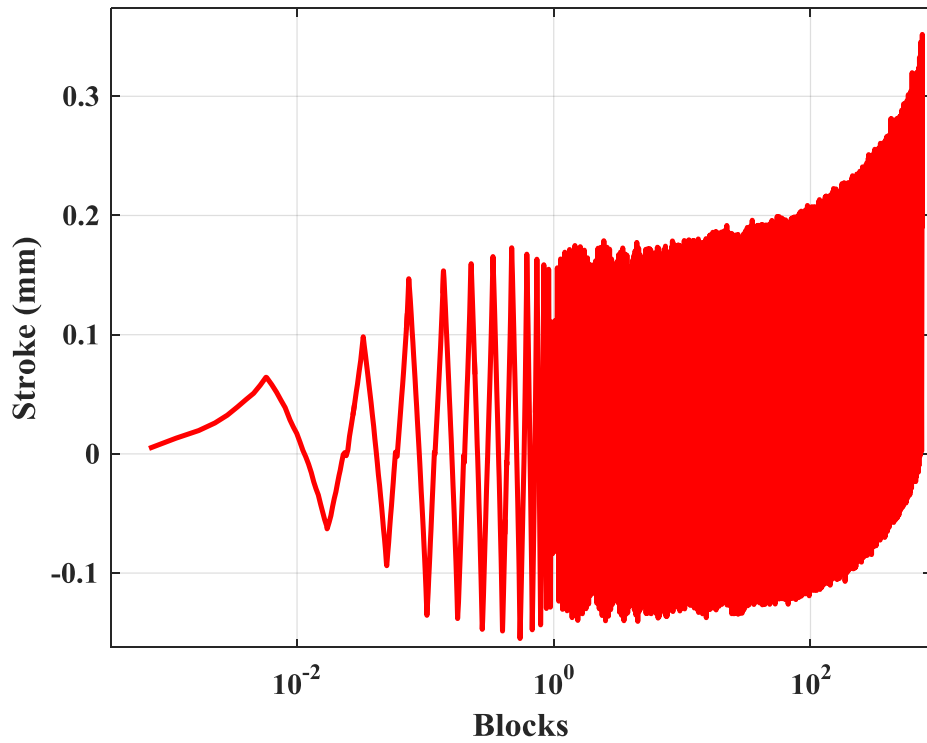


Figure 3.14 Time history of measured stroke for EN-F32 fatigue test.

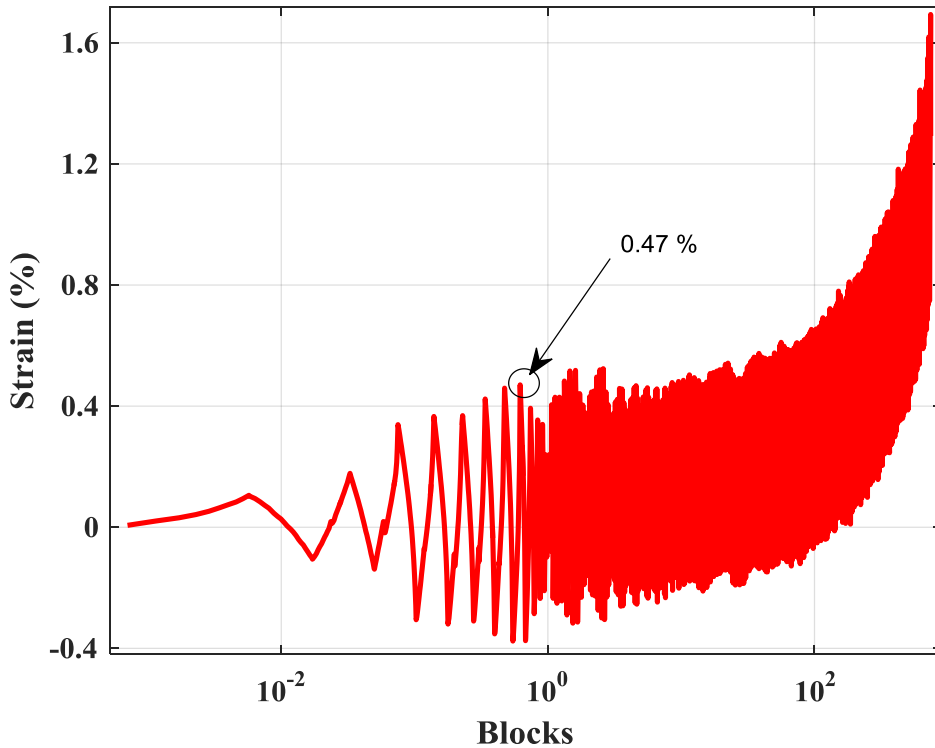


Figure 3.15 Time history of predicted strain (estimated from measured stroke, as shown in Figure 3.13, using stroke-strain mapping relation generated from ET-F31 in-air fatigue test) for EN-F32 PWR environment fatigue test.

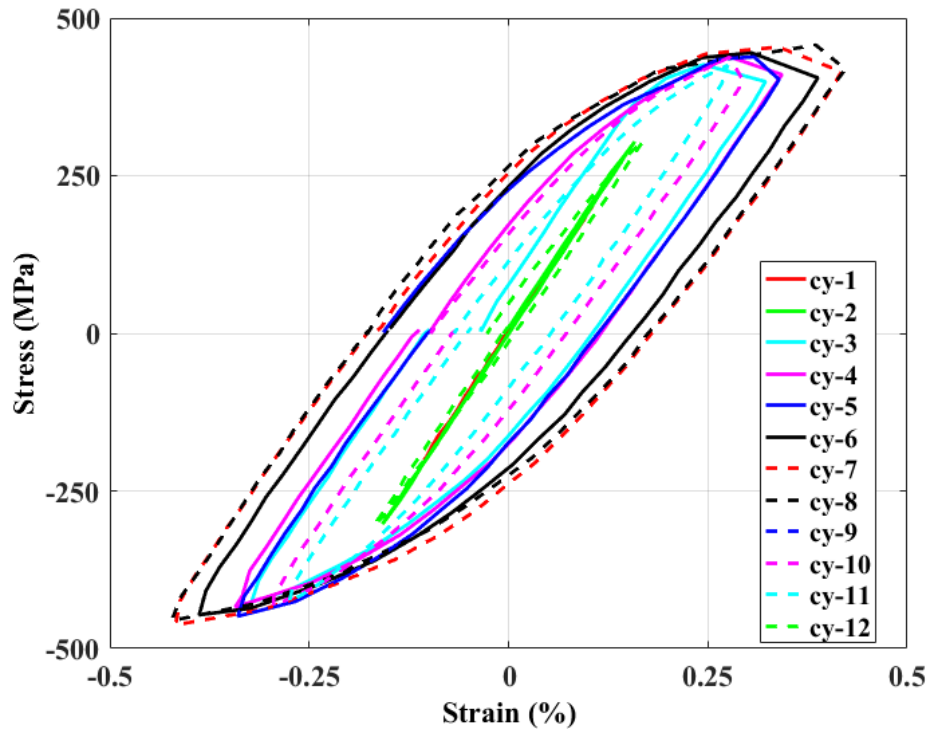


Figure 3. 16 Stress-strain hysteresis plots of first block (with all 12 cycles within the block) obtained through variable-amplitude fatigue test (ET-F32) of 508 LAS base alloy under PWR environment and 300°C condition.

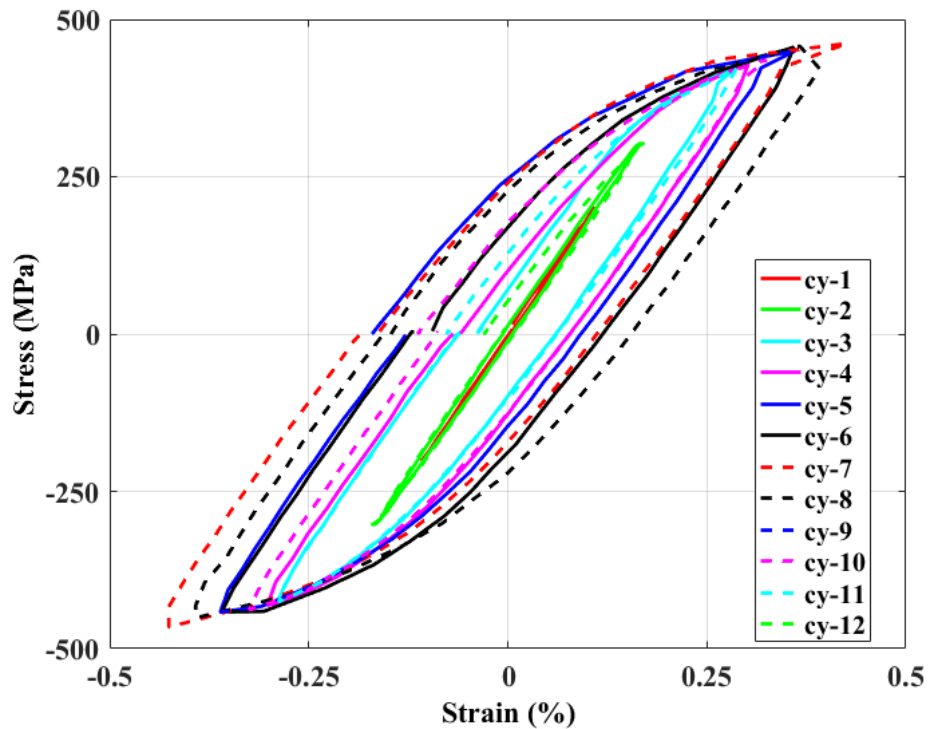


Figure 3. 17 Stress-strain hysteresis (after removing the offset due to ratcheting strain) plots of last block (with all 12 cycles within the block) obtained through variable-amplitude fatigue test (ET-F32) of 508 LAS base alloy under PWR environment and 300°C condition.

Figure 3.18 shows the block maximum and minimum strain from fatigue tests ET-F31 (in-air) and EN-F32 (PWR environment). In both cases, substantial strain hardening was observed for the first 10 to 15 blocks (equivalent of 120 to 180 cycles, with each block consisting of 12 loading cycles), and then the specimens were softened for the rest of the fatigue life. Due to the harsh nature of the PWR environment, the fatigue life of the specimen in the PWR environment can be lower than that in air. However, Figure 3.18 depicts the opposite due to a mistake made while programming the input of the ET-F31 fatigue test. According to Figure 2.1, the loading period of the 8th fatigue cycle in each block should be 22 s, but by mistake the loading period was entered as 2.2 s. This means the loading rate for that particular fatigue cycle of ET-F31 test was 10 times the intended rate. As the amplitude of that fatigue cycle was in the inelastic region, the corresponding loading rate effect had a substantial impact on the specimen and might have caused it to fail early. A repeat of ET-F31 test will be conducted in the future. However, the aim of the discussed results in this preliminary report is to describe the methodology followed for the material model and analytical model through some representative results. In so doing, we have not considered the effect of the loading rate, only the effects of time and the loading amplitude.

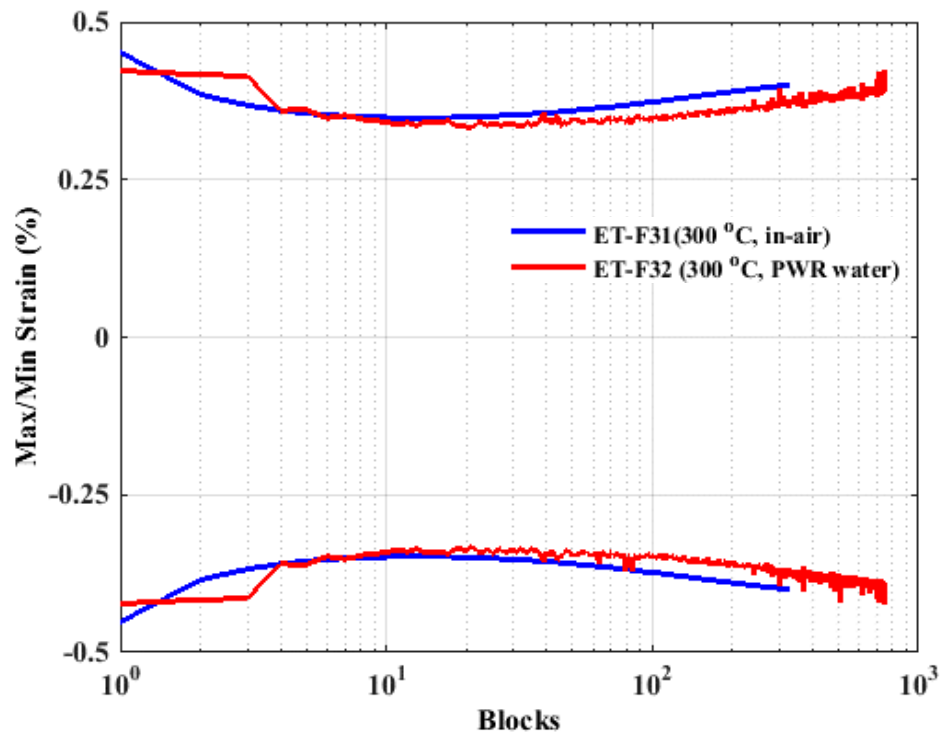


Figure 3. 18 Maximum and minimum strain for 508 LAS base metal alloy fatigue tested under stress-controlled variable-amplitude loading for in-air (ET-F31) and PWR environment (ET-F32) conditions.

3.4 Grid-Load-Following Random Amplitude Fatigue Tests

Grid-load-following random amplitude fatigue tests of 508 LAS base metal specimens were conducted under in-air (ET-F33) and PWR coolant water (EN-F34) conditions and at a temperature of 300°C. The finite element simulation results from the thermal-mechanical stress analysis of a RPV nozzle (with preexisting axial crack) were used to determine the loading condition during these tests. While the details of the grid-load-following condition along with the finite element modeling and simulation results can be found in our previous work [29, 30], representative results are briefly presented here to illustrate the connection between the discussed experimental results and previously performed modeling work. For example, Figure 3.19 depicts the solid model of the RPV, for which a stress state at a cracked nozzle was considered in the fatigue tests. The simulated shape and location of preexisting axial cracks on the left HL nozzle are illustrated in Figure 3.20. An example stress profile near the nozzle area at a typical full power condition is shown in Figure 3.21. A typical nodal location in the highly stressed location of the cracked region (Figure 3.21) was used to estimate the stress history for the discussed grid-load-following fatigue tests (ET-F3 and EN-F34). Figure 3.22 depicts the Von-Mises stress history over an entire fuel cycle at the selected node. This figure shows the Von-Mises stress histories at maximum stressed location in the axially cracked left HL nozzle and the corresponding maximum stressed element in the un-cracked right HL nozzle. Note that Figure 3.22 shows the estimated stress levels at a local stress concentration region (for a typical finite element node), which do not necessarily affect the overall structural integrity of the nozzle. In preliminary experimental work, we considered the cracked region stress profile (Figure 3.22) as loading input for the grid-load-following fatigue tests ET-F3 and EN-F34. This was done to check how the strain state of the 508 LAS specimen was affected by the input load/stress history. Based on the preliminary test results, future load-following tests will be planned. The experimental results using the simulated stress profile are discussed below.

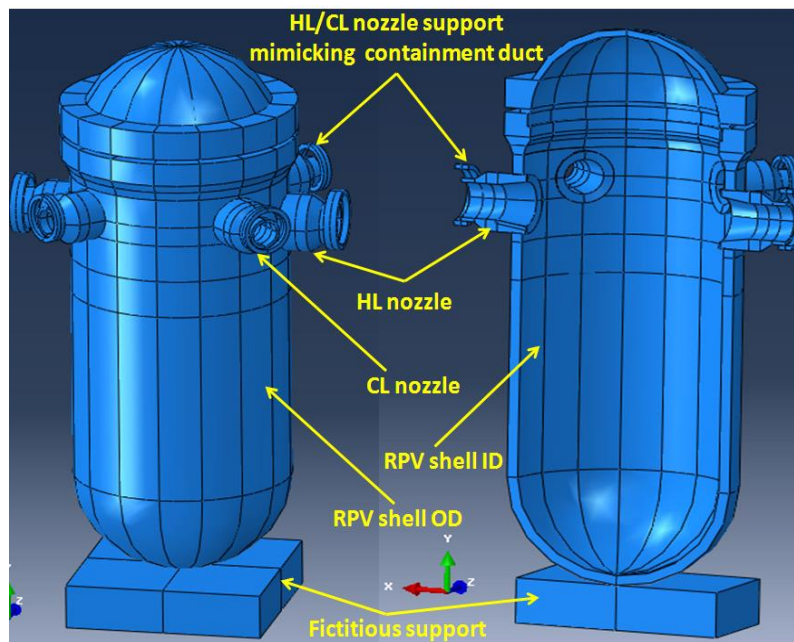


Figure 3. 19 Model of RPV and its hot leg (HL) and cold leg (CL) nozzles [29].

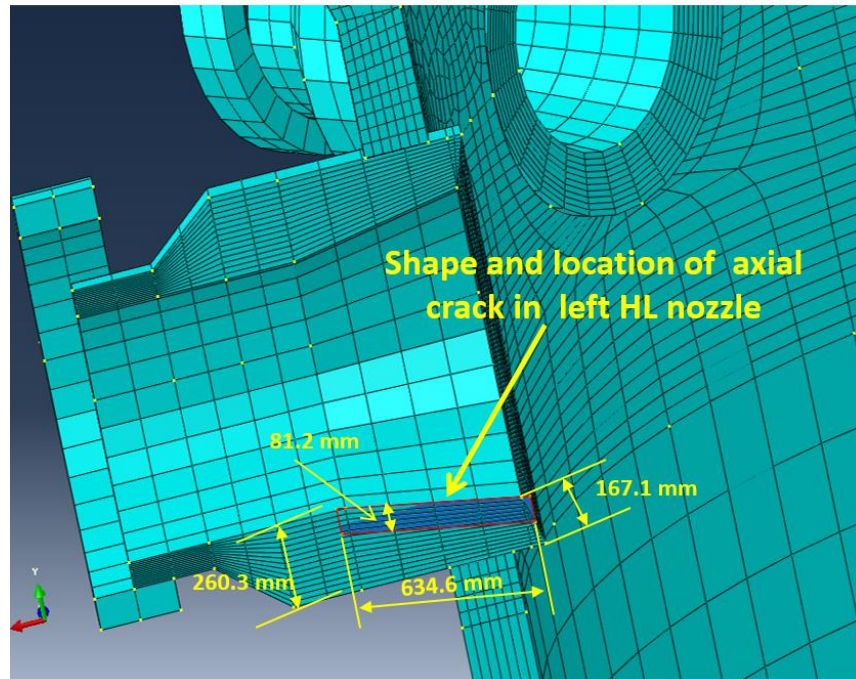


Figure 3. 20 Shape, approximate size, and location of axial crack in left HL nozzle of RPV [29].

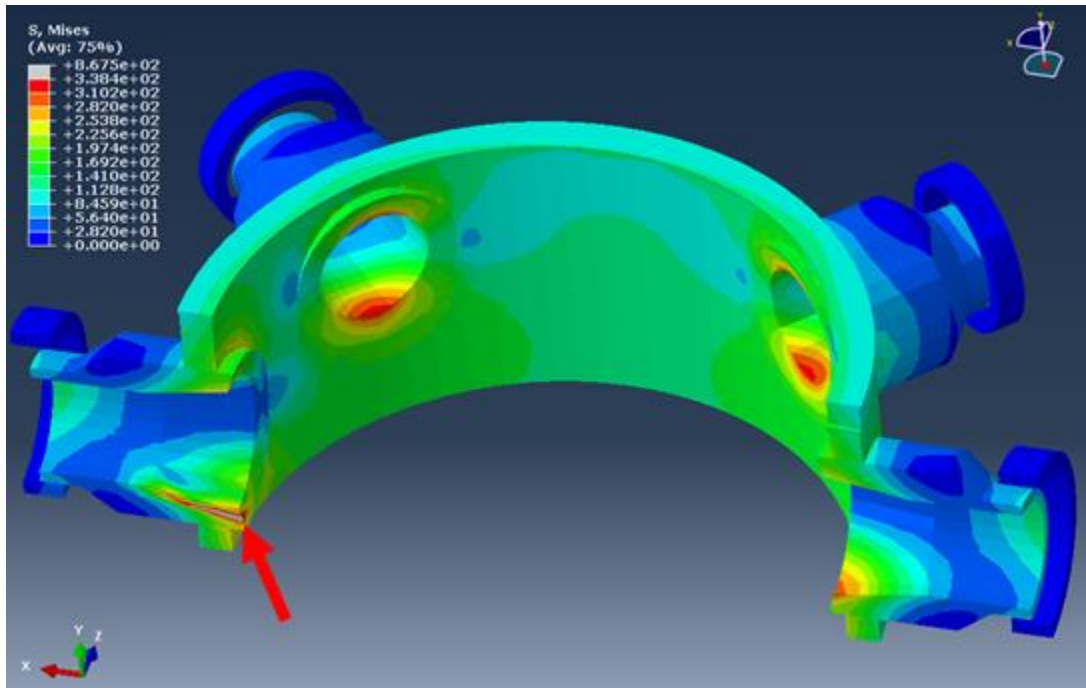


Figure 3. 21 Von-Mises stress contour at a typical full power condition [29]. Arrow showing a typical nodal location, where stress states are used as fatigue test loading input for grid-load-following fatigue tests (ET-F3 and EN-F34).

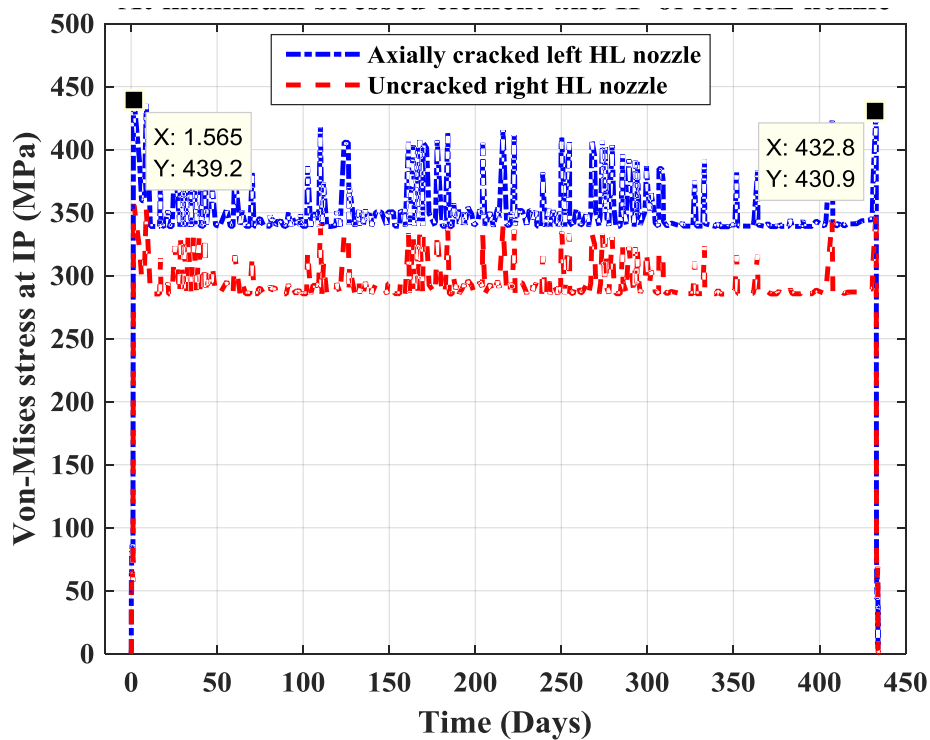


Figure 3. 22 Von-Mises stress histories at maximum stressed node in left HL and the corresponding maximum stressed node in right HL nozzle [29].

The simulated stress history shown in Figure 3.22 was scaled down along the time axis to generate the input load for the grid-load-following fatigue tests. This was necessary to finish the test in a reasonable time. For example, the scaled-down stress history used for the ET-F33 test had a block period of 1560 seconds. First the ET-F33 test was conducted, then the EN-F34 test. Because the ET-F33 test took a long time (for reasons discussed below), the time scale of the input stress history was further reduced for the EN-F34 test-to approximately 200 seconds. Both the ET-F33 and EN-F34 tests were conducted under the stress-controlled condition. The ET-F33 test was conducted under the in-air condition, whereas the EN-F34 test was conducted under the PWR water condition (Table 3.1). Figure 3.23 shows an example screen shot of the control panel during 1st block loading of EN-F34 test. In this figure, the Graph 1 shows time versus stress (ksi) and stroke (mil), Graph 2 shows stroke versus stress, Graph 3 shows temperature reading at various locations of autoclave, and Graph 4 shows the cycle versus max./min. of frame cross-head displacement (stroke) and actuator position measurements (which was updated at the end of each block).

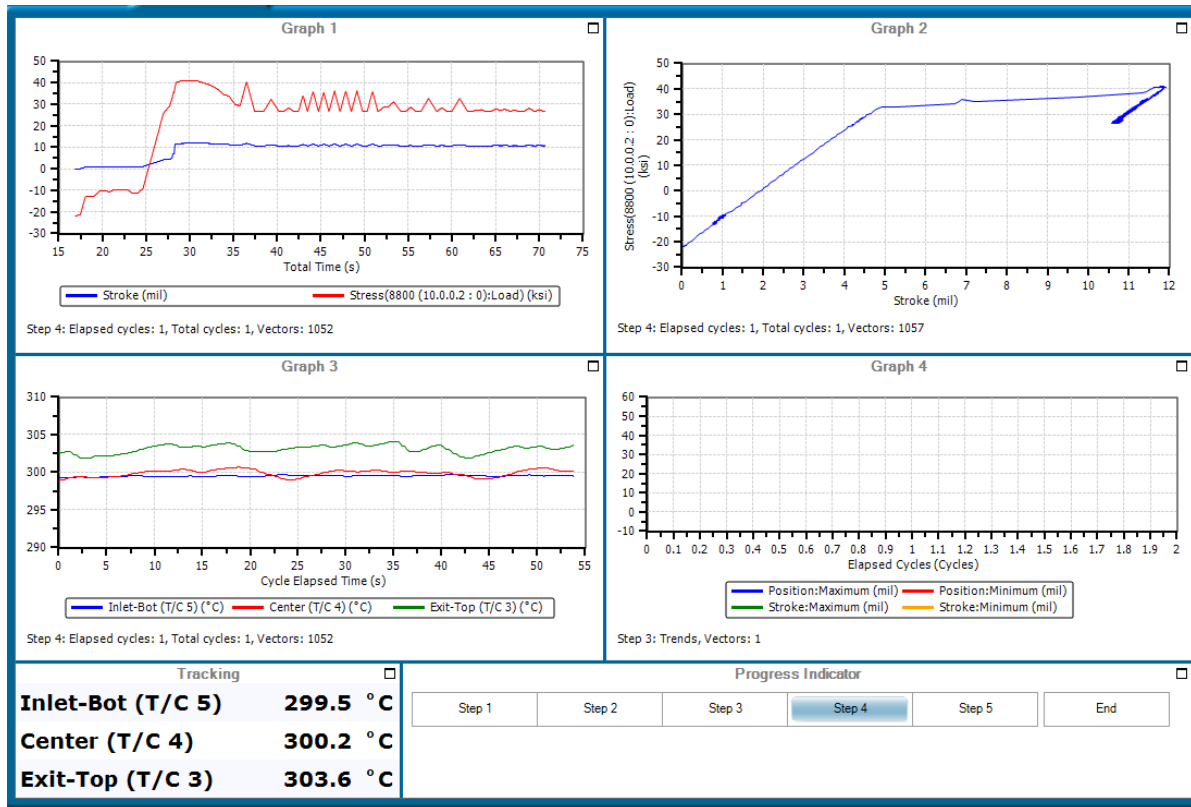


Figure 3.23 Example screen shot of the control panel during 1st block loading of EN-F34 test.

The observed stroke and strain history for the ET-F33 test is presented in Figures 3.24 and 3.25, respectively. For this test, both the stroke and strain were measured to generate a mapping function between stroke and strain. Figure 3.26 shows an example of the stroke-versus-strain data from this test and the regenerated/predicted stroke-versus-strain data obtained from the mapping function. This mapping function later was used to estimate the strain for the PWR water test (EN-F34 test) from the corresponding stroke measurements. For the PWR water test, an extensometer could not be used to measure the gauge area strain due to the use of a small water-tight tube autoclave. Figure 3.25 indicates that substantial strain was generated during ET-F33 test, although we expected a maximum strain of 0.5%. Based on the ET-T08 tensile test curve shown in Figure 3.1, we expected a maximum strain of 0.5%, corresponding to the maximum intended input stress of 439.2 MPa. Note that the ET-F08 specimen was tested at the same condition (in air at 300°C) as the ET-F33 test. Because of the high strain generated during the first loading block, the ET-F33 specimen was strain hardened and thus did not fail even after 888 loading blocks, after which the test was terminated.

Similar results were observed for the EN-F34 fatigue test. Note that ET-F33 specimen was fabricated from a pristine 508 LAS plate, whereas, EN-F34 specimen was fabricated from the 508 LAS heat affected zone (HAZ) of a 508 LAS – 316 SS dissimilar weld plate. Figure 3.27 shows the location of the specimen with respect to the cross-section of weld plate. The observed stroke and estimated strain profile for EN-F34 test are shown in Figures 3.28 and 3.29, respectively. Figure 3.29 shows that, for EN-F33, the strain amplitude crossed more than 1% within the first loading block. Similar to the case for the ET-F33 specimen, this led to a strain hardening of the EN-F34 specimen. The EN-F34 specimen thus didn't fail even after thousands of loading blocks, and the test was terminated after 10,000 loading blocks. Figure

3.30 shows the hysteresis (strain versus stress) curves for first 64 blocks of the EN-F34 test. The curves indicate an initial strain hardening (that observed during the first block period), then subsequent elastic cycling. The high strain generation and subsequent elastic shakedown could be due to a combination of material effects, which are a function of loading amplitude and rate. They might also be due to following a pure tensile-tensile loading profile, which didn't allow the material to reverse back some of the plastic strain as it would have recovered in the case of a conventional tensile-compression fatigue test. Due to this high strain generation, the ET-F32 and EN-F34 fatigue test results were not further considered for analytical modeling validation (see Section 5). Since the analytical models are developed based on material parameters, those results are a function of much smaller strain amplitudes. The above results show the complexity in conducting stress-controlled fatigue tests, particularly under prototypical (in this case, tensile-tensile) loading conditions. The test will be repeated in the future to ascertain the exact reason of initial strain hardening and subsequent elastic shakedown.

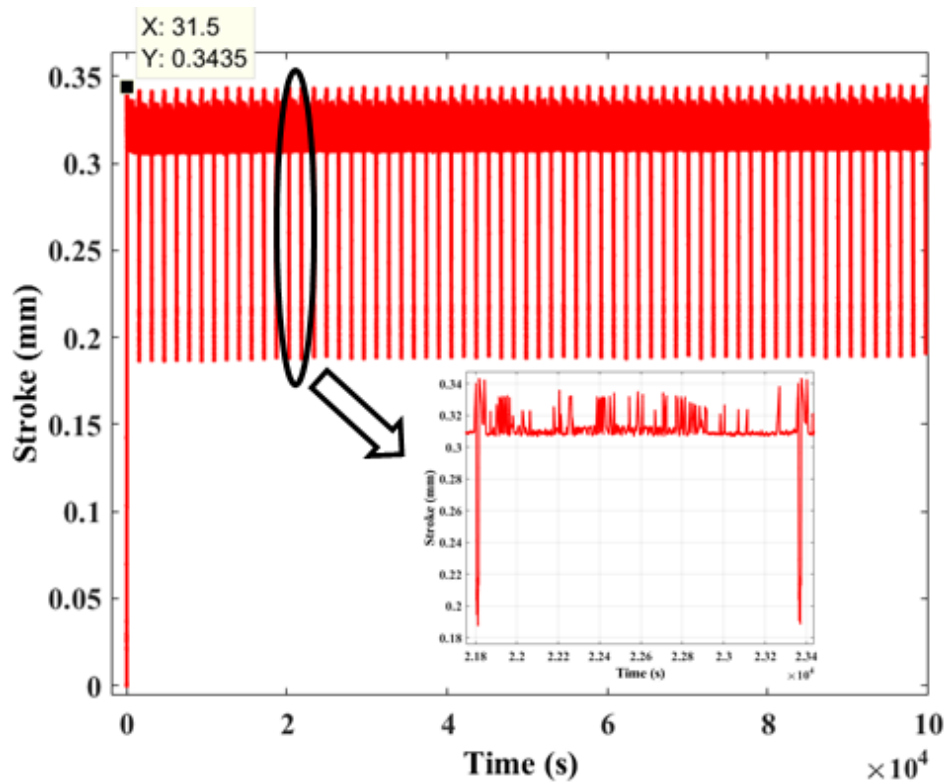


Figure 3.24 Time history of measured stroke (frame cross-head displacement) for ET-F33 fatigue test.

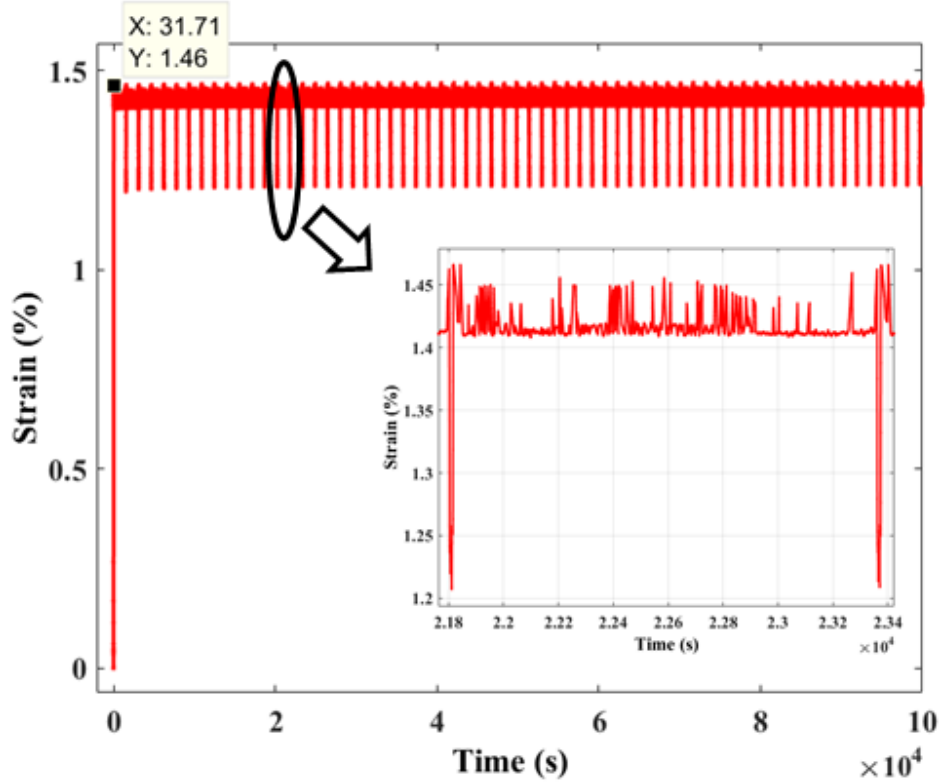


Figure 3.25 Time history of measured strain for ET-F33 fatigue test.

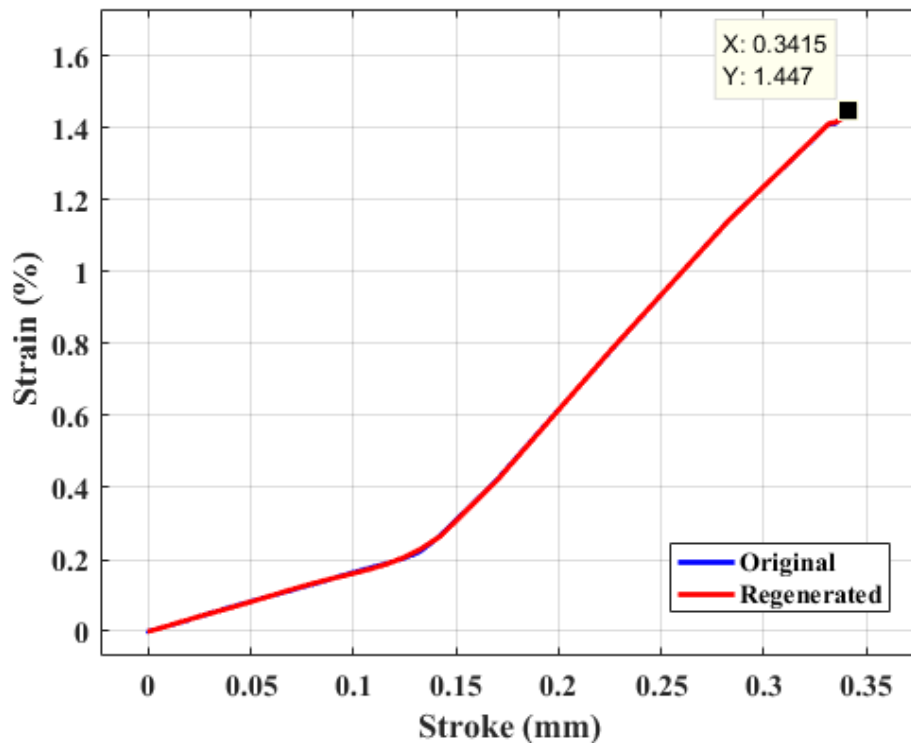


Figure 3.26 Example stroke-versus-strain mapping results for ET-F33 fatigue test.

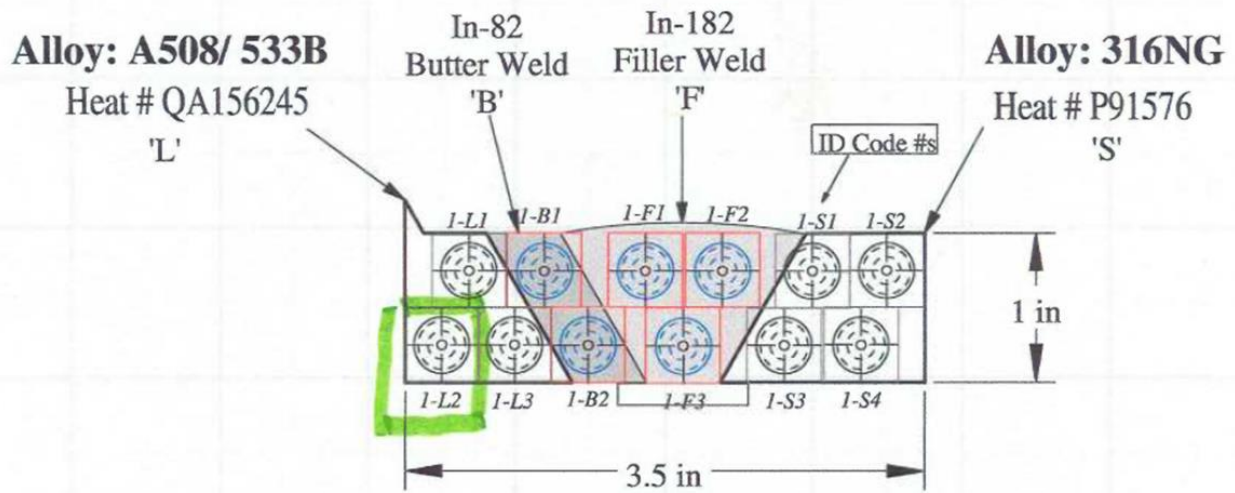


Figure 3. 27 Schematic showing the cross-section of 508 LAS- 316 SS dissimilar metal weld plate. The green highlighted block shows the location of EN-F34 fatigue specimen.

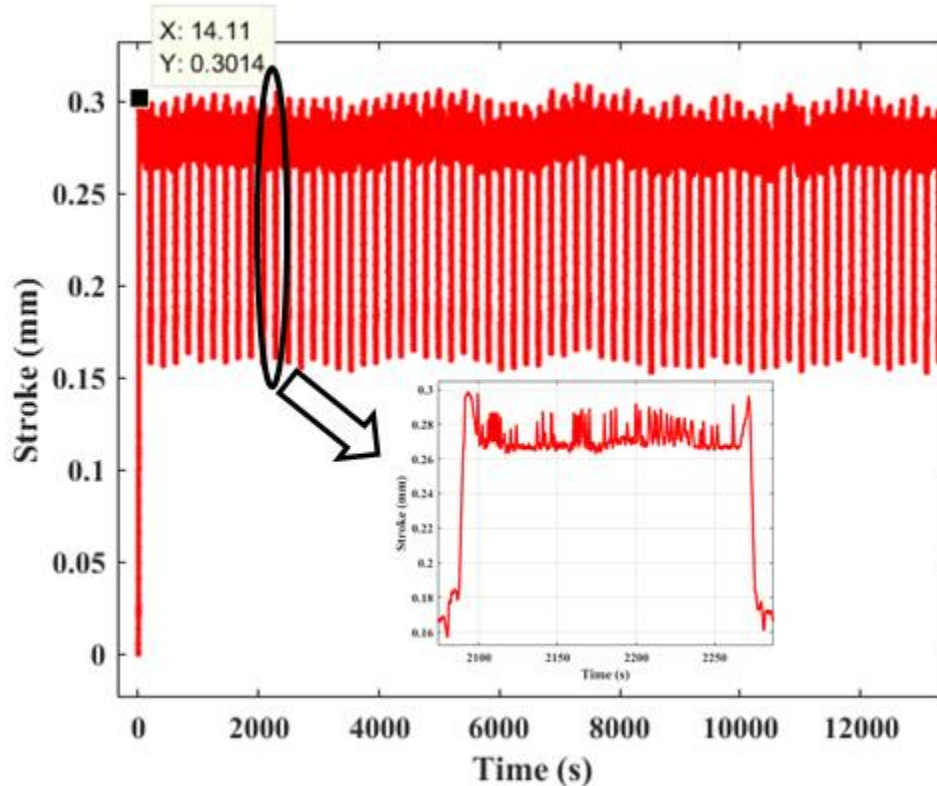


Figure 3. 28 Time history of measured stroke (frame cross-head displacement) for EN-F34 fatigue test.

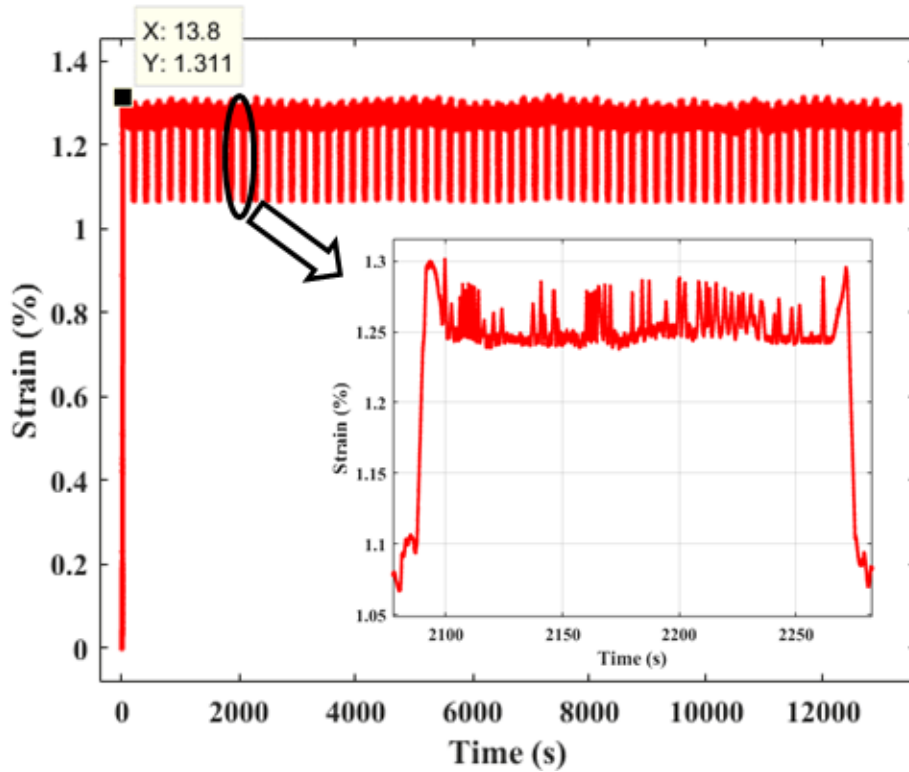


Figure 3. 29 Time history of estimated strain for EN-F34 fatigue test.

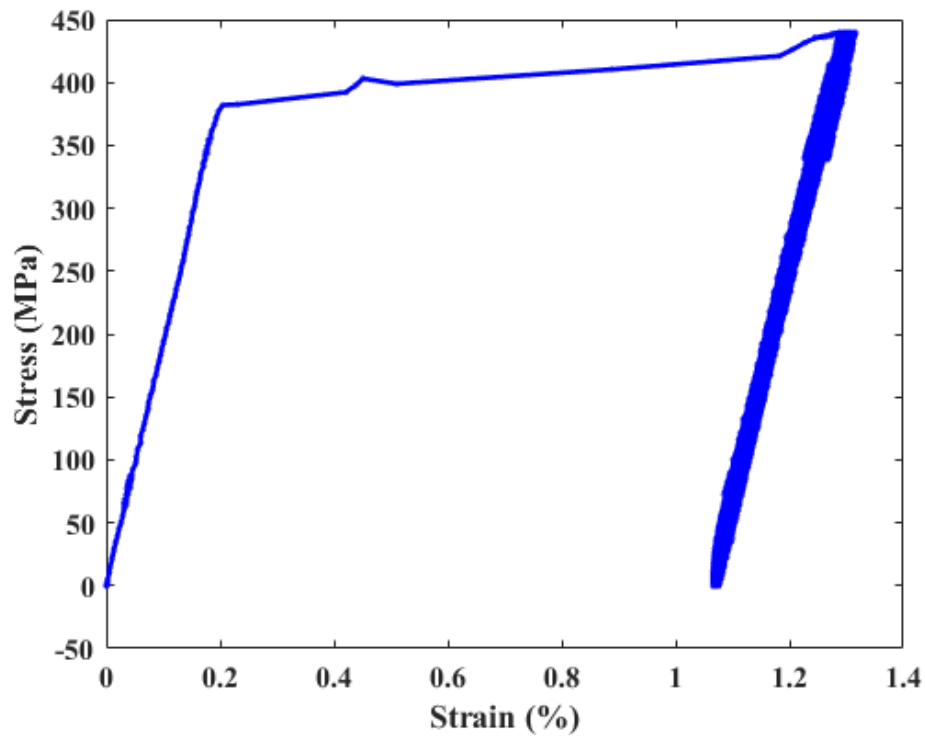


Figure 3. 30 Hysteresis (strain-versus-stress) curves for first 64 blocks of EN-F34 fatigue test.

4 Results from Material Parameter Estimation

A Chaboche-based nonlinear kinematic hardening model, along with a time-dependent, amplitude-independent material model, was presented in Section 2. The material model parameter estimations for 508 LAS base metal are discussed in this section. From our earlier work [26] we found that, although constant-amplitude fatigue tests can be used for estimating time-dependent material properties, the estimated material properties are sensitive to loading amplitude. We present here time-dependent-amplitude-dependent (cycle-by-cycle) parameters estimated from constant and variable amplitudes and time-dependent-amplitude-independent (block-by-block) parameters estimated from variable-amplitude fatigue test data. The details of the fatigue test data can be found in Section 3. The test conditions of the various fatigue experiments can be found in Table 3.1.

4.1 Cycle-by-Cycle Parameters Estimated from Constant-Amplitude Fatigue Tests

Using the cycle-by-cycle technique for parameter estimation as discussed in Ref. [28], the time-dependent (i.e., cycle-by-cycle) parameters for 508 LAS base metal alloys were estimated from a stress-controlled, constant-amplitude fatigue test (ET-F28) conducted in air at 300°C. The cyclic stress-strain curves were first converted into equivalent monotonic stress-strain curves, as shown in Figure 4.1. The data from a tensile test conducted under the same condition are also shown in the figure. The equivalent monotonic curves were further processed using the cycle-by-cycle parameter estimation technique [26-28]. The resulting process estimated the cyclic evolution of the parameters such as elastic modulus, elastic limit stress, and nonlinear kinematic hardening ($C1$ and $\gamma1$). In this report the nonlinear hardening parameters were estimated based only on the elastic limit stress, while in our previous work [28] they were also estimated based on a 0.05% offset yield limit stress for various stroke-controlled fatigue tests. As seen from Figure 4.1, selecting the 0.05% offset yield limit stress would exclude a substantial amount of the inelastic region in the equivalent monotonic stress-strain curves for the ET-F28 test; therefore, material parameters based on 0.05% offset yield limit stress were not estimated.

The cycle-by-cycle parameters estimated from a stress-controlled test (ET-F28) with 508 LAS base metal are shown in Figures 4.2 to 4.5. Figure 4.2 shows the time/cyclic variation of elastic modulus, whereas Figures 4.3 to 4.5 show the corresponding time/cyclic variation of elastic limit stress and the kinematic hardening parameters ($C1$ and $\gamma1$). The estimated parameters from a tensile test and a previously conducted stroke-controlled fatigue test (ET-F24) [28] are also shown in these figures for comparison. As seen from the curves, some of the parameters (e.g., $C1$ and $\gamma1$) vary significantly over the fatigue cycles, in contrast to the fixed parameters in the case of the tensile test. Therefore, elastic-plastic analysis of reactor components under cyclic loading may not produce accurate results if material parameters are considered purely based on tensile test data. The difference in cycle-by-cycle parameters between stress-controlled (ET-F28) and stroke-controlled (ET-F24) fatigue tests indicates that the test materials' behavior is sensitive to the amplitude. Note that a constant-amplitude stress was applied during the ET-F28 test while variation in stress amplitude was observed during the constant-amplitude, stroke-controlled (ET-F24) fatigue test. Similar test amplitude-related sensitiveness to estimated parameters was also observed for 316 SS base metal and reported in our earlier publication [26]. Thus, it is important to capture the amplitude independency in the estimated parameters for accurate elastic-plastic stress and fatigue

analysis of reactor components under cyclic loading. The corresponding results are discussed in the following section.

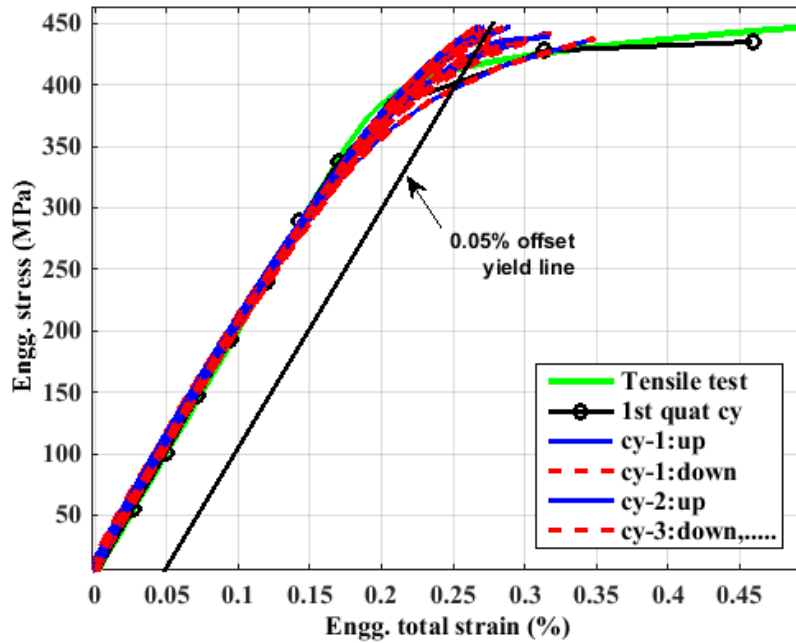


Figure 4.1 Equivalent monotonic stress-strain curves estimated from upward/downward cycle (for first 50 cycles) stress-strain curves data for ET-F28 fatigue test. Also given are the tensile test data (in-air, 300°C condition) and the 0.05% offset yield line.

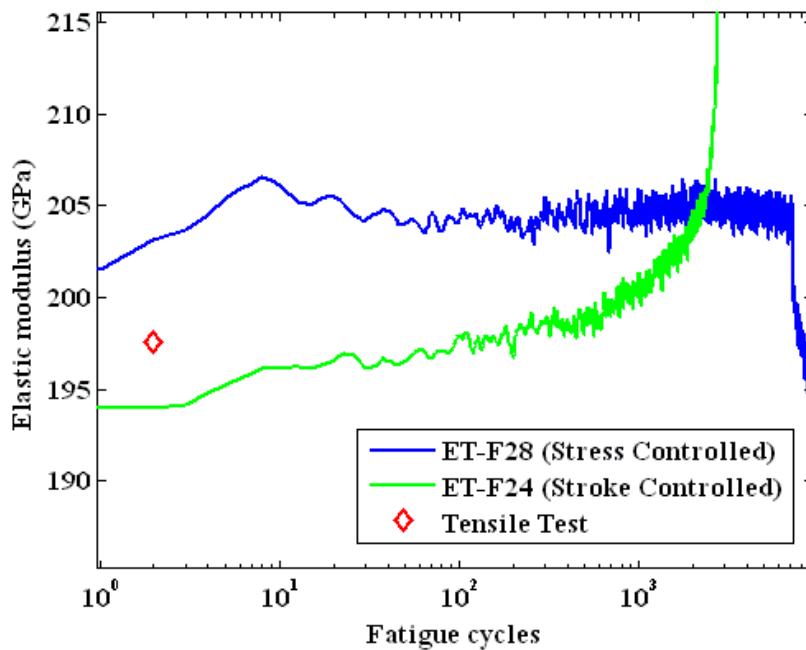


Figure 4.2 Cycle-by-cycle elastic modulus estimated from constant-amplitude fatigue tests. Corresponding parameter estimated from tensile test is also shown.

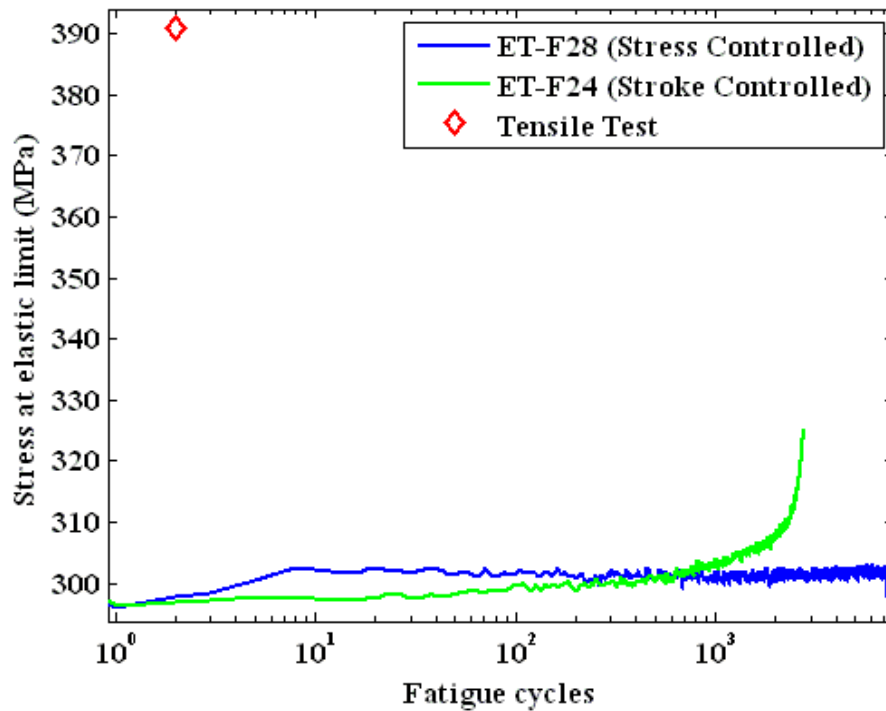


Figure 4.3 Cycle-by-cycle elastic limit stress estimated from constant-amplitude fatigue tests. Corresponding parameter estimated from tensile test is also shown.

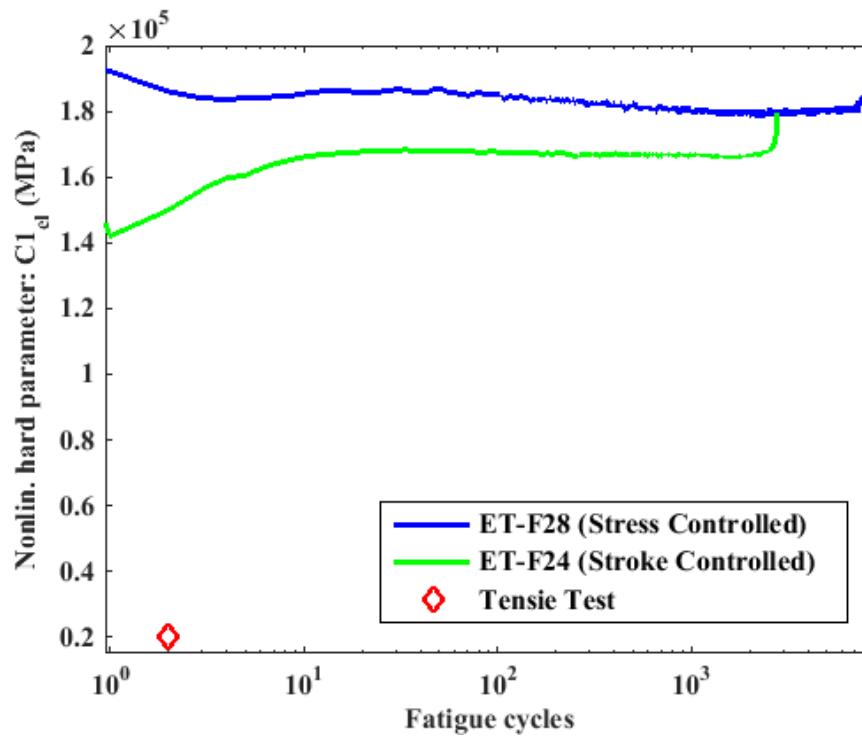


Figure 4.4 Cycle-by-cycle nonlinear kinematic hardening parameter $C1$ estimated from constant-amplitude fatigue tests. Corresponding parameter estimated from tensile test is also shown.

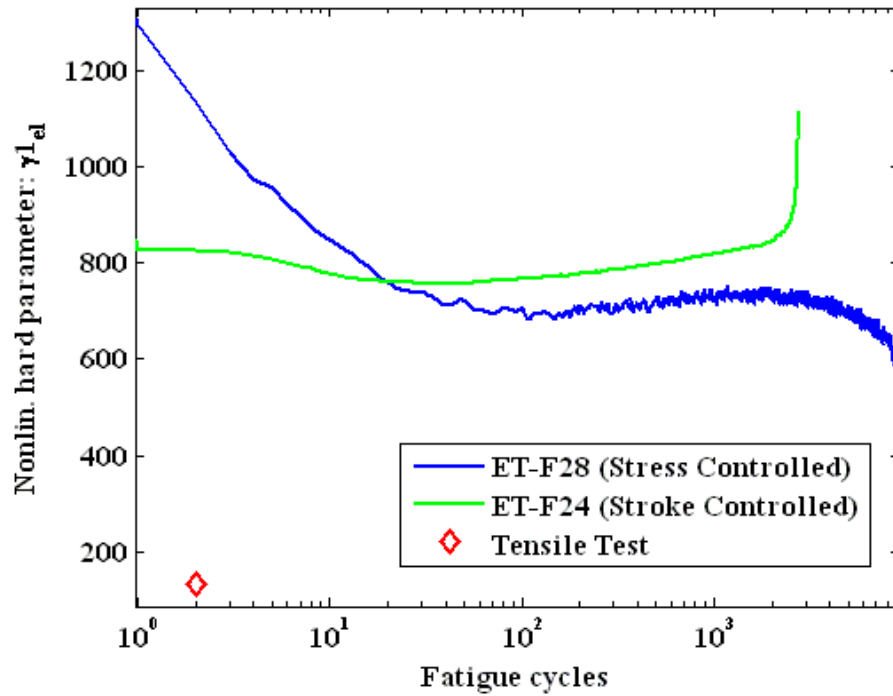


Figure 4.5 Cycle-by-cycle nonlinear kinematic hardening parameter γ_1 estimated from constant-amplitude fatigue tests. Corresponding parameter estimated from tensile test is also shown.

4.2 Parameters Estimated from Variable-Amplitude Fatigue Tests

To capture the independency of the material model and associated parameters on the loading amplitude, we conducted stress-controlled, variable-amplitude fatigue tests under the in-air (ET-F31) and PWR environment (EN-F32) condition at 300°C. The resulting fatigue test data were presented in Section 3. As block loading was applied during these tests, block average (i.e., block-by-block) parameters were estimated. In addition, cycle-by-cycle parameters were also estimated. In this section, we discuss first the cycle-by-cycle parameter results, then the block-by-block parameter results. Both the cases the variable-amplitude fatigue tests data were used. Note that the cycle-by-cycle parameter estimation technique is based on our previously developed technique for time-dependent parameter estimation [26-28]. In this report, however, we are proposing an improved technique for block-by-block parameter estimation (see Section 2 for theoretical background) to obtain parameters that would help to calculate an average for the different-amplitude fatigue cycles within a loading block. We assume that the block-by-block parameters can capture not only the effect of the time/cycle dependence, but also the loading amplitude effect. These improved parameter estimation results will help generate more accurate mechanistic modeling of reactor components under realistic random temperature and pressure transients. Nonetheless, results for both cycle-by-cycle and block-by-block parameters are presented below for comparison.

4.2.1 Cycle-by-Cycle Parameters Estimated from Variable-Amplitude Fatigue Tests

The cyclic stress-strain curves for the variable-amplitude test with 508 LAS base metal were first converted into equivalent monotonic upward and downward stress-strain curves, as we had done above for the constant-amplitude fatigue tests (e.g., ET-F28 and ET-F24). The cycle-dependent-amplitude-dependent (i.e., cycle-by-cycle) parameters such as elastic modulus, elastic limit stress (i.e., yield limit), and nonlinear kinematic hardening parameters ($C1$ and $\gamma1$) were then estimated from the equivalent monotonic curves. The resulting cycle-by-cycle parameters obtained from the ET-F31 and EN-F32 test data are shown in Figures 4.6 to 4.9. Figure 4.6 shows the estimated time/cycle variation of the elastic modulus for both in-air (ET-F31) and PWR water (EN-F32) conditions. Figures 4.7 to 4.9 show the corresponding time/cycle variation of the elastic limit stress and kinematic hardening parameters $C1$ and $\gamma1$.

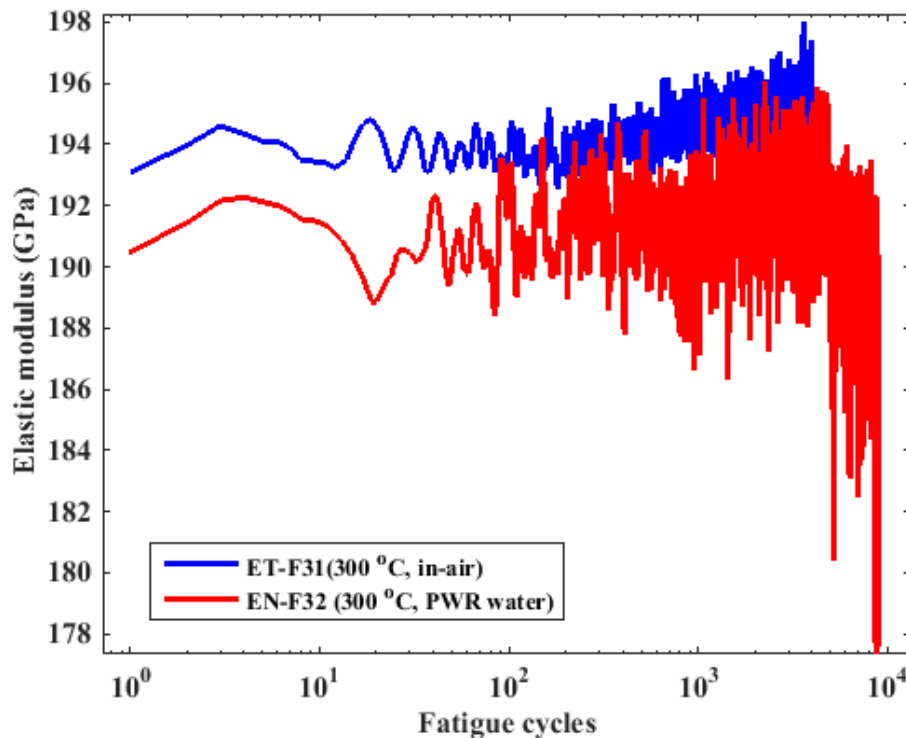


Figure 4.6 Cycle-by-cycle elastic modulus estimated from variable-amplitude fatigue tests.

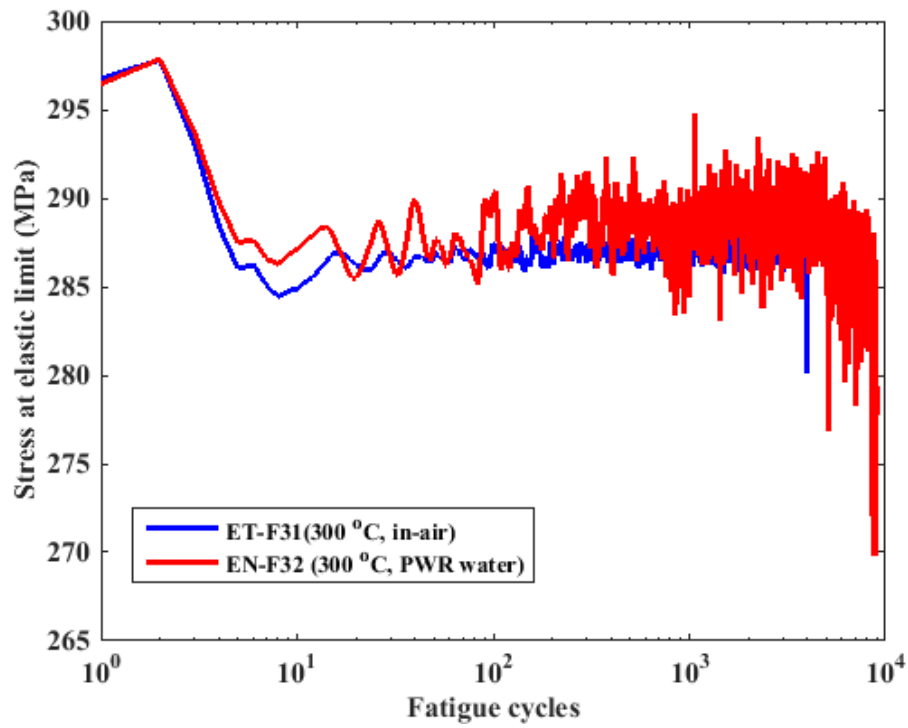


Figure 4.7 Cycle-by-cycle elastic limit stress estimated from variable-amplitude fatigue tests.

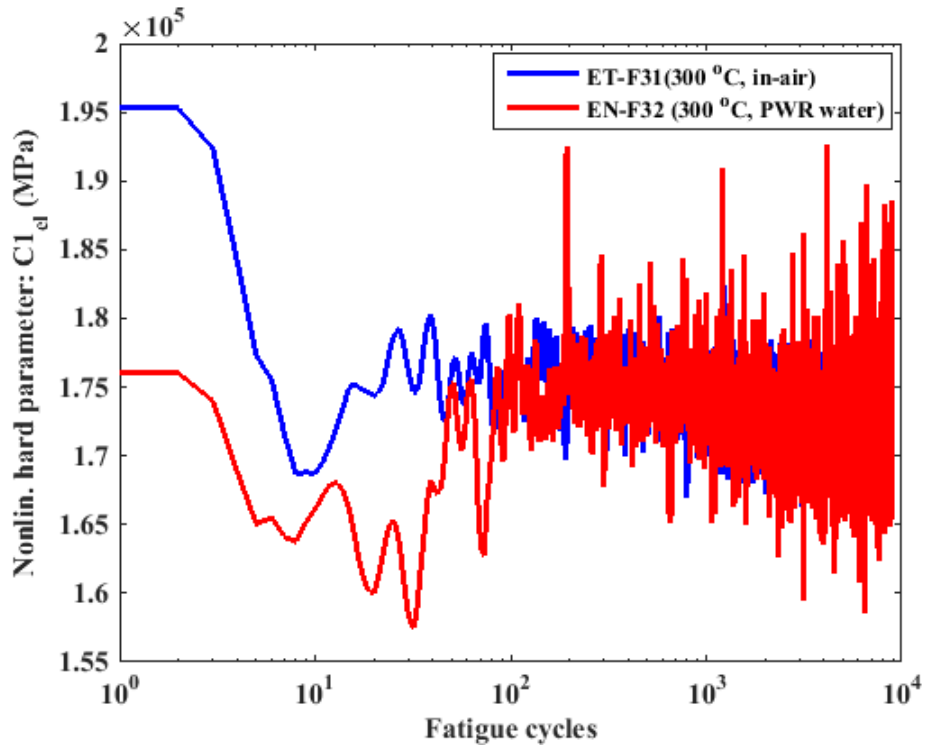


Figure 4.8 Cycle-by-cycle nonlinear kinematic hardening parameter $C1$ estimated from variable-amplitude fatigue tests.

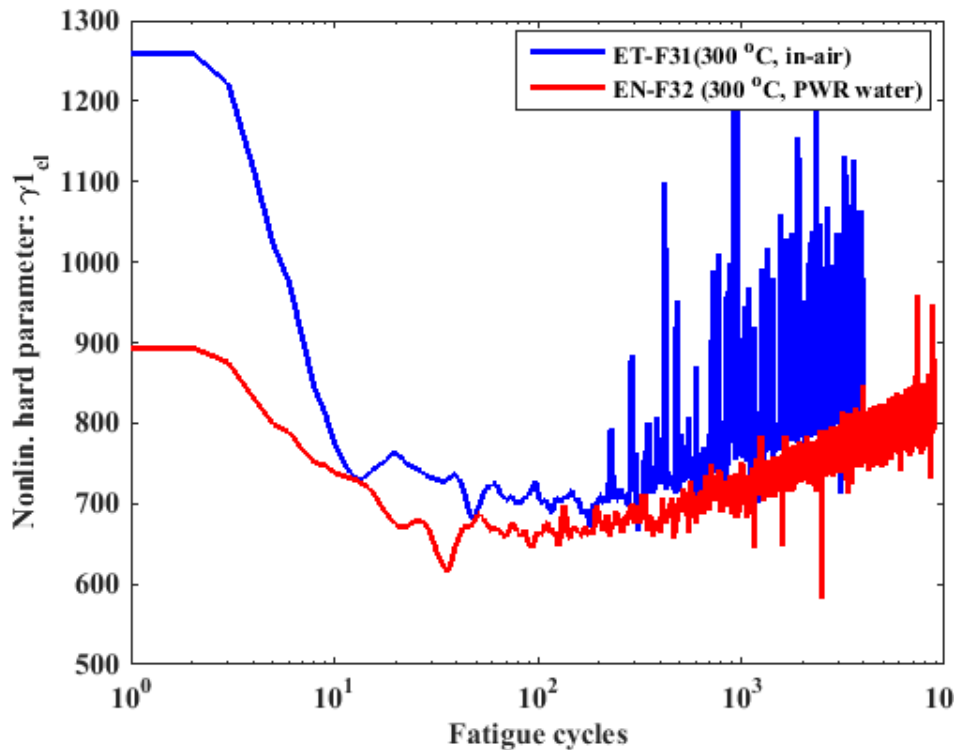


Figure 4.9 Cycle-by-cycle nonlinear kinematic hardening parameter $\gamma_{1_{el}}$ estimated from variable-amplitude fatigue tests.

4.2.2 Block-by-Block Parameters Estimated from Variable-Amplitude Fatigue Tests Using Method 1

According to method 1, as discussed in Section 2, average equivalent monotonic stress-strain curves were estimated by joining the peak locations (for tensile portion) and trough locations (for compressive portion) of individual cyclic stress-strain curves within a loading block. Although these stress-strain curves may not capture the shape of all the amplitude-dependent stress-strain curves (within a block), they can be used as approximate stress-strain curves to capture the amplitude dependency of the model parameters. Figures 4.10 and 4.11 show the resulting stress-strain graphs for 508 base metal under in-air (ET-F31) and PWR water (EN-F32) conditions. Magnified versions of the figures are also shown to demonstrate the variation in the behavior of the material over the entire fatigue life. These graphs were used to estimate time-dependent-amplitude-independent (i.e. block-by-block) parameters. The estimated parameters for 508 LAS base metal alloy under in-air and PWR conditions (both at 300°C) are plotted in Figures 4.12 to 4.15. Figure 4.12 shows the estimated elastic modulus for the in-air (ET-F31 test) and PWR water (EN-F32) conditions. Figures 4.13 to 4.15 show the corresponding results for the elastic limit stress and kinematic hardening parameters C_1 and γ_1 .

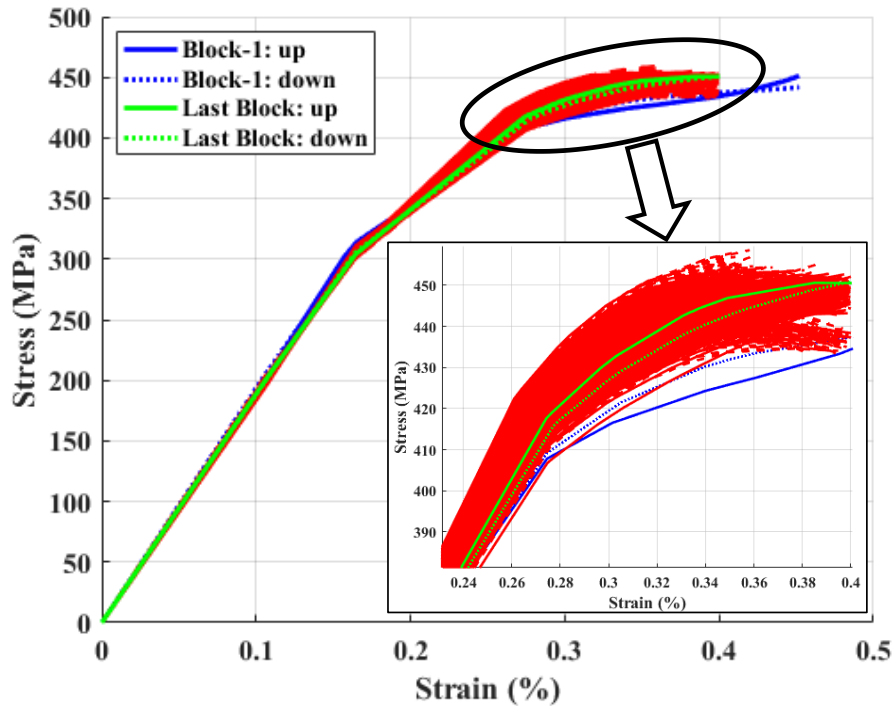


Figure 4.10 Block average equivalent monotonic strain-stress graphs (estimated from ET-F31 test data) for 508 LAS base metal alloy fatigued tested in air at 300°C.

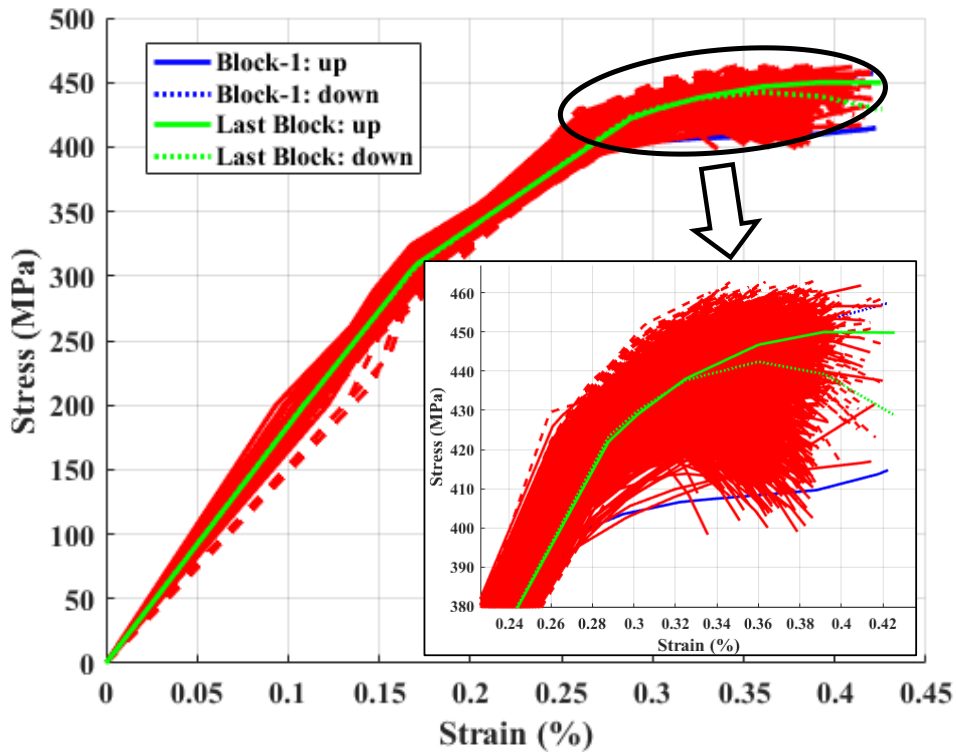


Figure 4.11 Block average equivalent monotonic strain-stress graphs (estimated from EN-F32 test data) for 508 LAS base metal alloy fatigued tested in PWR environment at 300°C.

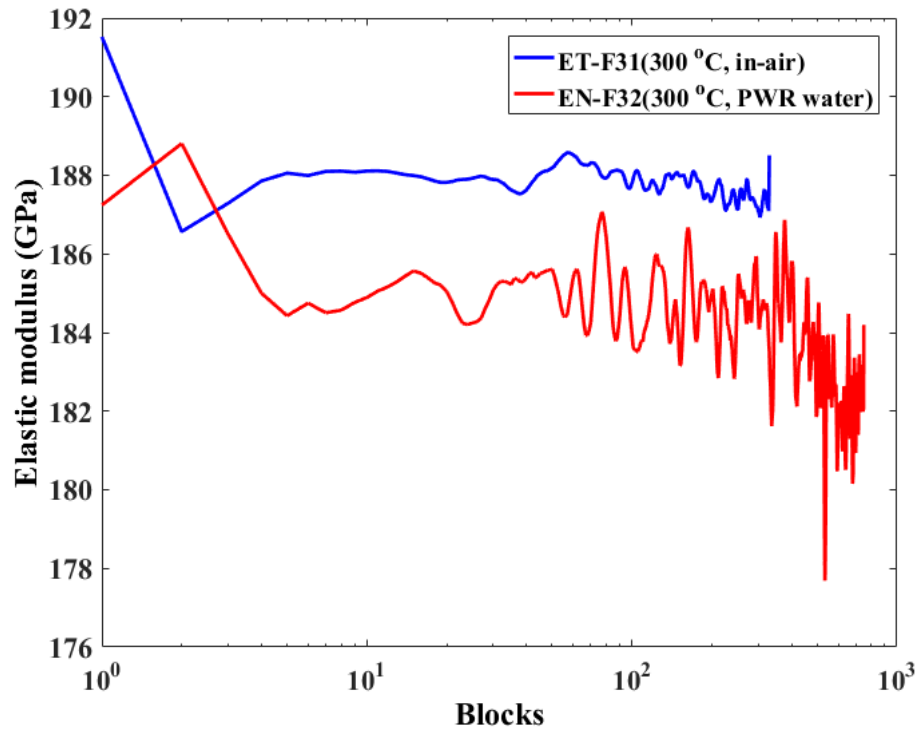


Figure 4.12 Block-by-block elastic modulus estimated (using method 1) from variable-amplitude fatigue tests.

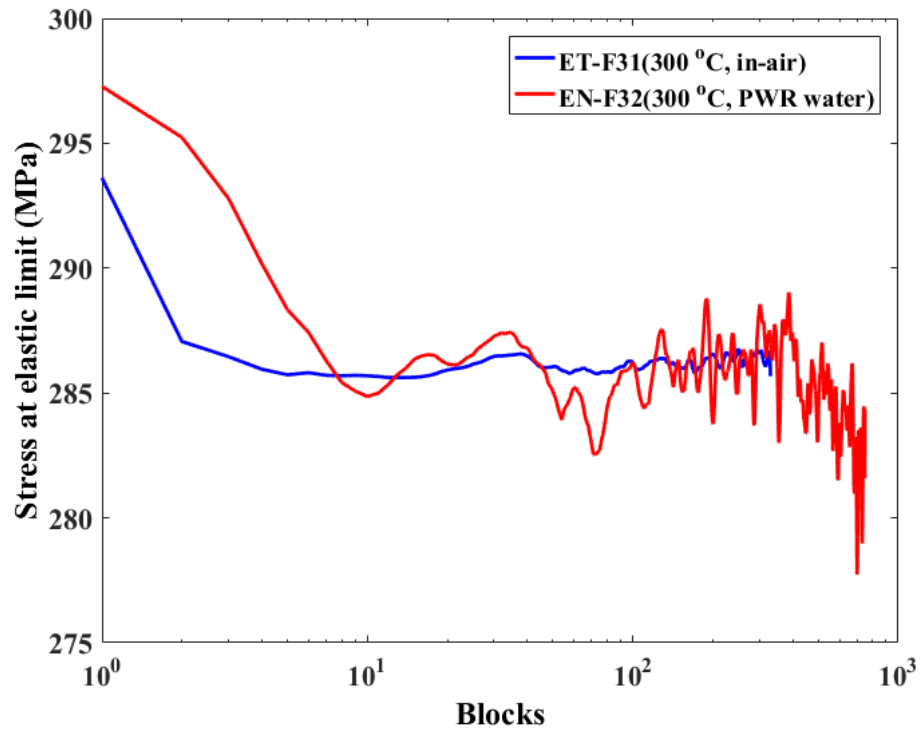


Figure 4.13 Block-by-block elastic limit stress estimated (using method 1) from variable-amplitude fatigue tests.

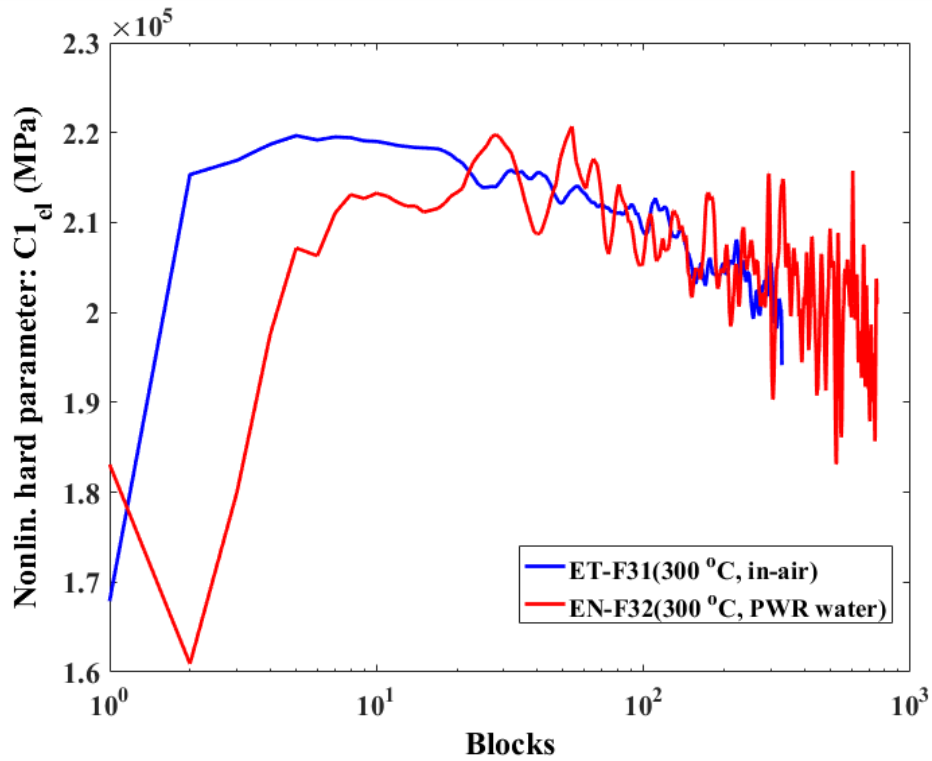


Figure 4.14 Block-by-block nonlinear kinematic hardening parameter $C1$ estimated (using method 1) from variable-amplitude fatigue tests.

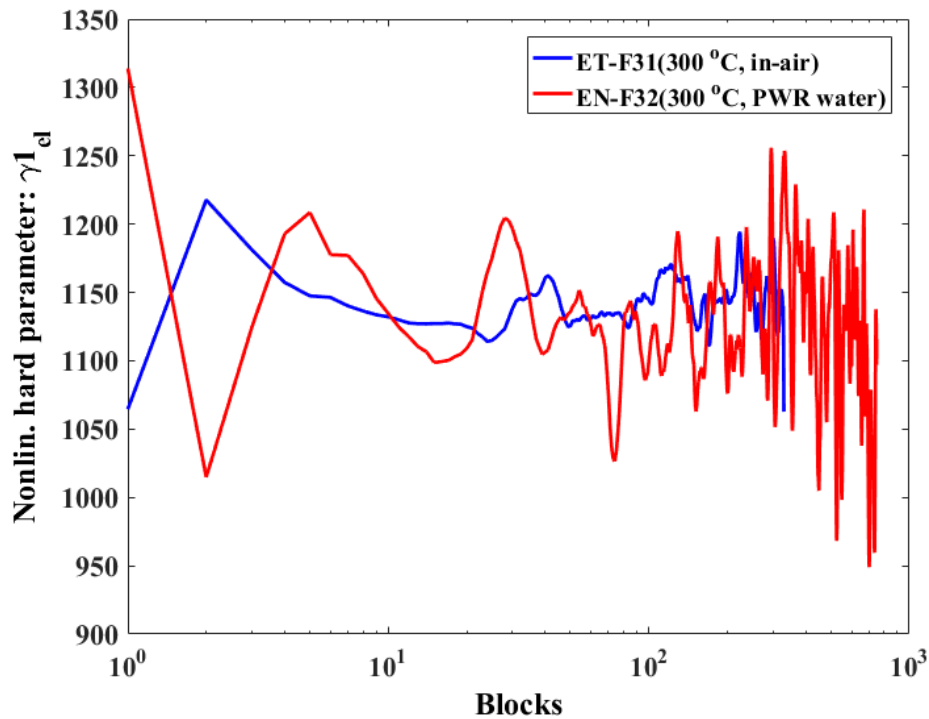


Figure 4.15 Block-by-block nonlinear kinematic hardening parameter $\gamma1$ estimated (using method 1) from variable-amplitude fatigue tests.

4.2.3 Block-by-Block Parameters Estimated from Variable-Amplitude Fatigue Tests Using Method 2

Compared to method 1, in which just the peak and trough locations of cyclic stress-strain curves (in a block) were used, in method 2 the entire stress-strain data (beyond the yield limit) of all the cycles (in a block) were used to estimate the corresponding average parameters. As stated previously, we believe this method will help capture not only the amplitude dependency of the model but also the shape/path of the stress-strain curves. The procedure for estimating the model parameters using method 2 is discussed in Section 2. An example comparison between experimental and predicted true back stress as a function of true plastic strain for a particular block (comprising all 12 cycles within that block) is shown in Figure 4.16. The estimated block-by-block parameters using ET-F31 (in-air, 300°C) and EN-F32 (PWR water, 300°C) tests data are plotted in Figures 4.17 to 4.20. Figure 4.16 shows the block variation of estimated elastic modulus for both in-air (ET-F31 test) and PWR water (EN-F31) conditions. Figures 4.17 to 4.20 show the corresponding block variation of elastic limit stress and kinematic hardening parameters C1 and γ_1 .

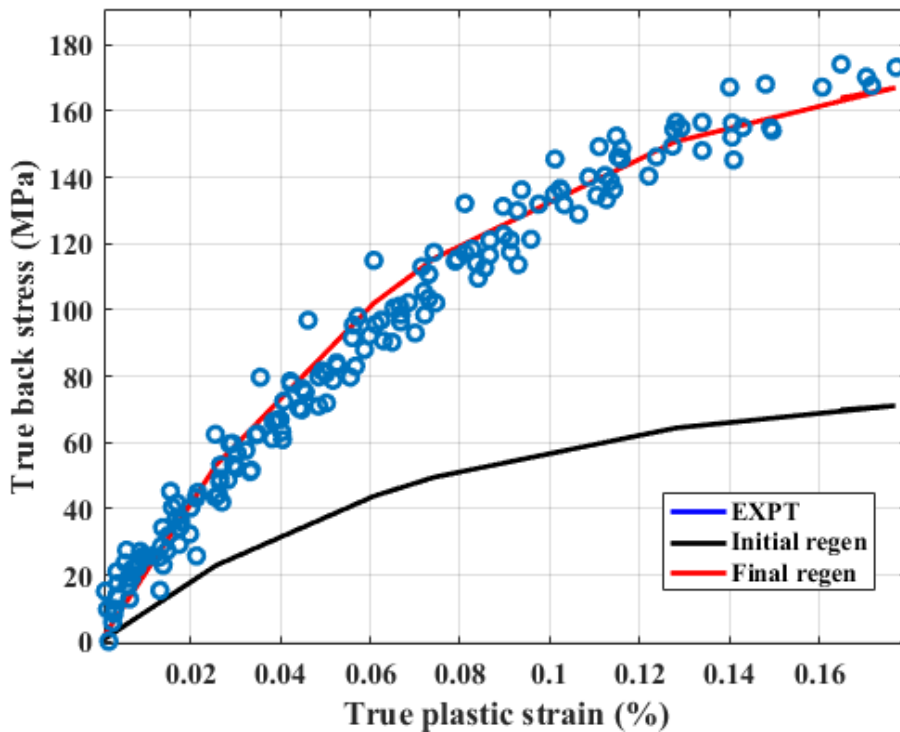


Figure 4.16 Example comparison of experimental true back stress (as a function of true plastic strain) with that predicted by using average hardening parameters (method 2) pertaining to that block.

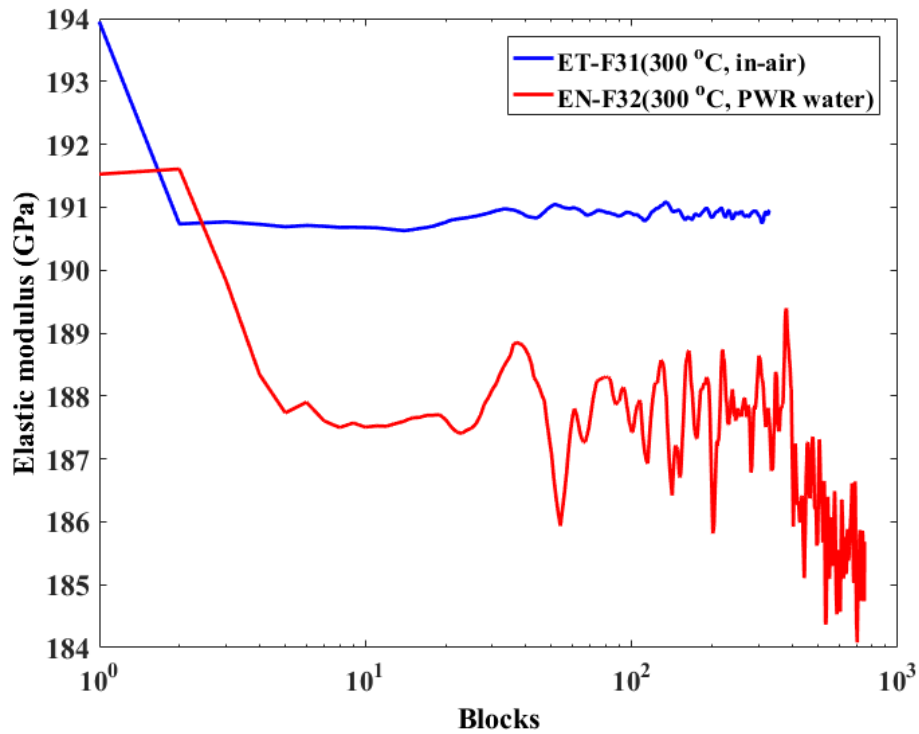


Figure 4.17 Block-by-block elastic modulus estimated (using method 2) from variable-amplitude fatigue tests.

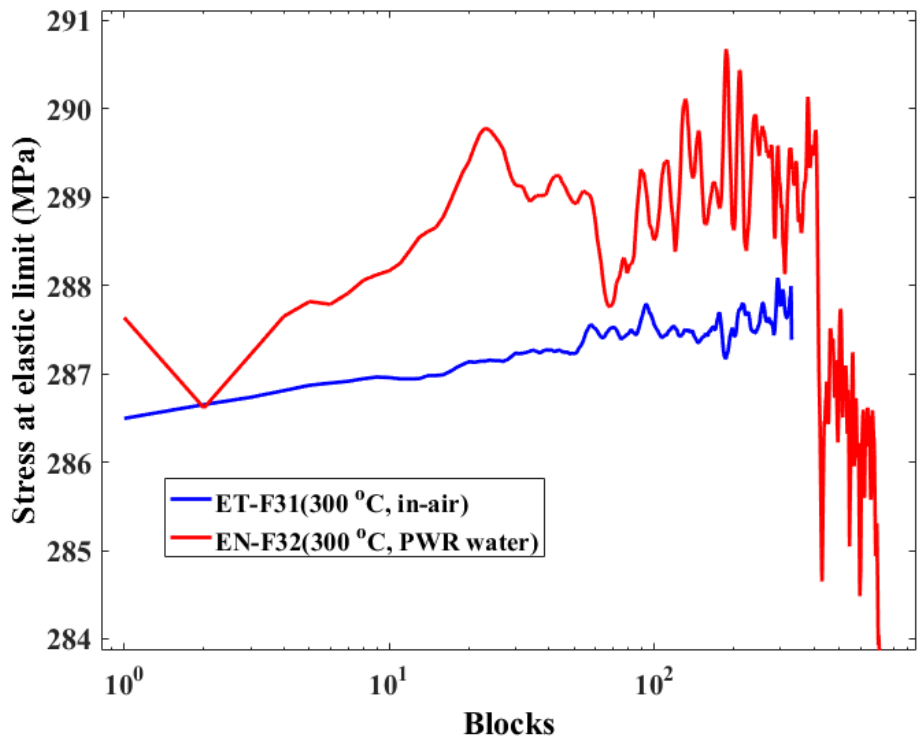


Figure 4.18 Block-by-block elastic limit stress estimated (using method 2) from variable-amplitude fatigue tests.

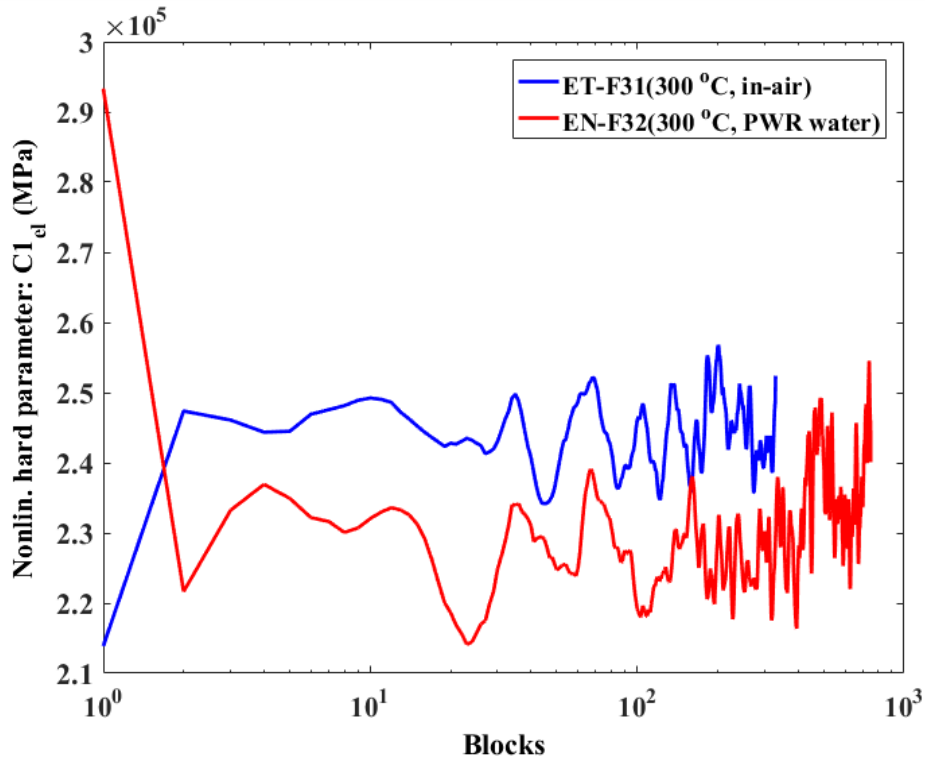


Figure 4.19 Block-by-block nonlinear kinematic hardening parameter $C1$ estimated (using method 2) from variable-amplitude fatigue tests.

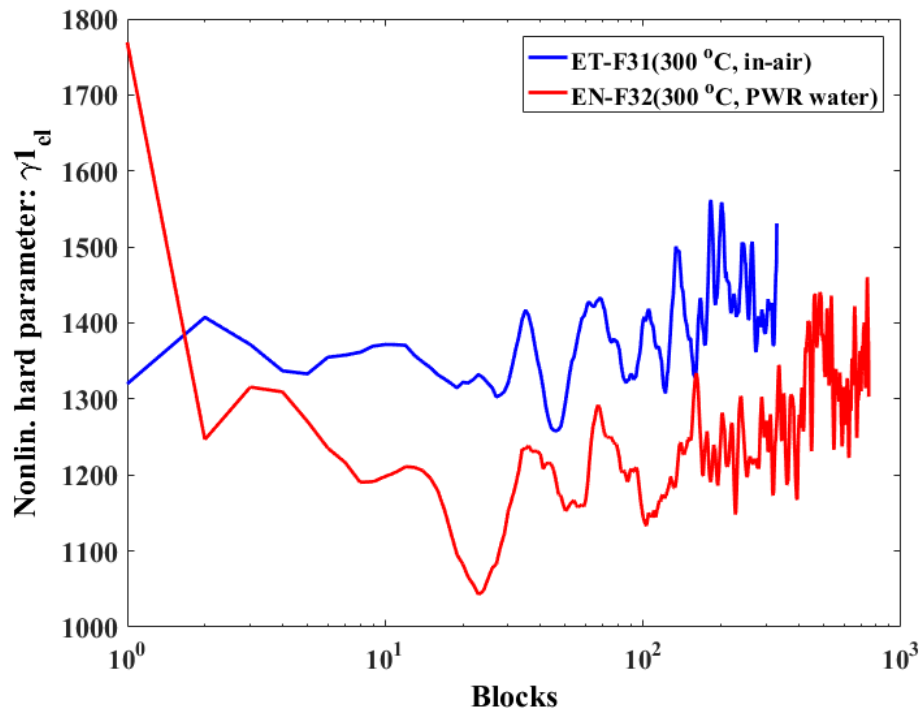


Figure 4.20 Block-by-block nonlinear kinematic hardening parameter $\gamma1$ estimated (using method 2) from variable-amplitude fatigue tests.

5 Results from Analytical Modeling

Section 2 describes a time-dependent cyclic plasticity model and related parameter estimation technique, and Section 4 presents the estimated time-dependent parameters. In this section, the time-dependent cyclic plasticity model was verified by analytically modeling various fatigue test cases using the estimated time-dependent parameters. The fatigue test specimens were also modeled with time-independent (i.e., fixed) parameters, such as those associated with tensile tests and half-life fatigue tests. The results predicted from the fixed parameters were then compared with those predicted from time-dependent parameters. This comparison is essential to determine whether the estimated parameters can predict the nonlinear ratcheting (or hardening/softening) behavior of materials under cyclic loading. Most important, in addition to providing the analytical model verification for the constant-amplitude fatigue tests, the behavior of 508 LAS base metal under variable-amplitude fatigue tests was modeled by using estimated block-by-block (i.e., time-dependent-amplitude-independent) parameters. Analytical modeling of the variable-amplitude specimens was carried out to check whether those estimated parameters can reconstruct the stress-strain states for that particular test condition. As presented in Section 4, methods 1 and 2 were employed to estimate the block-by-block, time-dependent, amplitude-independent parameters.

5.1 Constant-Amplitude Fatigue Tests

Figures 5.1 and 5.2 show the predicted versus experimental hysteresis curves for the first 20 cycles of a constant-amplitude fatigue test (ET-F28) using fixed (or time-independent) parameters estimated from a tensile test (ET-T08) and the corresponding fatigue test (ET-F28) data at half-life. The curves indicate that the analytical model based on constant parameters does not predict the material behavior accurately. Figure 5.1 shows that the tensile-test-based properties are not able to capture the shape of the fatigue test data. Figure 5.2 shows that, despite using material properties estimated from same fatigue test (ET-F28) data, the fixed half-life parameters are not able to capture the stress-strain state accurately. In particular, there is a large discrepancy between the predicted and experimental peak amplitudes. The peak amplitude for stress differs by more than 50 MPa compared with that obtained from the model based on the half-life parameter. In contrast, the material behavior is well predicted when the time-dependent parameters are used, as evident from Figure 5.3. This finding verifies the importance of using time-dependent parameters to model the safety-critical reactor components for fatigue life evaluation.

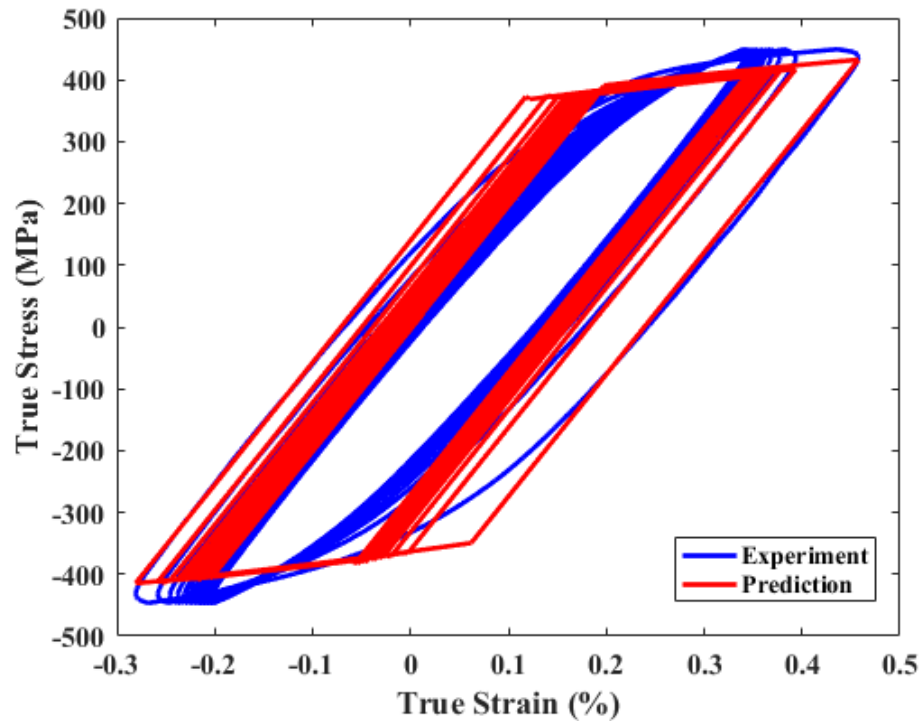


Figure 5.1 Predicted (using time-independent parameters estimated from tensile test ET-T08) versus experimental hysteresis curves for first 20 cycles of ET-F28 test.

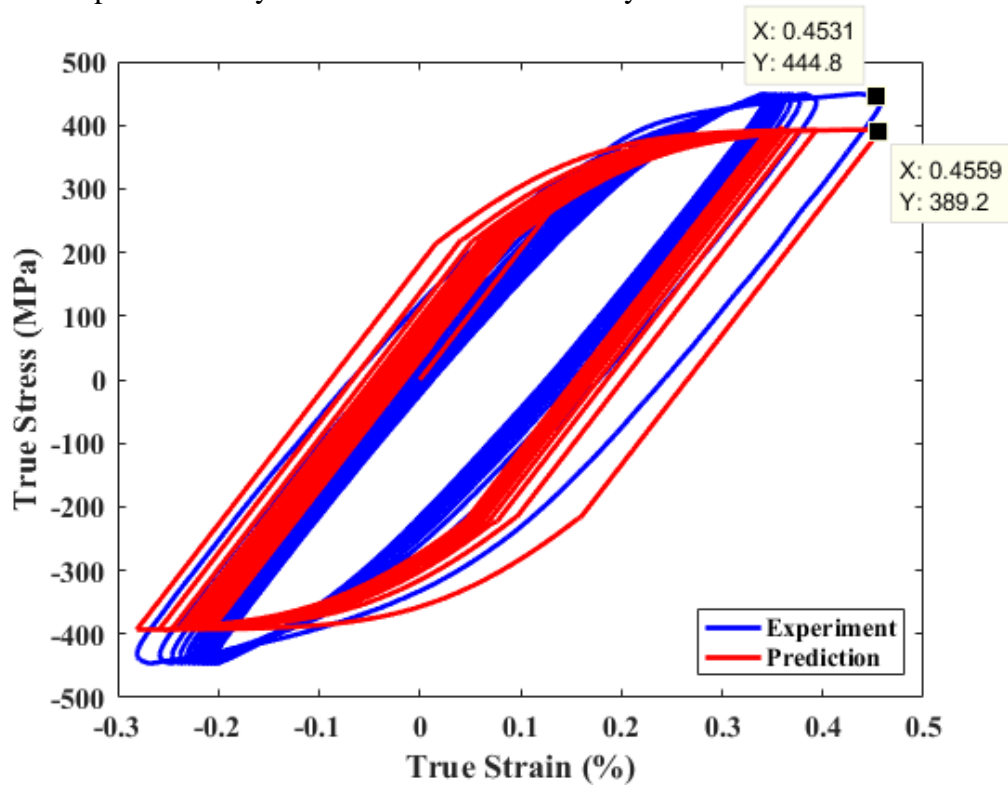


Figure 5.2 Predicted (using time-independent parameters estimated from ET-F28 fatigue test data at half-life) versus experimental hysteresis curves for first 20 cycles of ET-F28 test.

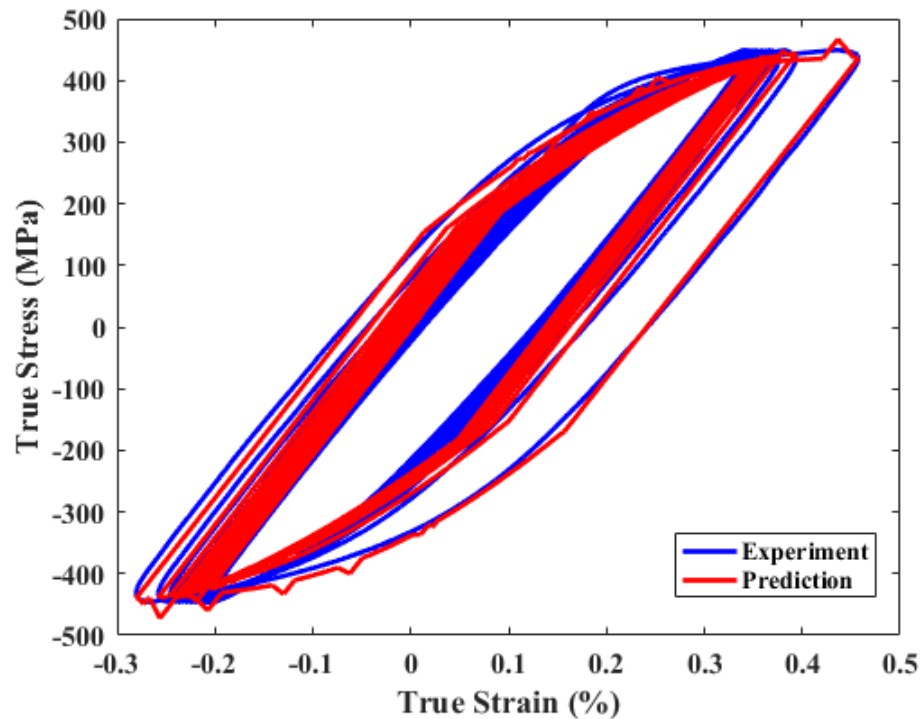


Figure 5.3 Predicted (using time-dependent, cycle-by-cycle parameters estimated from ET-F28) versus experimental hysteresis curves for first 20 cycles of ET-F28 test.

5.2 Variable-Amplitude Fatigue Tests

5.2.1 Results Using Time-Independent and Time-Dependent (Cycle-by-cycle) Parameters

To verify the cyclic plasticity model, in the case of variable-amplitude fatigue loading, the ET-F31 specimen was modeled by using both time-independent (or fixed) and time-dependent (cycle-by-cycle) parameters. Figures 5.4-5.6 show the predicted versus experimental hysteresis curves for the first block (with 12 variable-amplitude fatigue cycles) of the ET-F31 fatigue test. Figure 5.4 shows the predicted hysteresis curves using fixed tensile test (ET-T08) data, whereas Figure 5.5 shows the predicted hysteresis curves using a fixed set of parameters obtained from half-life data for the ET-F28 fatigue test. In contrast, Figure 5.6 shows the predictions using time-dependent (cycle-by-cycle) parameters estimated from each cycle data of the first block in the ET-F31 fatigue test. It is evident from Figures 5.4 to 5.6 that the material behavior under variable-amplitude fatigue loading can be well predicted with time-dependent parameters. However, the hysteresis curve shown in Figure 5.6 was predicted with the amplitude-dependent, cycle-by-cycle parameters. Although, ideally, amplitude-dependent parameters can be considered for this test case, it may not be feasible to consider amplitude-dependent parameters for real-life loading transients consisting of hundreds to thousands of loading peaks. This condition necessitates the use of an amplitude-independent model for determining the stress-strain state under variable loading. The associated verification results are discussed in the following subsection.

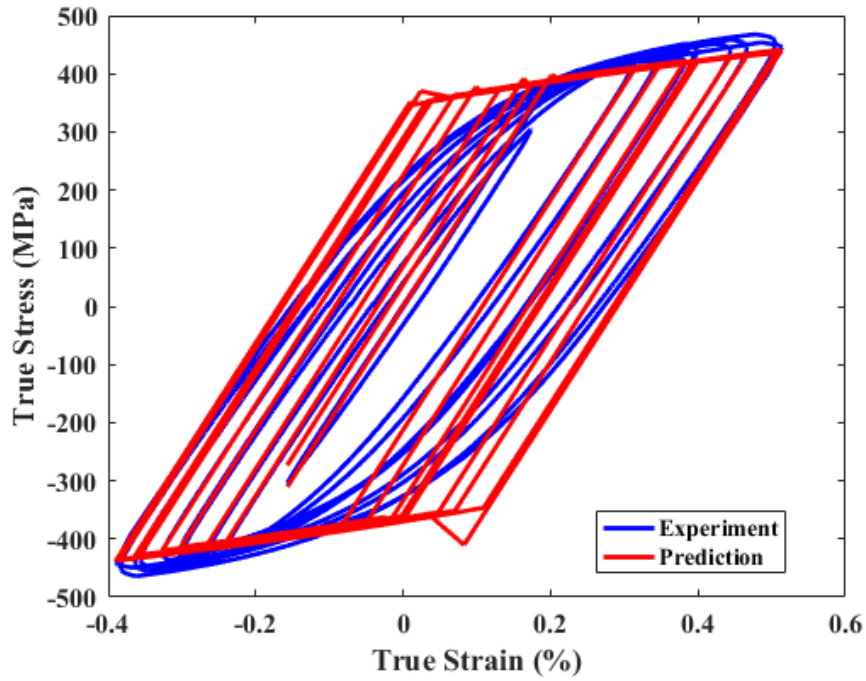


Figure 5.4 Predicted (using time-independent parameters from ET-T08) versus experimental hysteresis curves for first block (with 12 variable-amplitude cycles) of ET-F31 test.

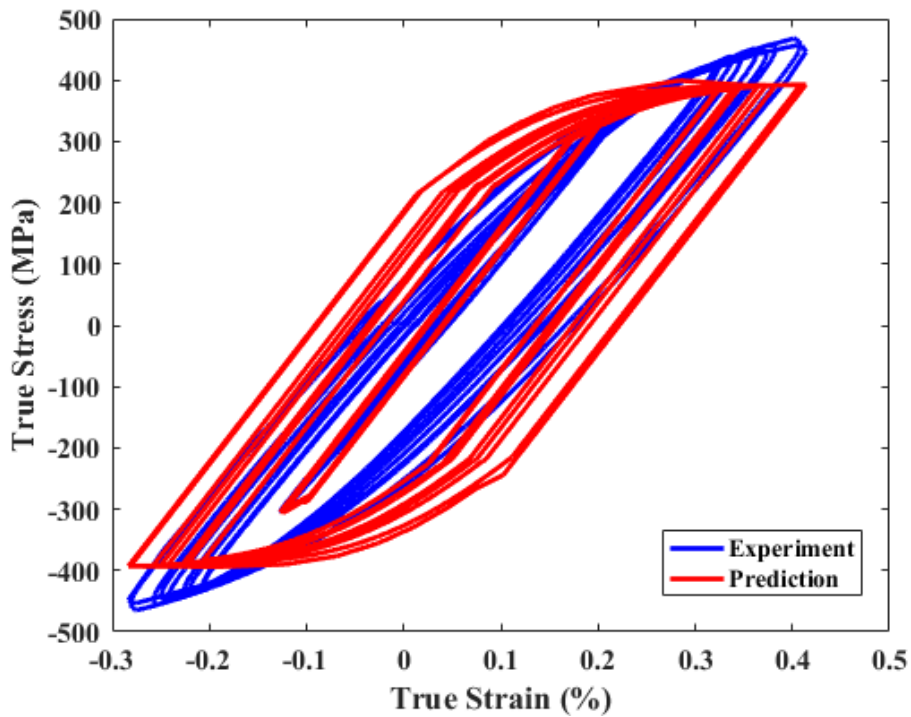


Figure 5.5 Predicted (using time-independent parameters from half-life fatigue data of ET-F28) versus experimental hysteresis curves for first block (with 12 variable-amplitude cycles) of ET-F31 test.

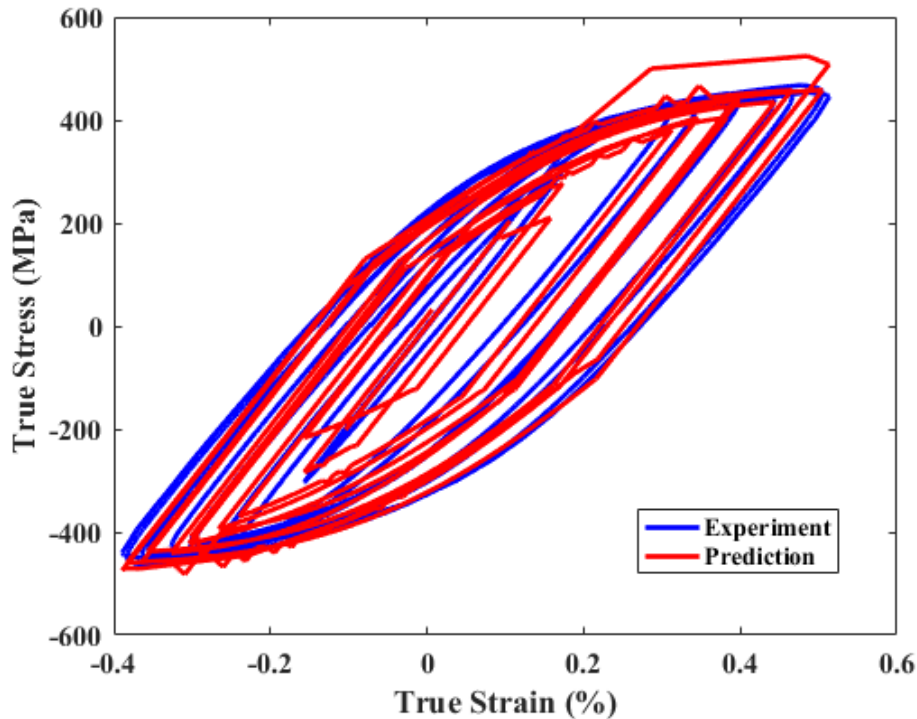


Figure 5.6 Predicted (using cycle-by-cycle, amplitude-dependent parameters estimated from first block data of ET-F31 fatigue test) versus experimental hysteresis curves for first block (with 12 variable-amplitude cycles) of ET-F31 test.

5.2.2 Results Using Time-Dependent-Amplitude-Independent (Block-by-Block) Parameters

As discussed in Section 4 (see also comparison between ET-F24 and ET-F28 data, presented in Figures 4.2 to 4.5), the parameters, such as elastic modulus, elastic limit stress, and material kinematic hardening ($C1$ and $\gamma1$), vary not only with time but also loading amplitude. To capture the amplitude independency in estimated parameters, two methods were introduced in Section 2. The time-dependent-amplitude-independent (or block-by-block) parameters for 508 LAS base metal under different environmental conditions (in-air and PWR environment) were estimated from variable-amplitude fatigue tests (ET-F31 and EN-F32) and are presented in Section 4. It was assumed that that the block-by-block parameters using method 2 should predict the parameters better than those estimated using method 1, since the back stress versus plastic stain data within a variable-amplitude block loading (with multiple-variable loading cycles) are considered in method 2, in contrast to only the corresponding peak and trough data in method 1.

The results for the ET-F31 fatigue test specimen using block-by-block parameters estimated by methods 1 and 2 are shown in Figures 5.7 and 5.8, respectively. It is evident from these two figures that the estimated parameters using method 2 agree better with measured values than those estimated using method 1. Figure 5.9 and 5.10 show the corresponding 20th block predicted versus experimental hysteresis curves of ET-F31 using methods 1 and 2, respectively. Furthermore, we also used the estimated parameters under PWR water conditions to predict the hysteresis curves for the PWR water fatigue test EN-F32. Figures 5.11 and 5.12 show the predicted versus experimental hysteresis curves for the EN-F32 test using

method 2 and the 1st and 20th blocks, respectively. As seen from the above results (Figures 5.7 to 5.12), the model predictions for in-air (ET-F31) are better compared to PWR water (EN-F32) test. This is possibly due to the EN-F32 strain history which was not directly measured rather estimated from stroke measurements using a stroke-strain mapping function. In addition, the discrepancy could be due to noise in sensor measurements associated with water flow in PWR test loop. Nonetheless, for both the variable-amplitude test cases, there is a better capturing of stress-strain state due to the use of block-by-block parameters.

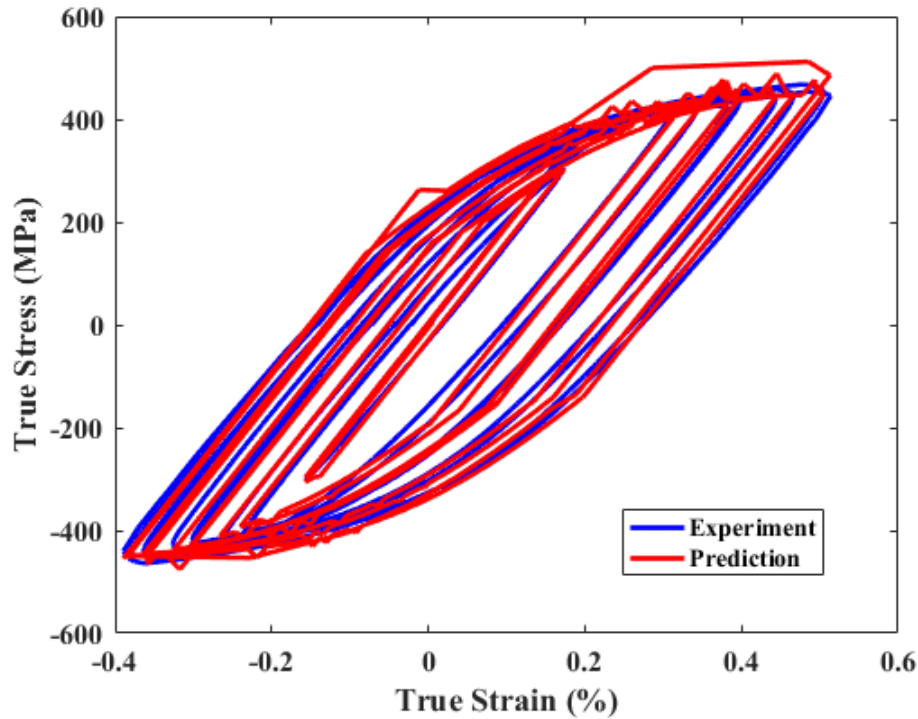


Figure 5.7 Predicted (using method 1 block-by-block parameters estimated from ET-F31 data) versus experimental hysteresis curves for 12 variable-amplitude fatigue cycles within the 1st block of ET-F31 test.

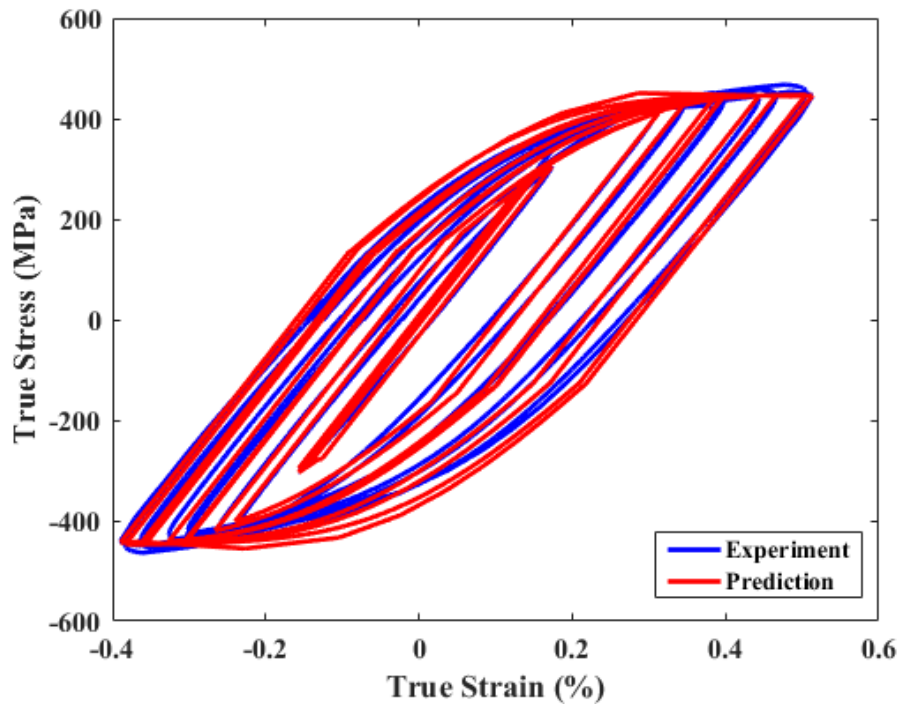


Figure 5.8 Predicted (using method 2 block-by-block parameters estimated from ET-F31 data) versus experimental hysteresis curves for 12 variable-amplitude fatigue cycles within the 1st block of ET-F31 test.

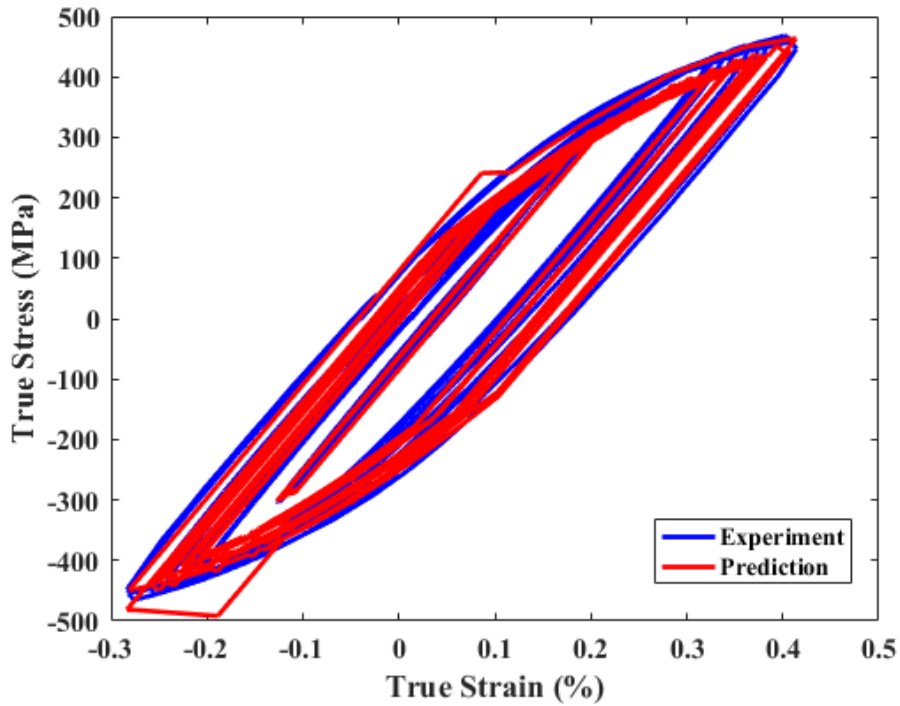


Figure 5.9 Predicted (using method 1 block-by-block parameters estimated from ET-F31 data) versus experimental hysteresis curves for 12 variable-amplitude fatigue cycles within the 20th block of ET-F31 test.

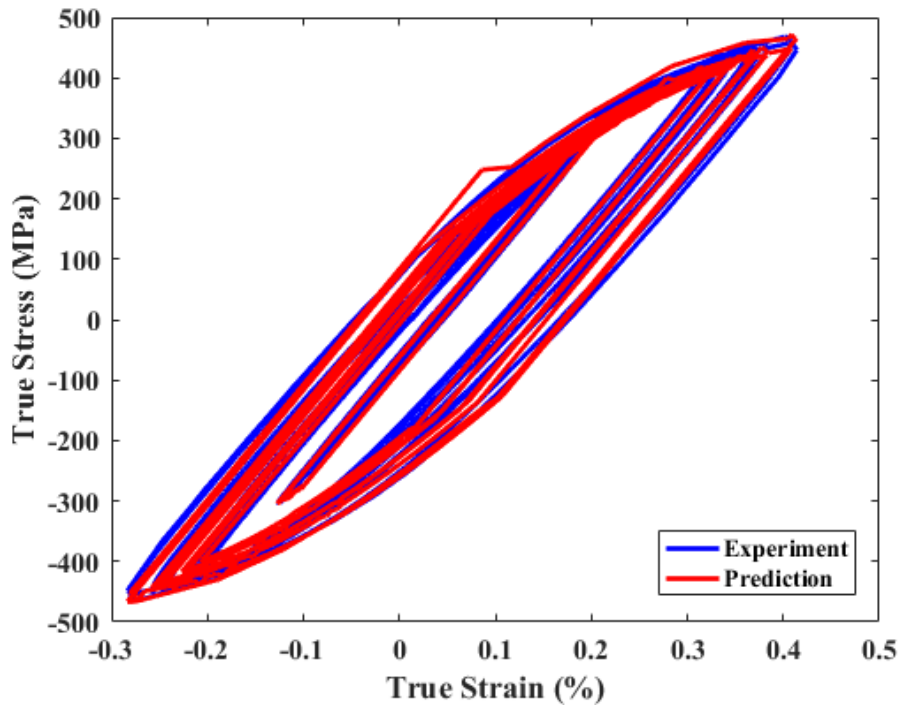


Figure 5.10 Predicted (using method 2 block-by-block parameters estimated from ET-F31 data) versus experimental hysteresis curves for 12 variable-amplitude fatigue cycles within the 20th block of ET-F31 test.

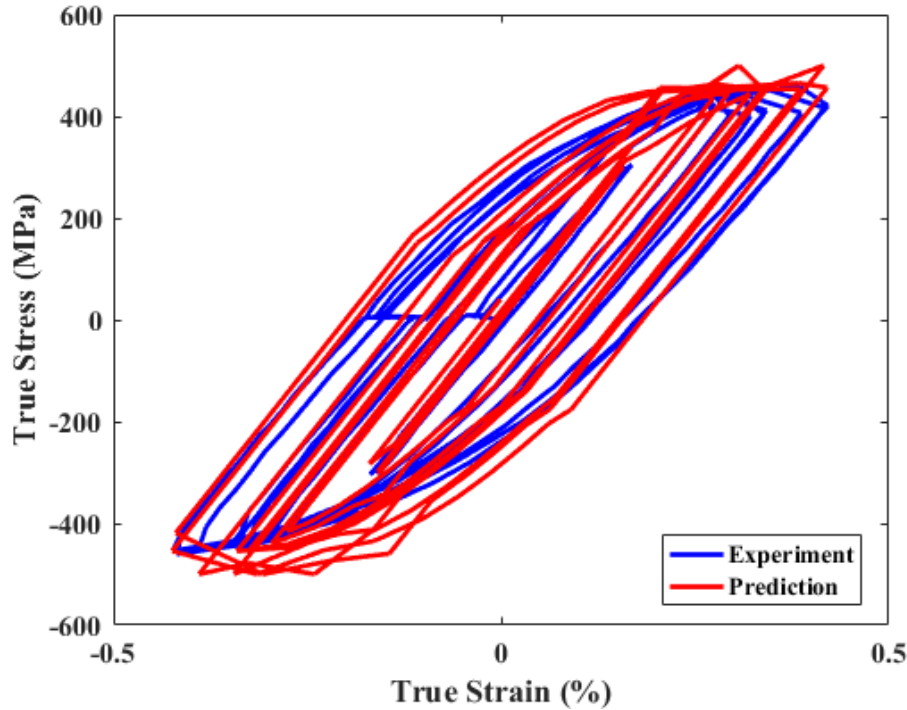


Figure 5.11 Predicted (using method 2 block-by-block parameters estimated from EN-F32 data) versus experimental hysteresis curves for 12 variable-amplitude fatigue cycles within the 1st block of ET-F32 test.

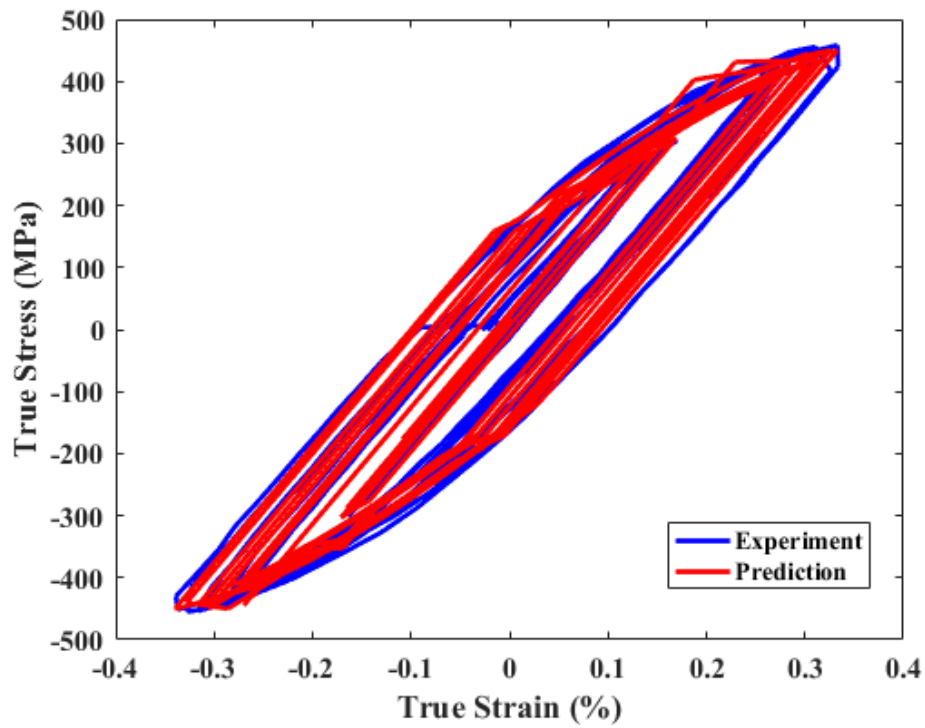


Figure 5.12 Predicted (using method 2 block-by-block parameters estimated from EN-F32 data) versus experimental hysteresis curves for 12 variable-amplitude fatigue cycles within the 20th block of ET-F32 test.

6 Summary and Future Study

In this report, we presented fatigue test data of 508 LAS base metal alloy under the stress control mode with different amplitude conditions (constant, variable, and grid-load-following random amplitude) and in different environments (in-air and PWR water conditions). Based on our previously proposed cyclic plasticity model, the time-dependent (i.e., cycle-by-cycle) material properties, such as elastic modulus, elastic limit stress, and kinematic hardening parameters ($C1$ and $\gamma1$), were estimated from the stress-controlled, constant-amplitude fatigue test data. The comparison of the stress-controlled fatigue test results with previously reported stroke-controlled fatigue test results indicated that the estimated material parameters are amplitude dependent. Thus, the quantification of the amplitude dependencies for the model parameters is important for accurate modeling of the stress-strain state of the reactor components.

To capture the amplitude dependency of the material behavior, two novel parameter estimation techniques are proposed, both of which are based on variable-amplitude fatigue test data. The first method uses the peak and trough locations of the hysteresis curves within a variable-amplitude loading block, while the second uses all the stress-strain data within that variable-amplitude loading block. It is our assumption that the second method is better compared to the first and would help to capture not only the amplitude dependency of the material model, as is the case of method 1, but also the shape/path of the stress-strain curves. In addition to the constant-amplitude fatigue test, variable-amplitude fatigue tests were conducted under in-air and PWR water conditions. These data were used for estimating the time-dependent-amplitude-independent (block-by-block) parameters using the above two methods.

The accuracy of the estimated parameters was verified by analytically (or mechanistically) modeling the various fatigue test scenarios. The results indicate that the material behavior is better predicted by using time-dependent parameters (obtained through fatigue test data) rather than fixed or time-independent parameters (obtained through tensile test data or half-life data of a fatigue test). However, from the analytical model results, we also found that the time/cycle-dependent parameters based on constant-amplitude test data are not able to predict the stress-strain state of a variable condition fatigue test accurately. At the same time, the analytical model results show that the time-dependent-amplitude-independent parameters are able to capture the stress-strain state under variable-amplitude fatigue loading. Thus, it is important to use time-dependent-amplitude-independent material parameters for more accurate stress analysis of safety-critical reactor components under real-life variable/random loading. Also as expected, the block-by-block parameters estimated by method 2 predicted the material behavior better than those estimated by method 1.

We also conducted grid-load-following random amplitude fatigue tests using the previously reported finite element simulation results. This was done to simulate the 3D stress-strain state of a cracked RPV nozzle using small-specimen laboratory tests. The tests were conducted under both in-air and PWR water conditions. However, the experimental results showed high plastic strain generation during the first loading block and then follow-up elastic shakedown. The high strain generation and subsequent elastic shakedown could be due to a combination of material effects associated with loading amplitude and loading rate. They could also be due to following a pure tensile-tensile loading profile, which didn't allow the material to reverse back some of the plastic strain as it would have recovered in the case of conventional tensile-compression fatigue tests. Due to this high strain generation, the grid-load-following fatigue test results were not considered further for analytical modeling validation. This is because the

analytical models were developed based on material parameters, which are a function of much smaller strain amplitudes. However, the preliminary grid-load-following results show the complexity in conducting stress-controlled fatigue tests, particularly under prototypical (in this case, tensile-tensile) loading conditions. The grid-load-following fatigue tests will be repeated in the future to ascertain the exact reason for initial strain hardening and subsequent elastic shakedown. In addition, the parameter estimation techniques based on variable-amplitude tests will be extended to 316 SS base and 508 LAS-316 SS weld metals.

7 References

1. Faidy, C., and Wazylyk, A., "Nuclear Fatigue Analysis Codified Design Rules Comparison of Cyclic Plasticity Effects," Proceedings of the ASME Pressure Vessels and Piping Conference, Paper No. PVP2015-45198 (2015).
2. Chopra, O. K., and Shack, W. J., "Effect of LWR Coolant Environments on the Fatigue Life of Reactor Materials," U.S. Nuclear Regulatory Commission Report No. NUREG/CR-6909 (2007).
3. Chopra, O., and Stevens, G., "Effect of LWR Coolant Environments on the Fatigue Life of Reactor Materials," U.S. Nuclear Regulatory Commission Report No. NUREG/CR-6909, Revision 1 (2014).
4. Japan Nuclear Energy Safety Organization, "Nuclear Power Generation Facilities Environmental Fatigue Evaluation Method for Nuclear Power Plants," Nuclear Energy System Safety Division, Japan Nuclear Energy Safety Organization Report No. JNES-SS-1005 (2011).
5. Métais, T. P., Stevens, G., Blatman, G., Le Roux, J. C., and Tregoning, R. L., in *ASME 2015 Pressure Vessels and Piping Conference* (pp. V01AT01A031-V01AT01A031), Paper no. PVP2015-45146, American Society of Mechanical Engineers (2015).
6. De Baglion, L., Cedat, D., Ould, P., and Chitty, W. J., "Low Cycle Fatigue Behavior in Air and in PWR Water of Type 304L and 316L Austenitic Stainless Steels Manufactured by Hot Isostatic Pressing Process," *ASME 2015 Pressure Vessels and Piping Conference* (pp. V01AT01A034-V01AT01A034), Paper No. PVP2015-45214, American Society of Mechanical Engineers (2015).
7. Wilhelm, P., Steinmann, P., and Rudolph, J., "Fatigue Strain-Life Behavior of Austenitic Stainless Steels in Pressurized Water Reactor Environments," *ASME 2015 Pressure Vessels and Piping Conference* (pp. V01AT01A025-V01AT01A025), Paper no. PVP2015-45011, American Society of Mechanical Engineers (2015).
8. Platts, N., Tice, D., Stairmand, J., Mottershead, K., Zhang, W., Meldrum, J., and McLennan, A., "Effect of Surface Condition on the Fatigue Life of Austenitic Stainless Steels in High Temperature Water Environments," *ASME 2015 Pressure Vessels and Piping Conference* (pp. V01AT01A028-V01AT01A028), Paper no. PVP2015-45029, American Society of Mechanical Engineers (2015).
9. Han, Y., and Wang, K. S., "Effect of Cold Stretching on Fatigue Properties of Type S31603 Austenitic Stainless Steel at High Temperature," *Procedia Engineering*, 130: 1075-1080 (2015).
10. Ranganath, S., and Mehta, H. S., "An Examination of the Role of the Assumed Young's Modulus Value at the High Cycle End of ASME Code Fatigue Curve for Stainless Steels," *ASME 2015 Pressure Vessels and Piping Conference* (pp. V01AT01A038-V01AT01A038), American Society of Mechanical Engineers (2015).
11. Reese, S. H., Seichter, J., Klucke, D., and Karabaki, H. E., "Numerical Evaluation of Environmentally Assisted Fatigue (EAF) in Consideration of Recent Updates of the Formulas and Hold Time Effects," *ASME 2015 Pressure Vessels and Piping Conference* (pp. V01AT01A026-V01AT01A026), Paper no. PVP2015-45020, American Society of Mechanical Engineers (2015).
12. Platts, N., Tice, D. R., and Nicholls, J., "Study of Fatigue Initiation of Austenitic Stainless Steel in a High Temperature Water Environment and in Air Using Blunt Notch Compact Tension Specimens," *ASME 2015 Pressure Vessels and Piping Conference* (pp. V01AT01A042-V01AT01A042), Paper no. PVP2015-45844, American Society of Mechanical Engineers (2015).
13. Solin, J., Reese, S., Karabaki, H. E., and Mayinger, W., "Research on Hold Time Effects in Fatigue of Stainless Steel: Simulation of Normal Operation Between Fatigue Transients," *ASME 2015 Pressure Vessels and Piping Conference* (pp. V01AT01A030-V01AT01A030), Paper no. PVP2015-45098, American Society of Mechanical Engineers (2015).

14. Emslie, J., Watson, C., Gill, C., and Wright, K., "Temperature and Rise Time Inputs to Fatigue Crack Growth Calculations for Austenitic Stainless Steels in a Pressurised Water Reactor Environment," *ASME 2015 Pressure Vessels and Piping Conference* (pp. V01AT01A037-V01AT01A037), Paper no. PVP2015-45587, American Society of Mechanical Engineers (2015).
15. American Society of Mechanical Engineers, *ASME Boiler and Pressure Vessel Code*, Section III, Division 1 - Subsection NB (2013).
16. Nuclear Safety Standards Commission (KTA), "Components of the Reactor Coolant Pressure Boundary of Light Water Reactors," KTA 3201.2 Part 2, Design and Analysis, Salzgitter, Germany (2013).
17. Rudolph, J., Maneschy, J. E., Cisternas, M., Freire, J. L. F., Costa, F. M., Silva, B., and Suanno, R., "Load Data Evaluation, Stress Analysis and Cycle Counting for the Qualified Thermal Fatigue Assessment of a NPP Component," *ASME 2015 Pressure Vessels and Piping Conference* (pp. V01AT01A055-V01AT01A055), Paper no. PVP2015-45668, American Society of Mechanical Engineers (2015).
18. Gilman, T., Weitze, B., Rudolph, J., Willuweit, A., and Kalnins, A., "Using Nonlinear Kinematic Hardening Material Models for Elastic-Plastic Ratcheting Analysis," *ASME 2015 Pressure Vessels and Piping Conference* (pp. V01AT01A046-V01AT01A046), Paper no. PVP2015-45674, American Society of Mechanical Engineers (2015).
19. Hojo, K., and Kawabata, S., "Low Cycle Fatigue Evaluation Using Cyclic Loading Test Data," *ASME 2015 Pressure Vessels and Piping Conference* (pp. V01AT01A045-V01AT01A045), Paper no. PVP2015-45326, American Society of Mechanical Engineers (2015).
20. Gilman, T. D., Alleshwaram, A., and Satyan-Sharma, T., "Industry's First NRC Approved Appendix L Flaw Tolerance Evaluation to Manage Fatigue in a Surge Line," *ASME 2015 Pressure Vessels and Piping Conference* (pp. V01AT01A033-V01AT01A033), Paper no. PVP2015-45194, American Society of Mechanical Engineers (2015).
21. Rudolph, J., Kalnins, A., Götz, A., and Hilpert, R., "Local Ratcheting by Elastic-Plastic FEA — Criteria and Code Based Approaches," *Proceedings of the ASME Pressure Vessels and Piping Conference*, Paper No. PVP2011-57229 (2011).
22. Nimrouzi, H., Goldak, J. A., and Yetisir, M., "A Methodology for Optimizing Startup-Shutdown Transients for Pressure Vessel Integrity," *ASME 2015 Pressure Vessels and Piping Conference* (pp. V01AT01A049-V01AT01A049), Paper No. PVP2015-45975, American Society of Mechanical Engineers (2015).
23. J. L.Chaboche, "Time-independent constitutive theories for cyclic plasticity.", *International Journal of Plasticity* 2: 149–188 (1986).
24. J. L.Chaboche, "On some modifications of kinematic hardening to improve the description of ratchetting effects.", *International Journal of Plasticity* 7: 661–678 (1991).
25. J. L.Chaboche, "A review of some plasticity and viscoplasticity constitutive theories." , *International Journal of Plasticity* 24: 1642–1693 (2008).
26. Mohanty, S., Soppet, W. K., Majumdar, S., and Natesan, K., "Effect of Pressurized Water Reactor Environment on Material Parameters of 316 Stainless Steel: A Cyclic Plasticity Based Evolutionary Material Modeling Approach," *ASME 2015 Pressure Vessels and Piping Conference* (pp. V01AT01A039-V01AT01A039), Paper no.PVP2015-45701, American Society of Mechanical Engineers (2015).
27. Mohanty, S., Soppet, W. K., Majumdar, S., and Natesan, K., "Chaboche-Based Cyclic Material Hardening Models for 316 SS–316 SS Weld under In-air and Pressurized Water Reactor Water Conditions," *Nuclear Engineering and Design*, 305: 524-530 (2016).

28. Mohanty, S., Soppet, W., Majumdar, S., and Natesan, K., "Tensile and Fatigue Testing and Material Hardening Model Development for 508 LAS Base Metal and 316 SS Similar Metal Weld under In-air and PWR Primary Loop Water Conditions," Argonne National Laboratory, Report No. ANL/LWRS-15/02 (<http://www.osti.gov/scitech/biblio/1224989>) (2015).
29. Mohanty, S., Soppet, W., Majumdar, S., and Natesan, K., "Thermal-Mechanical Stress Analysis of PWR Pressure Vessel and Nozzles under Grid Load-Following Mode: Interim Report on the Effect of Cyclic Hardening Material Properties and Pre-existing Cracks on Stress Analysis Results," Argonne National Laboratory, Report No. ANL/LWRS-16/01 (<http://www.osti.gov/scitech/biblio/1249554>) (2016).
30. Mohanty, S., Soppet, W., Majumdar, S., and Natesan, K., "Thermal-Mechanical Stress Analysis of Pressurized Water Reactor Pressure Vessel with/without a Preexisting Crack under Grid Load Following Conditions", *Journal of Nuclear Engineering and Design* (Accepted for publication), (DOI: 10.1016/j.nucengdes.2016.09.020) (2016)
31. Sonsino, C. M., "Fatigue Testing under Variable Amplitude Loading," *International Journal of Fatigue*, 29(6): 1080-1089 (2007).
32. Zhang, Y. H., and Maddox, S. J., "Fatigue Testing of Full Scale Girth Welded Pipes Under Variable Amplitude Loading," *Journal of Offshore Mechanics and Arctic Engineering*, 136(2): 021401 (2014).
33. Dunne, F., and Petrinic, N., *Introduction to Computational Plasticity*, Oxford University Press on Demand (2005).
34. Belytschko, T., Liu, W. K., Moran, B., and Elkhodary, K., *Nonlinear Finite Elements for Continua and Structures*, John Wiley & Sons (2013).
35. Mohanty, S., Soppet, W. K., Majumdar, S., and Natesan, K., "In-Air and Pressurized Water Reactor Environment Fatigue Experiments of 316 Stainless Steel to Study the Effect of Environment on Cyclic Hardening," *Journal of Nuclear Materials*, 473: 290-299 (2016).

This page intentionally left blank



Nuclear Engineering Division

Argonne National Laboratory
9700 South Cass Avenue, Bldg. 208
Argonne, IL 60439

www.anl.gov

